TITANIUM DIOXIDE NANOMATERIALS AS NEGATIVE ELECTRODES FOR RECHARGEABLE LITHIUM-ION BATTERIES

Valentina Gentili

A Thesis Submitted for the Degree of PhD
at the
University of St Andrews

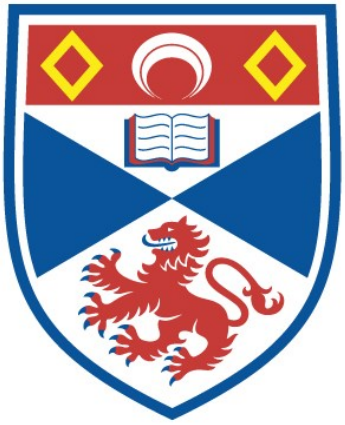

2011

Full metadata for this item is available in
St Andrews Research Repository
at:
http://research-repository.st-andrews.ac.uk/

Please use this identifier to cite or link to this item:
http://hdl.handle.net/10023/2612

This item is protected by original copyright

Titanium Dioxide Nanomaterials as Negative Electrodes for Rechargeable Lithium-Ion Batteries

Valentina Gentili

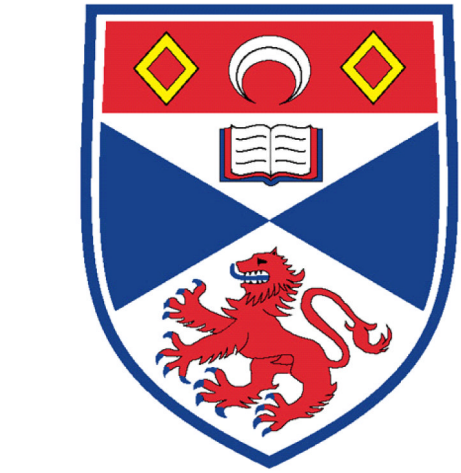

A Thesis presented for the degree of Doctor of Philosophy in the Faculty of Science of the University of St. Andrews

April 2011

Declaration

I, Valentina Gentili, hereby certify that this thesis, which is approximately 33500 words in length, has been written by me, that it is the record of work carried out by me and that it has not been submitted in any previous application for a higher degree.

I was admitted as a research student in August 2007 and as a candidate for the degree of Doctor of Philosophy in September 2008; the higher study for which this is a record was carried out in the University of St Andrews between 2007 and 2011.

Date Signature of candidate

Certification

I hereby certify that the candidate has fulfilled the conditions of the Resolution and Regulations appropriate for the degree of Doctor of Philosophy in the University of St Andrews and that the candidate is qualified to submit this thesis in application for that degree.

Date Signature of supervisor

Library declaration

In submitting this thesis to the University of St Andrews we understand that we are giving permission for it to be made available for use in accordance with the regulations of the University Library for the time being in force, subject to any copyright vested in the work not being affected thereby. We also understand that the title and the abstract will be published, and that a copy of the work may be made and supplied to any bona fide library or research worker, that my thesis will be electronically accessible for personal or research use unless exempt by award of an embargo as requested below, and that the library has the right to migrate my thesis into new electronic forms as required to ensure continued access to the thesis. We have obtained any third-party copyright permissions that may be required in order to allow such access and migration, or have requested the appropriate embargo below.

The following is an agreed request by candidate and supervisor regarding the electronic publication of this thesis:

Embargo on both all of printed copy and electronic copy for the same fixed period of 3 years on the following ground:

publication would preclude future publication.

Date Signature of candidate

Signature of supervisor

Acknowledgements

Firstly, I would like to thank Professor Peter G. Bruce for giving me the opportunity to join his research group and for his excellent guidance throughout the entirety of this PhD project.

I would particularly like to express my appreciation to Dr Yuri Andreev, Dr A. Robert Armstrong and Dr Allan Paterson and to Dr Sergio Brutti for all the helpful discussions and suggestions along the way, and for answering all my questions. Thanks are also due to Dr Laurence Hardwick for his help with the Raman microscopy and Dr Hervé Ménard from the Sasol St Andrews Laboratory for his help with the photoelectron spectroscopy. I would also like to thank all the other members of the Bruce group, both past and present, who I encountered during my studies.

I would also like to acknowledge the technical staff at the University of St Andrews, in particular Mrs S. Williamson for all her help with the analytical measurements and Mr R. Blackley for the electron microscopy.

Finally, I would like express my gratitude to my parents, my sister Sara and my fiancé Alistair for all their love, support and understanding which sustained me during my PhD.

Thanks must go to EPSRC for funding this project.

Abstract

Titanium dioxide, TiO_2, materials have received much attention in recent years due to their potential use as intercalation negative electrodes for rechargeable lithium-ion batteries. The aim of this doctoral work was to synthesise and characterise new titanium dioxide nanomaterials and to investigate their electrochemical behaviour.

Three morphologies of TiO_2(B) phase: micro-sized (bulk), nanowires and nanotubes, were synthesised. All three exhibit properties which make them excellent hosts for lithium intercalation. The nanotubes show the best capability of accommodating lithium in the structure, being able to host over one molar equivalent of lithium at low current rates (5 mA g^{-1}). The lithium insertion mechanism in the TiO_2(B) was studied using powder neutron diffraction. In addition, the nature of the irreversible capacity of the nanotubes was studied and ways of reducing it proposed.

Nanotubes of another titanium dioxide polymorph, anatase, were synthesised and characterised. Their electrochemical performance was compared with that of commercially available counterparts with different morphologies and particle sizes. The interrelation between particle size/morphology and electrochemical properties has been established. The insertion of lithium which leads to phase variations was studied using *in situ* Raman microscopy and neutron powder diffraction.

It has been demonstrated that doping of the TiO_2(B) nanotubes with vanadium improves their electronic conductivity which is essential for practical applications. Remarkably good electrochemical performance is exhibited by the 6 % V-doped TiO_2(B) nanotubes.

Index

page number

Chapter 1. Introduction

Chapter 2. Characterisation Techniques

Chapter 3. Synthesis and Characterisation of TiO_2(B) materials

Chapter 4. Electrochemical performance of TiO_2(B) materials

Chapter 7 Electrochemical performance of TiO_2 Anatase materials

Chapter 8. Vanadium doped TiO_2(B) nanotubes

Chapter 9. Summary and conclusions

Chapter 1

Introduction

1.1 Introduction

Over the last two decades, lithium ion (Li-ion) batteries have developed into the technology of choice for powering portable electronic devices such as laptops, mobile phones, handheld mp3 and gaming devices. This market is increasing rapidly due to insatiable worldwide demand for such products. However, intensive research is now being carried out on new generation of rechargeable lithium-ion batteries to meet the needs of new and even more challenging markets such as storing energy from renewable sources (wind, solar and wave power) or powering a new generation of electric or hybrid electric vehicles[1]. For applications in the renewable energy field, a step-change in energy density (energy stored per unit volume) is required along with much greater cycle life (more cycles) and larger calendar life than batteries for consumer electronics. The mass commercialisation of hybrid or electric vehicles requires batteries with much higher specific energy (energy per unit mass), energy density along with higher safety standards and lower costs.

1.2 Energy Storage

Currently, the energy economy is threatened due to our continued reliance on fossil fuels, which are in ever-increasing demand and are non-renewable. Indeed, this dependence on fossil fuels has led to a dramatic rise in CO_2 emissions over the last two hundred years (since the beginning of the industrial revolution), with possible effects including global temperature increases and overall changes in climate. There is a significant urgency for renewable energy sources which utilise clean energies. The aforementioned CO_2 issue and concomitant air pollution found in large urban areas could be resolved by replacing traditional internal combustion engines (ICEs) with either hybrid electric vehicles (HEVs), plug-in electric vehicles (PHEVs) or zero emission electric vehicles (EVs), all of which have much lower emissions than the current ICEs. Consequently, worldwide efforts to increase the use of renewable energy sources are now being made. The most heavily researched technologies are those utilising wind, wave and solar power thus producing renewable energy plants (REPs). Due to the intermittence of these energy sources, high efficiency energy storage systems are required. In fact, electrochemical systems, for example batteries, super-capacitors and fuel cells are currently being used to fulfil this important role. These systems are required to operate efficiently in storing and delivering energy from stand-alone power plants. In addition they must provide power quality and load levelling of the electrical grid in integrated systems, and also be cost effective.

As mentioned previously, the interest in rechargeable Li-ion batteries has intensified in the last twenty years as power sources for portable electronic devices. However, in the near future they will power the vehicles mentioned above and will play a major

part in the storage and delivery of electricity from both non-renewable and renewable sources.

1.3 Rechargeable lithium-ion battery

The first reversible cell was developed by Exxon in the 1970s and consisted of a metallic lithium anode, an intercalation cathode (TiS_2) and a non-aqueous solution of lithium ions as an electrolyte[2]. Lithium metal was attractive as an anodic material due to its low atomic mass (6.94 g mol^{-1}) and therefore high energy density; however, several safety issues were associated with its use in batteries. The concerns included the possibility of explosion due to dendrite growth. Due to these issues, alternative negative electrodes have been intensively studied and lithium was eventually replaced.

The first commercial lithium-ion battery was introduced by Sony in 1990 and has not changed significantly since then. In the Li-ion cell, the metallic lithium anode is replaced with a second lithium insertion compound, thus the cell consists of two lithium insertion compounds, constituting both the cathode and the anode. They are intercalation electrodes: an anode, generally of graphite or carbon based materials, and a cathode typically one of the three electro-active oxide materials, lithium cobalt oxide ($LiCoO_2$), lithium nickel oxide ($LiNiO_2$) or manganese oxide ($LiMn_2O_4$). A schematic representation of a rechargeable lithium-ion battery is shown in figure 1.1.

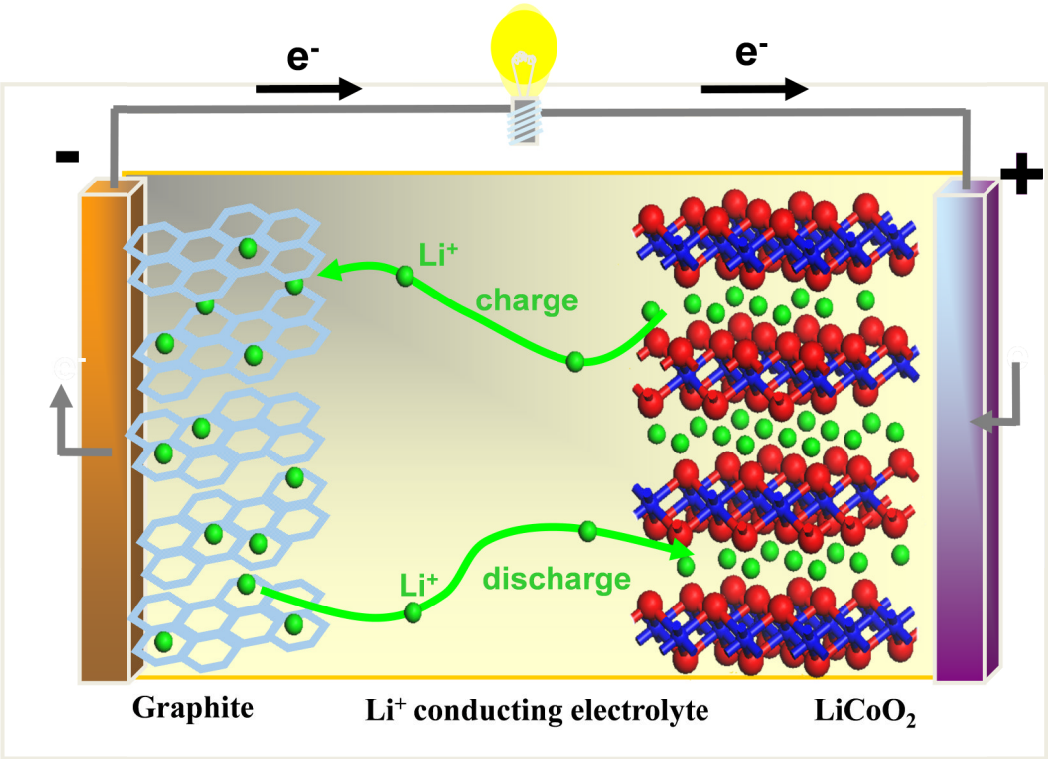

Figure 1.1 Schematic representation of a rechargeable lithium-ion battery.

During the charging phase, lithium ions are removed from the host electrode material and flow through the electrolyte and are inserted into the carbon layers of graphite. During discharge the reverse process occurs and due to charge equivalence the corresponding number of electrons travels through the external circuit. The lithium-ion battery was also known as a "rocking-chair" because of the forward and backward motion of the lithium ions which leads to major advantages in terms of energy storage.

The introduction of the lithium-ion battery, as a power source for portable electronic devices, led to the phasing out of both the nickel-cadmium (Ni/Cd) and nickel metal hydride (Ni/MH) batteries. The lithium-ion batteries have a high discharge potential (about 3.6 V), which is three times the potential of a Ni/Cd battery; they also have high specific energy (ca. 120-150 Wh kg^{-1}), more than double the value for a Ni/Cd

(50 Wh kg^{-1}) and Ni/MH (60-70 Wh kg^{-1}) battery. Moreover, they possess a long cycle life, (over 1000 charge/ discharge cycles) and do not display the memory effect (loss of maximum capacity due to being repeatedly recharged from only a partial discharge), which is a major issue for the Ni/Cd batteries.

As previously mentioned, until recently, lithium-ion batteries have been optimised for use in portable electronic applications. Lately, however, research efforts have been focussing on emerging high power applications such as electric vehicles and battery electrical energy storage systems.

1.3.1 Electrolytes for lithium-ion batteries

An electrolyte is both an ionic conductor and an electronic insulator. In Li-ion batteries the electrolyte is generally a liquid or a gel which consists of a lithium salt dissolved in a non-aqueous solvent. The ideal electrolyte must fulfil a number of requirements to be suitable for application in lithium-ion batteries[4, 5].

- High dielectric constant (ε), in other words to be able to dissolve salts to a sufficient concentration.
- High ionic conductivity (> 1 mS cm^{-1}), in order to minimise the internal resistance of the cell.
- Low viscosity (η) to ease the ionic transport.
- Wide electrochemical stability window (from 0 to 5 V *vs* Li^+/Li^0).
- Good thermal (up to 90 °C) and chemical stability.
- Compatibility with the other cell components.
- Low cost, low toxicity and low flammability.

Liquid electrolytes

Liquid organic electrolytes consist of a lithium salt dissolved in pure or a mixture of organic solvents. The lithium salts most commonly used for lithium-ion batteries are $LiPF_6$, $LiClO_4$, $LiBF_4$, $LiCF_3SO_3$ and $LiN(SO_2CF_3)$. The organic solvents employed to dissolve these salts must possess a high working voltage and a broad electrochemical stability window. In this regard, linear carbonates are the solvents of choice for lithium-ion batteries because of their superior cycling behaviour.

During lithium insertion in the graphitic negative electrodes (anodes) at low voltage, the organic solvents decompose at the anodes forming a passivating film also known as the solid electrolyte interphase layer (SEI)[6, 7]. This passivating film prevents the bulk from further corrosion, but it also leads to a non-uniform plating of lithium, which could potentially result in total cell failure caused by dendritic short circuiting, as well as serious safety problems due to local overheating.

Propylene carbonate (PC) is one of the most popular solvents employed in lithium-ion battery technology, not only because of its ability to dissolve lithium salts, thus providing high conducting electrolytes also at low temperatures, but also electrolytes containing PC as a unique solvent are stable against oxidation up to voltages of ~5 V[8]. However, when pure PC based electrolytes are used, the co-intercalation of solvated lithium occurs at the negative electrode, leading to exfoliation of the graphite, and therefore destruction of the anode[9-16]. Therefore it is necessary to blend PC with other solvents. Ethylene carbonate (EC) is reduced quicker than PC, rapidly forming a stable SEI, which prevents any further solvent co-intercalation at the anode. However, EC is a solid at room temperature, therefore it also needs to be used in blends with lower boiling point solvents such as dimethyl carbonate (DMC) and

diethyl carbonate (DEC). In figure 1.2 some examples of molecular structures of the most common solvents used in lithium-ion batteries are displayed.

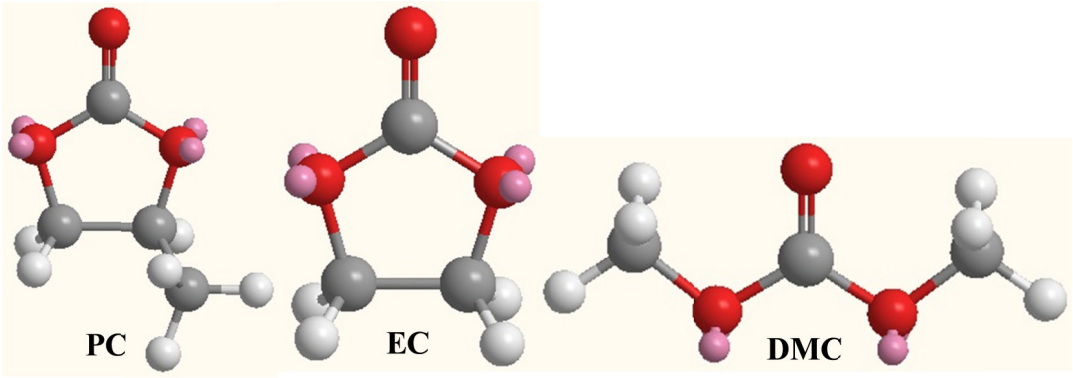

Figure 1.2 Molecular structures of some of the most popular solvents employed in lithium-ion batteries. Carbon atoms are shown in grey, oxygen in red, hydrogen in white and the oxygen lone pairs are shown in pink.

Polymer Electrolytes

In lithium polymer batteries the electrolyte consists of a lithium ion conducting polymeric matrix. The polymer electrolytes have several advantages over the traditional liquid electrolytes: firstly, since there is no liquid in the cell, they are more stable, leakage free and therefore safer; there is no need of any further separator; and finally the polymer separator is solid but flexible, keeping the design and the assembly of the battery simple, providing a technological advantage.

Poly(ethylene oxide) -$(CH_2CH_2O)_n$- (PEO) has been the most intensively studied host polar matrix for polymer electrolytes[17]. As with all polyethers, it contains co-ordinating groups along the polymer chain and can dissolve a wide variety of salts. The presence of polar groups in the PEO chain enables the dissolution of the salt and the formation of stable salt-polymer complexes, with conductivities up to 10^{-4} S cm^{-1} above the melting point of 65 °C[18].

Ionic electrolytes

Ionic liquids have recently emerged as a new class of solvents. These solvents are generally fluid at room temperature or below 100 °C and consist entirely of ionic species. They show excellent solvating properties, thus high ionic conductivity; and both high thermal and electrochemical stability (high oxidising potential). These characteristics make ionic liquids suitable for application in lithium-ion batteries. Ionic liquids have several advantages over conventional liquid electrolytes such as: a reduced or non-existent flammability; little measurable vapour pressure. Hence they emit no volatile organic compounds (VOCs) and therefore they are also environmentally friendly[19]. However, the high viscosity of this class of solvents limits high-rate cycling. The ionic liquid salt 1-Ethyl-3-methylimidazolium bis(trifluoromethylsulfonyl)imide (EMI-FSI) when used with a lithium salt, such as LiTFSI, is one of the most promising candidates in this class of solvents for application in lithium-ion batteries[20].

1.3.2 Positive electrodes

In a lithium-ion battery the materials employed for the cathode (positive electrode) are generally intercalation materials. Intercalation is the mechanism whereby a guest atom is reversibly inserted into a solid host, without causing major disruption to the host material. In the specific lithium-ion case, such a system allows the reversible reaction of removal, during oxidation (charge), and uptake, during reduction (discharge), of the lithium ions. In conventional commercial cells the cathode is initially in the discharged state with the lithium ions intercalated in the structure.

The ideal cathode material must satisfy a number of requirements[21]:

- It should be able to accommodate as much lithium as possible per formula unit and at the same time have low molecular weight.
- It has to be able to tolerate high rates of lithium insertion and removal with minimal strain being caused to the structure.
- It must have a low Fermi level in order to ensure a high cell voltage.
- It must have an operating voltage within the electrolyte electrochemical stability window and which remains constant during charge and discharge cycling.
- It should be non-toxic and environmentally benign.
- Finally it should be low cost.

Layered materials

Lithium cobalt oxide ($LiCoO_2$) is the most widely used cathode in commercial cells [4,22,23,24]. The typical cell voltage (average discharge voltage) is 3.7 V and it shows long cycle life and very high energy density. The crystal structure, shown in figure 1.3, consists of layers of CoO_6 octahedra and lithium ions which are hosted in-between the metal oxide layers.

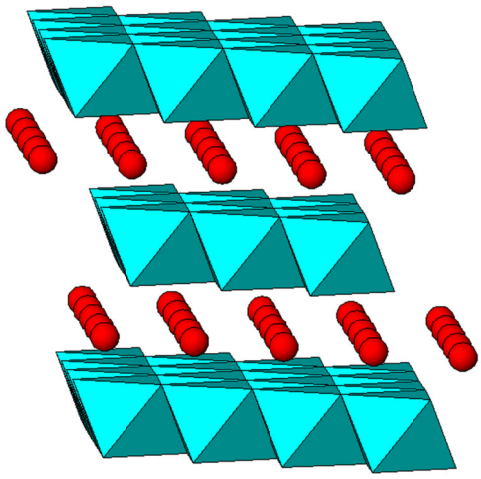

Figure 1.3 The diagrammatic structure of $LiCoO_2$, showing the octahedra CO_6 (cyan) and Li (red) .

On charging, the cobalt is oxidised from 3^+ to 4^+, giving a theoretical specific capacity of 274 mAh g^{-1}. However, only half of the lithium in the structure can be reversibly removed and re-inserted, resulting in an effective energy storage capacity of ~130 mAh g^{-1}. Moreover, the use of cobalt is associated with environmental and toxic hazards. However, there are other layered compounds which are less toxic than $LiCoO_2$ that have the potential to be used as cathodes in lithium-ion batteries. The first example is lithium nickel oxide ($LiNiO_2$), which is isostructural with $LiCoO_2$. Lithium nickel based cells provide up to 30 % higher energy density (the amount of energy stored per unit of volume) than ones based on cobalt, although the cell voltage is slightly lower, 3.6 V, and it has a specific capacity of ~140 mAh g^{-1}.[4, 23] One of the major drawbacks for application of this material, especially in high power devices, is that it also has the highest exothermic reaction of any material considered, which could give rise to cooling issues. Moreover, it is extremely difficult to synthesise these structures without some level of disorder being present.

Another class of materials receiving a great amount of attention are the lithium nickel cobalt manganese oxides $Li(NiCoMn)O_2$, such as $Li(Ni_{1/3}Co_{1/3}Mn_{1/3})O_2$. The combination of these three elements provides improved safety at lower cost and enhanced performance in terms of capacity. [25, 26]

Spinels

Another potential cathode material is the lithium manganese spinel ($LiMn_2O_4$), reported in figure 1.4. It provides a higher cell voltage compared with the cobalt based cells, in the range of 3.8-4 V and a charge storage capacity of 148 mAh g^{-1}. However the energy density of the manganese spinel is 20 % less than $LiCoO_2$. This material also shows other advantages over $LiCoO_2$ including the fact that it is highly abundant and therefore more cost effective, and it is less toxic. The chemistry of this system is more stable and therefore safer[4, 23]; however, its main disadvantage is that the manganese is gradually dissolved in the solvents over time, which therefore degrades the electrode. Despite this the manganese spinel is now starting to be commercialised (Nissan Leaf).

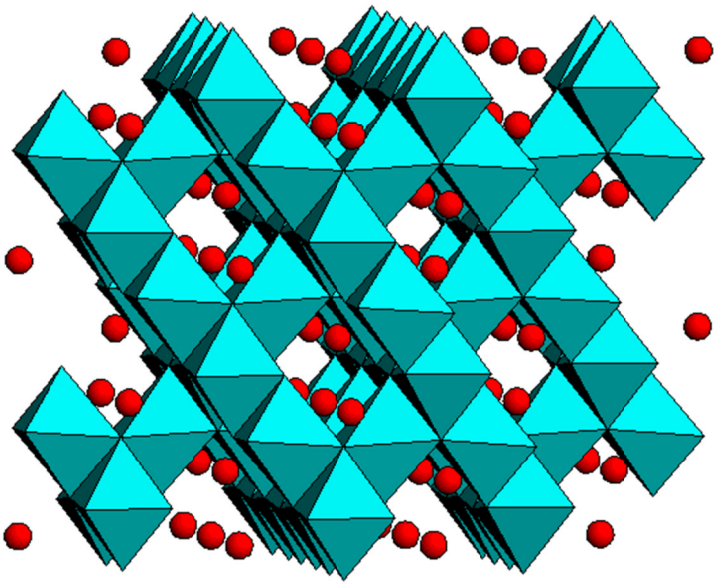

Figure 1.4 A diagrammatic structure of the $LiMn_2O_4$ spinel, showing the thedrahedral lithium (red) and the manganese oxide octahedra (cyan).

The Ni-doped spinel oxide, $LiNi_{0.5}Mn_{1.5}O_4$[27], is considered one of the most promising and attractive materials for the next generation of lithium-ion batteries because of its good cycling performance and relatively high capacity, with one dominant plateau at around 4.7 V, the highest amongst all other layered cathode materials. $LiNi_{0.5}Mn_{1.5}O_4$ is fundamentally different from pure spinels as all redox activity takes place on Ni (Ni^{2+}/Ni^{4+}) and the Mn is kept in 4^+ states. The theoretical capacity of this material is 147 mAh g^{-1}, when all the lithium ions are extracted from the material. However the Ni-doped spinel oxide has a few flaws: firstly the redox couple Ni^{2+}/Ni^{4+} is close to the potential of decomposition of the conventional lithium battery electrolyte solution (1.0 M $LiPF_6$ in EC/DMC 1:1); and secondly, it is difficult to synthesise a pure $LiNi_{0.5}Mn_{1.5}O_4$ material due to the formation of a

second $Li_xNi_{1-x}O$ phase. The formation of this second phase impairs the electrochemical performance of the $LiNi_{0.5}Mn_{1.5}O_4$ spinel. Coatings have been successfully tested to reduce the first drawback (electrolyte decomposition).

Olivines

Other potential candidates to replace the cobalt oxides are the transition metal phosphates, which have the olivine structure. The olivine structure is formed with corner sharing FeO_6 octahedra and PO_4^{3-} tetrahedral anions, with lithium occupying the octahedral holes. The structure of $LiFePO_4$ is shown in figure 1.5.

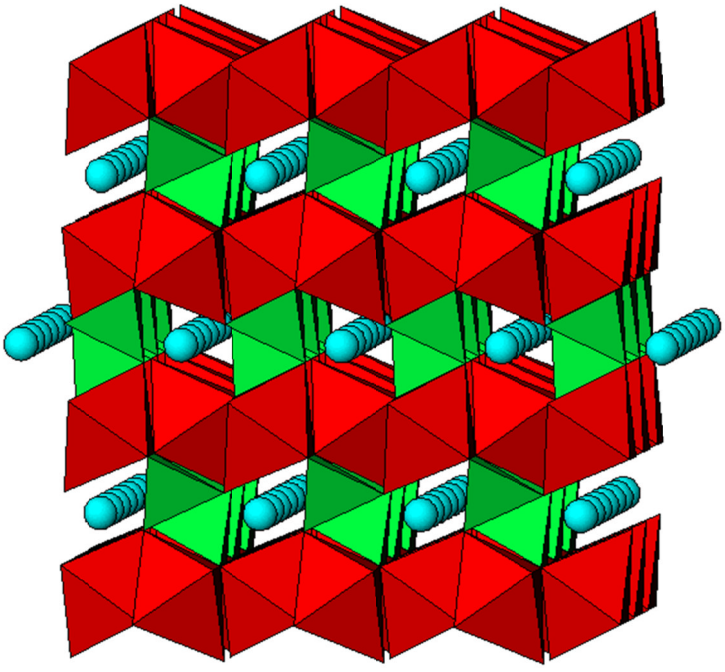

Figure 1.5 A diagrammatic representation of the Olivine $LiFePO_4$, showing the FeO_6 octahedra (red), the PO_4^{3+} tetrahedral anions (green) and lithium (cyan).

These materials offer better safety characteristics compared with the current cobalt based cathodes. In fact they also possess superior thermal and chemical stability.

The most promising of this class of olivines is the lithium iron phosphate ($LiFePO_4$) [28]. It has a cell voltage of 3.4 V and the energy storage capacity of 165 mAh g^{-1} (over 90 % of the theoretical charge capacity 175 mAh g^{-1}). Phosphates significantly reduce the drawbacks of cobalt technology, particularly in terms of cost, safety and environmental compatibility. One slight disadvantage of this material is a 14 % reduction in the energy density; however, higher energy variants are being explored.

In $LiFePO_4$ the redox energies of the Fe^{3+}/Fe^{2+} is increased due to an inductive effect from $(PO_4)^{3-}$ ions. In fact, the strong polarisation of oxygen ions into the covalent bonding within the polyanion results in the reduction of the covalent bonding to the iron ion. This reduces the Fe^{3+}/Fe^{2+} redox energy and raises the potential versus lithium for this couple. This phenomenon observed for $LiFePO_4$ has also generated some interest towards other polyanionic systems[29, 30]. For example lithium iron phosphate has recently become a highly commercialised cathode (Bosch power tools, Renault HEV, etc.)

1.3.4 Negative electrodes

We can distinguish four classes of negative electrodes for application in lithium-ion batteries: the carbonaceous materials, the lithium metal alloys, the transition-metal oxides and conversion materials. However, the most commonly used materials for negative electrodes are carbon based. In particular, graphite is the most frequently employed material in commercially available lithium-ion batteries[31].

Carbonaceous materials

Graphite and coke are the most widely used as negative electrode materials, mainly because of their non-toxicity and low cost.

Carbonaceous materials also have other advantages such as high specific capacity and having redox potentials close to 0 V; moreover they exhibit dimensional stability, since the intercalation of lithium occurs without resulting in any major structural changes.

During charging, lithium is inserted into the carbon layers and the process can be described via the following:

$$C_n + xLi^+ + xe^- \underset{\text{charge}}{\overset{\text{discharge}}{\rightleftharpoons}} Li_xC_n$$

The ability of the host material to reversibly accommodate lithium and also to what extent lithium is stored is strongly dependent on the crystallinity, the microstructure, and the micromorphology of the carbonaceous material[23].

Carbonaceous materials capable of reversible lithium intercalation can be distinguished into two classes: graphitic and non-graphitic (disordered) carbons.

Graphitic carbons are carbonaceous materials which have a layered structure with a number of structural defects. Graphite is the most well-known and has a regular layered lattice structure with perfect stacking of graphene layers[23]. At room temperature one atom lithium is inserted per six atoms of carbon, corresponding to a theoretical capacity of 372 mAh g^{-1}. However, during the first charge, an amount of charge is irreversibly consumed; this is caused by a side reaction involving the decomposition of the electrolyte, inducing (promoting) the formation of a solid

electrolyte interphase (SEI) on the electrode's surface, which, at the same time, also prevents any further electrolyte decomposition from occurring. The solvents employed strongly affect the SEI film formation. For instance, as previously mentioned in paragraph 1.3.1, propylene carbonate (PC) undergoes a reduction beginning at 0.8 V *vs* Li^+/Li^0 and at higher voltages it decomposes and starts to intercalate in the graphite layer. This then induces the exfoliation of the electrode before the SEI layer is formed; whereas the reduction of ethylene carbonate (EC) occurs rapidly and the SEI layer is formed promptly, preventing any further solvent co-intercalation and destruction of the electrode.

A class of non-graphitic or disordered carbons are the hard carbons. These materials are obtained by pyrolysis of non-expensive precursors, such as phenolic or epoxy resins, or natural carbohydrates, such as sugar, starch and cellulose. They consist of randomly stacked graphene sheets. The lithium can be inserted not only in-between the graphene layers but also in the voids and on both sides of the isolated carbon sheets, resulting in a very large storage capacity (400 and 2000 mAh g^{-1}). The hard carbons certainly have advantages over graphite electrodes in terms of cost, simplicity of processing and capacity. However, their main drawback is the high irreversibility which results in poor cycling stability[23].

Lithium metal alloys

Binary or ternary lithium metal alloys (tin, aluminium, antimony, silicon and copper-tin) are considered as very appealing negative electrodes to be explored in replacement for conventional graphite. In fact, these materials show very high specific capacity compared with graphite. However, they suffer from large volume

expansion and contraction during charge/discharge cycling, thus inducing mechanical disintegration which results in a very poor cycle life.

Transition metal oxides

Transition-metal oxides and sulphides, such as layered MoO_2, WO_2 and TiS_2, can easily intercalate lithium, and for this reason they have long been studied as negative electrodes for rechargeable lithium batteries. However, in these materials, the lithium insertion occurs at low redox potential (~1.5 V to ~2 V), resulting in rather low specific charges and, when combined with an oxidic positive electrode, rather low cell voltage[23]. Nevertheless, the low cell voltage is not necessary considered a drawback, as it makes these cells safer, compared with carbon electrodes based cells[23].

Amongst the transition metal oxides materials, lithium titanate spinel ($Li_4Ti_5O_{12}$) has been intensively studied for use as an anode material, providing high power thermally stable cells with improved cycle life.

The lithium titanate has a defect spinel-framework structure which is able to reversibly accommodate 3 lithium atoms per formula unit as shown by the reaction[32]:

$$Li_4Ti_5O_{12} + 3Li^+ + 3e^- \underset{\text{charge}}{\overset{\text{discharge}}{\rightleftharpoons}} Li_7Ti_5O_{12}$$

This results in a capacity of ~175 mAh g^{-1}. The reaction of insertion and extraction of lithium occurs without a noticeable change in lattice dimension and for this reason it is defined as a "zero strain" insertion material, which results in a large charge/discharge life expectancy. This property makes lithium titanate appealing as

an anode for Li-ion batteries. Moreover, the absence of restriction on ion flow in the structure makes higher charge/discharge rates possible at low temperatures. An additional advantage to those already mentioned is that the lithium insertion potential occurs at ~1.5 V, above the reduction potential of most organic electrolytes. Consequently, passivating films with high resistance formed by the reduction of the electrolyte will not grow on the surface. The development of no SEI also improves the long cycle life of the cell.

However, the use of the titanate spinel as an anode material in Li-ion rechargeable batteries is limited by its modest capacity and low energy density (25 % to 30 %).

Conversion materials

In a conversion reaction the active phase, M_xA_y is electrochemically reduced to a composite material consisting of nanometric metallic particles dispersed in an amorphous Li_nA matrix according to the reaction:

$$M_xA_y + ne^- + n\,Li^+ \underset{\text{charge}}{\overset{\text{discharge}}{\rightleftharpoons}} xM^0 + yLi_nA$$

This concept has been widely accepted as promising for a number of different materials such as oxides, nitrides, phosphides, sulfides as negative electrodes and fluorides for the positive electrodes. Moreover, depending on the oxidation state of the metal, these reactions have been reported to involve one (Cu_2O), two (MnO), three (Fe_2O_3) or four (RuO_2) electrons. As a consequence, innovative negative electrodes can be developed with outstanding capacity improvements over graphite or insertion oxides, while using low-cost and environmentally friendly elements such

as manganese and iron. The major drawback of this class of reactions is the poor kinetics and the consequential large voltage difference between the Li uptake and removal processes, leading to poor energy efficiency. The magnitude of this negative effect is apparently determined by the nature of the negative counter-ion "A" of the active species. This evidence suggests that the transport of the mobile ions is a key factor in these classes of materials[33].

1.4 Nanomaterials for lithium-ion batteries

Over the last twenty years a substantial amount of interest has been shown in the development of nanomaterials, resulting in an intensification of research in nano-science and nanotechnology. The term "nanostructured materials" refers to any material which has at least one dimension that is less than 100 nm[34]. It has been shown that both the physical and chemical properties of nanomaterials can differ significantly from those of bulk materials. This has led researchers to focus on producing materials with unusual and tailored properties. Nanomaterials can now be produced with a specific intended application whereby the crystallinity, size and morphology of the nanomaterial are controlled during synthesis. Nanomaterials have been produced in a wide range of morphologies, ranging from single particles to nanorods and even nanotubes.

The development of nanomaterial electrodes as lithium-ion storage materials could lead to significant improvements from the battery application perspective in terms of energy, power and cycle life. By designing the *active* energy storage component of the electrode in the nano-scale considerable advantages can be achieved[35].

Reducing the particle size enables electrode reactions to occur that cannot take place for bulk materials. The reduced dimensions increase the rate of lithium ($Li^+ + e^-$) insertion/removal, short diffusion distances (L) for Li^+ and e^-, therefore reducing the time (t) for Li insertion/removal ($t = L^2/2D$, where D is the diffusion coefficient). The high surface area of the electrode permits a high contact area with the electrolyte and, hence, high lithium ions flux across the interface. Moreover, for very small particles there is a modification of the chemical potential for lithium and electrons resulting in the change of chemical potential for the electrodes. Finally, the range of compositions over which solid solutions exist is often more extensive for nanoparticles (i.e. $LiFePO_4$) and the mechanical stresses accompanying the lithium insertion and removal reactions, the expansion and contraction during charge and discharge, is also believed to be substantially reduced, improving the reversibility.

However, moving to the nano-scale can also have a few disadvantages. For instance, nanomaterials can be more difficult to synthesise and therefore more expensive; also the electrode fabrication can be more complex. Furthermore, the high electrolyte/electrode contact area may significantly favour side-reactions with the electrolyte. It is also more difficult to maintain the inter-particles contact affecting the cell cycle life. The density of nanoparticles is normally lower compared with the bulk material.

General overview on nanomaterials morphologies

Nanomaterials can be produced via physical or chemical methods. Physical methods can be further sub-divided into mechanical or phase change methods. In the physical-mechanical method the nanomaterial is obtained by milling or grinding larger particles of the same composition of the final material, without any accompanying chemical change. This method is also commonly referred to as a "top-down" synthesis approach[36].

The physical-phase change methods consist of phase change processes such as direct precipitation and thermal, plasma or laser ablation processing in which the material is vaporised and subsequently condensed into solid in the nanometre scale range.

Chemical methods include processes in which nanomaterials are obtained via chemical synthesis. Examples include flame and spray pyrolysis, and wet-chemical methods such as sol-gel and solvo-thermal synthesis. The chemical and physical-phase change method are both referred to as a "bottom-up" synthesis approach of nanomaterials[36].

The different nano-morphologies of these materials can be classified according to the number of dimensions they have which are not nano-scaled. Nanoparticles are 0D; nanotubes and nanowires are examples of 1D nanomaterials; nanosheets are classified as having a 2D morphology and mesoporous nanoparticles are defined 3D nanomaterials[37].

The nanoparticles are the most common of all the nanomaterials. They exhibit a high surface area in the range of 40 -100 m^2 g^{-1}. They are applied in several fields, including gas sensors, where the large surface area provides high sensitivity for

lower detection limits, or in the medical field as biosensors or as carriers for targeted drug delivery[38].

Nanotubes are long cylinders that have a hollow cavity at their centre. They can have single or multi-layered walls (2-10 layers). Structurally nanotubes can be scrolled, "onion-like" or concentric in type[39].

The first TEM image of carbon nanotubes was reported in 1952, when research was focused on the prevention of nanotube formation in the coal and steel industry and in the coolant channels of nuclear reactors. Only in 1991 were carbon nanotubes rediscovered by Iijima[40]. Since then, these structures have received huge interest from the scientific community. This increasing interest has led to the development of many other materials having nanotubular morphologies, such as boron nitride nanotubes followed by inorganic nanotubes of MoS_2. More recently, several oxide nanotubes have been produced: vanadium, silicon, aluminium, magnesium, titanium and tungsten oxides were obtained by templates, sol-gel and hydrothermal methods.

Nanowires or nanorods are long, solid cylinders with a circular base, with nanowires usually being much longer than nanorods. Nanowires are similar in size to nanotubes; however, their surface area is much more modest. Usually they do not exhibit internal layered structures[39]. Nanowires can be obtained by both the physical and chemical methods, as mentioned previously, in particular, a great number of metal oxide nanowires have been produced via hydrothermal methods, such as vanadium, manganese, titanium oxides and zinc oxide.

Nanosheets are classified as 2D nanomaterials. They possess large surface areas given by their paper-like morphology. Nanosheets are usually obtained by exfoliation of layered materials or by decomposition reactions; however, often nanosheets are

found as an intermediate stage during the formation of nanotubes and nanowires[39]. Examples of materials exhibiting this particular morphology are titanium, zinc, aluminium, nickel and manganese oxides.

Porous materials can be classified into several categories according to the pore diameter. Microporous materials have diameters that are less than 2 nm, mesoporous materials have diameters between 2-50 nm and macroporous materials have diameters greater than 50 nm. Commercially, these materials have a large number of uses, including catalysis and drug delivery applications[41]. However, porous materials are becoming more attractive as electrode materials for lithium-ion batteries, due to their very high surface area which can be attributed to the internal network of pores[42].

1.5 Titanium dioxide as anode for lithium-ion batteries

Titanium dioxide, TiO_2, is the most commonly found titanium compound and it is widely employed in many applications including paints; anti-corrosion; self-cleaning coatings; solar cells and photocatalysts[39]. However, in recent years there has been much interest in using titanium dioxide materials as an anode in rechargeable lithium-ion batteries[43-48].

Titanium dioxide is very similar to lithium titanate, $Li_4Ti_5O_{12}$, in many respects. Both have a higher working potential (1.5 V *vs* lithium) than graphite, which results in a lower overall cell voltage[46]. However, the higher working potential is above the reduction potential of the electrolytes and thus improves the safety characteristics of these anode materials compared with graphite. Moreover, the low cost, low toxicity

and good cycle life of both these materials give them more advantages and therefore make them more appealing than conventional anodes.

Titanium dioxide, however, has one great advantage over lithium titanate in that it can intercalate almost twice the amount of lithium in its structure compared with lithium titanate[43,44]. This is only true for certain polymorphs of TiO_2 as it can adopt several structures: such as Anatase, Brookite, Rutile and TiO_2(B).

The only polymorphs that can intercalate Li in the bulk material are TiO_2(B) (335 mAh g^{-1})[49] and anatase (168 mAh g^{-1})[50], although it has been proven that all the polymorphs can intercalate lithium in nanostructured form, including brookite and rutile[51-57].

It is for this reason that both the TiO_2(B) and Anatase polymorphs have received such interest for electrochemical applications[43-48].

This thesis has focused on the synthesis, characterisation and the improvement in the electrochemical properties of nano-sized TiO_2(B) and Anatase structures for their future application as anodes in rechargeable lithium-ion batteries.

References

1. Scrosati, B. and Garche, J. *J. Power Sources* (2010) **195** 2419.
2. Whittingham, M.S. *Science* (1976) **192** 1126.
3. Nagaura, T. *International Battery Seminar (3)* Deerfieeld 1990).
4. Linden, D.; Reddy, T.B. *Handbook of Batteries*. Third Edition, McGraw-Hill, NewYork, 2002.
5. Xu, K. *Chemical Reviews* (2004) **104** 4303.
6. Peled, E. *J. Electrochem. Soc.* (1979) **126** 2047.
7. Balbuena, P.B.; Wang, Y.X. eds. *Lithium Ion Batteries: Solid Electrolyte Interphase* Imperial College Press, London, 2004.
8. Arakawa, M.; Yamaki, J.-I. *J. Power Sources* (1995) **54** 250.
9. Shu, Z.X.; McMillan, R.S.; Murray, J.J. *J. Electrochem. Soc.* (1995) **140** 2873.
10. Dey, A.N.; Sullivan, B.P. *J. Electrochem. Soc.* (1970) **117** 222.
11. Fong, R.; Van Sacken, U.; Dahn, J.R. *J. Electrochem. Soc.* 1990 **137** 2009.
12. Aurbach, D.; Ein-Eli, Y.; Chusid, O. Y.; Carmeli, Y.; Babai, M.; Yamin, H. *J. Electrochem. Soc.* (1994) **141** 603.
13. Aurbach, D.; Chusid, O. Y.; Carmeli, Y.; Babai, M.; Ein-Eli, Y. *J.Power Sources* (1993) **43** 47.
14. Aurbach, D.; Ein-Eli, Y.; Markovsky, B.; Carmeli, Y.; Yamin, H.; Luski, S. *Electrochim. Acta* (1994) **39** 2559.
15. Dahn, J.R.; Fong, R.; Spoon, M. *J. Phy. Rev. B* (1990) **42** 6424.
16. Abe, T.; Kawabata, N.; Mizutani, Y.; Inaba, M.; Ogumi, Z. *J. Electrochem. Soc.* (2003) **150** A257.
17. F. Gray & M. Armand in *Energy Storage Systems*.Chap 10 p. 351-406.Ed. T. Osaka & M. Dalta. Gordon and Breach Science Publishers (2000).
18. Owen, J.R. *Chemical Society Reviews* (1997) **26** 259.

19. Paranham, E.R. and Morris, R.E. *Acc. Chem Res.* (2007) **40** 1005-1013.

20. Holzapfel, M.; Jost, C.; Novak, P. *Chem. Comm.* (2004) **18** 2098.

21. Bruce, P.G. *Chem. Comm.*(1997) 1817.

22. Tarascon, J.M.; Armand, M. *Nature* (2001) **414** 359.

23. Winter, M.; Besenhard, J.O.; Spahr, M.; E. Novak, P. *Adv. Mat.* (1998) **10** 725.

24. Whittingham, M.S. *Chemical Reviews* (2004) 104 4271.

25. MacNeil, D.; Lu, D.Z. and Dahn, J.R. *J. Electrochem. Soc.* (2002)**149 (**10) A1332-A1336.

26. Shaju, K.M. and Bruce, P.G. *Adv. Mater.* (2006**) 18** 2330–2334.

27. Santhanam, R. and Rambabu, B. *J. Power Sources* (2010) **195** 5442-5451.

28. Padhi, A.K.; Nanjundaswamy, K.S.; Masquelier, C.; Osaka, S.; Goodenough, J.B. *J.Electrochem. Soc.* (1997) **144** 1609.

29. Padhi, A.K.; Nanjundaswamy, K. and Goodenough, J.B. *J. Electrochem. Soc.* (1997) **144** 1188-1194.

30. Ellis, B.L.; Lee, K.T. and Nazar, L.F. *Chem. Mater.* (2010) **22** 691–714.

31. Shukla, A.K.; Prem Kumar, T. *Curr. Sci* (2008) **94** 314.

32. Ohzuku, T.; Ueda, A. and Yamamoto, N. *J. Electrochem. Soc.* (1995) **142** 1431-1435.

33. Cabana, J; Monconduit, L.; Larcher, D. and Palacin, M.R. *Adv. Mat*. (2010) **22** E170-192.

34. ASTM Standarads Document E2456 (2006).

35. Bruce, P.G.; Scrosati, B.; Tarascon, J.M. *Angew. Chem Int. Ed.* (2008) **47** 2930-2946.

36. Hunt, A.; Jiang, Y.; Zhang, Z.; Venugopal, G. Chapter 5 *Nano-Bio-Electronic, Photonic and MEMS Packaging* (Edited by Wong, C.P.; MoonK-Y.; Li, Y.) Springer 2010.

37. Pokropivny , V.V.; Skorokhod V.V *Mat. Sc. and Eng. C* (2007) **27** 990–993.

38. Franke, M.; Koplin, T. and Simon,U. *Small* (2006) **2** *36.*

39. Bavykin D.V. and Walsh F.C., *Titanate and Titania Nanotubes*, RSC Nanoscience and Nanotechnology, RSC publishing, 2010.

40. Iijima, S. *Nature* (1991) **354**.

41. Vallet-Regi, M.; Balas, F. and Arcos, D. *Angew. Chem. Int. Ed.*(2007) **46** 7548-7558.

42. Ren, Y.; Hardwick, L. and Bruce, P. *Angew. Chem. Int. Ed.* (2010) **122** 2624-2628.

43. Armstrong, A.R., Armstrong, G.; Canales, J.; Garcia, R.; Bruce, P G. *Adv. Mater.* (2005) **17** 862.

44. Armstrong, A.R., Armstrong, G.; Canales, J.; Bruce, P.G. *J. Power Sources* (2005) **146** 501.

45. Armstrong, A.R., Armstrong, G.; Canales, J.; Bruce, P.G. *Angew. Chem. Int. Ed.* (2004) **43** 2286.

46. Armstrong, G; Armstrong, A.R.; Bruce, P.G.; Reale, P.; Scrosati, B. *Adv. Mater.* (2006) **18** 2597-2600.

47. Sudant, G.; Baudrin, E.; Larcher, D.; Tarascon, J.M. *J. Mat. Chem.*(2005) 1263.

48. Huang, S.Y.; Kavan, L.; Exnar,I.; Gratzel, M. *J. Electrochem. Soc.* (1995) **142** L142.

49. Marchand, R.; Brohan, L. and Tournoux, M.; *Material Research Bulletin* (1980) 15 1129.

50. Cava, R.J.; Murphy, D.W. and Zahurak, S.; *J. Solid State Chem.* (1984) **53** 64-75.

51. Sudant, G.; Baudrin, E.; Larcher, D.; Tarascon, J.M.; *J. Mater. Chem.* (2005) **15** 1263.

52. Baudrin, E.; Cassaignon, S.; Koesch, M.; Jolivet; J.P.; Dupont L.; Tarascon, J.-M.; *Electrochem. Commun.,* (2007) **9** 337.

53. Wagemaker, M.; Borghols,W.J.H.; Mulder, F.M.; *J. Am. Chem. Soc.* (2007) **127** 4323.

54. Reddy, M.A.; Kishore, M.S.; Pralong, V.; Varadaraju, U.V.; Raveau, B. *Electrochem.Solid-State Lett.*; (2007) **10** A29.

55. Borghols, W.J.H.; Wagemaker, M.; Lafont, U.; Kelder, E.M.; Mulder, F M. *Chem. Mater.* (2008) **20** 2949.

56. Hu, Y.S.; Kienle, L.; Guo, Y.-G.; Maier, *J. Adv. Mater*. (2006) **18** 1421.

57. Dambournet, D.; Belharouak, I. and Amine, K. *Chem. Mater.* (2010) **22** 1173-1179.

Chapter 2

Characterisation Techniques

2.1 Powder X-ray Diffraction Technique

X-ray diffraction is an established technique for both qualitative and quantitative phase analysis of solids as well as for studying structure and morphology. X-ray diffraction can be performed on both single crystals and powdered materials.

The technique is based on the diffraction of X-rays by the crystal lattice planes. X-rays are scattered by the electrons of an atom. Given parallel atomic planes, the scattered intensity diffracted by each plane interferes either constructively or destructively depending on the different phase shift between the two waves, (fig.2.1)[1]. The conditions for constructive interference are described by Von Laue's law and, in a simpler way, by Bragg's law[2].

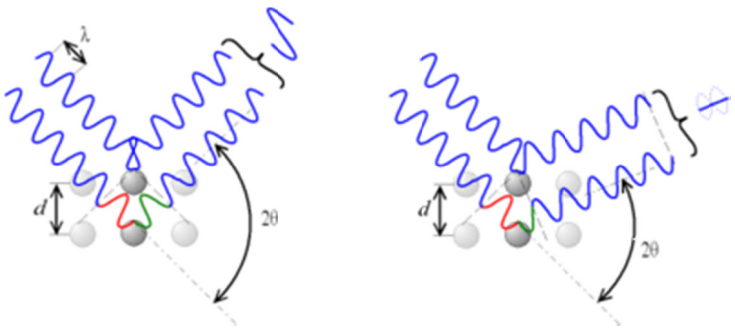

Figure 2.1 The scheme showing Bragg's law.

The condition for constructive interference, as defined by Bragg's law, is:

$$n\lambda = 2d\sin\theta \qquad (1)$$

Where n is an integer, λ is the wavelength of the radiation, d is the interplanar spacing and θ is the incident angle.

The incident electromagnetic radiation (X-rays) must possess a wavelength of the same order of magnitude as d (~ 10^{-10} m). X-rays may be generated by synchrotron radiation or by striking a metal target e.g. Cu or Fe with electrons.

A single crystal gives a diffraction pattern with discrete diffraction spots, each in a definitive direction, relative to the orientation of the crystal and the incident beam.

In the case of powder diffraction, the sample consists of a large number of small stationary single crystallites, all randomly oriented. The diffracted rays are arranged in a series of concentric cones (fig.2.2). By sampling along a longitudinal plane the intensities of the cones can be measured as a series of peaks.

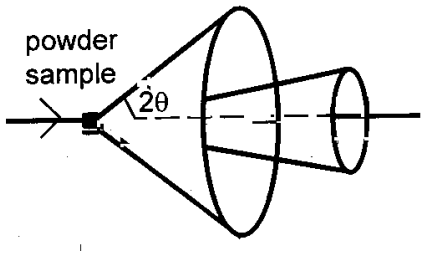

Figure 2.2 The differing orientations of crystallites in the powder around the incident beam give diffraction reflections that lie on a cone.

The most intense lines of X-ray radiation emitted from a metal anode result from 2p → 1s transitions, labelled Kα. For a Cu anode, $K\alpha_1$ has a wavelength of $\lambda = 1.5418$ Å and for Fe $K\alpha_1$ $\lambda = 1.936$ Å.

Powder X-ray diffraction has been extensively used to investigate the crystal structure throughout this work in both reflection and transmission mode.

In the case of air-sensitive materials, samples were sealed in a glovebox either between two pieces of polyethylene sheets using vacuum grease or in glass capillary tubes using non corrosive silicon rubber.

Powder X-ray diffraction was performed in reflection mode using a Philips XPERT data collector, with Cu Kα1 radiation.

2.2 Neutron Diffraction

Neutrons have a mass of 1.660437×10^{-27} kg and wavelengths of the order of atomic distances (0.5 to 3 Å, depending on the energy), therefore, they are particularly suitable for applications in structural analysis via neutron diffraction.

Neutrons are scattered from materials by interacting with the nucleus of an atom rather than the electron clouds like X-ray photons are scattered in X-ray diffraction. This allows use of neutron diffraction techniques to detect light atoms even in presence of heavy atoms with many electrons, which would be difficult using X-ray diffraction. In fact, the neutron scattering lengths of most atoms are approximately equal in magnitude.

Due to the lower intensity of the neutron beam, a larger sample size for neutron diffraction is required. However, as neutron absorption is weak, they can penetrate the sample to a great depth allowing for probing of much bulkier material.

In neutron diffraction, it is the atomic nucleus that is responsible for the scattering of the neutrons. When a wave of unit amplitude strikes a nucleus of an atom in a solid, the nucleus is not free and recoils. The resulting scattered neutron amplitude, *A*, at a given distance *R* from the nucleus is:

$$A = \frac{b}{R} \qquad (2)$$

Where *b* is scattering amplitude, which is a complex quantity with a length dimension.

Since the radius of the nucleus is around 10^5 times smaller than the incident neutron wavelength, the angular dependence of *b* is negligible compared with the similar dependence for X-rays. The nuclear dependence of scattering allows isotopes of the same element to have substantially different scattering lengths in terms of absolute value and sign for neutrons.

Neutrons can be generated by nuclear fission. The experiments reported in this work were carried out at ISIS pulsed neutron and muon source at the Rutherford Appleton Laboratory in Oxfordshire. At ISIS pulsed neutrons are generated by a nuclear proton-neutron reaction, in which a beam of protons strikes a target of heavy atomic nuclei (tungsten). This process is known as *spallation*. At the facility source, the neutron beam is pulsed, thus neutrons with different wavelengths can be discriminated against by their time of arrival, *time of flight* (TOF), at the detector. At this stage different d-spacings are measured at fixed θ, according to Bragg's law:

$$\lambda = 2d_{hkl} \sin \theta_0 \qquad (3)$$

with λ being the wavelength of the incident neutron radiation.

In order to ensure the highest count rate, several banks of detectors are placed at different scattering angles, allowing access to a large number of possible d-spacings.

The spallation process produces neutrons which have very high energy; therefore it is necessary to slow them down employing moderators before they can be used for neutron diffraction studies. Using a series of beam guides, the neutron beam is split and directed to a number of different diffractometers, at which point various experiments can then take place.

For the purpose of this work, data was collected at the ISIS facility on the high intensity, medium resolution diffractometer POLARIS and on the high intensity, medium resolution, general material diffractometer GEM.

2.2.1 Rietveld Refinement

Following successful data collection at ISIS, the neutron diffraction patterns were subjected to Rietveld data analysis in order to determine the structure of the samples of interest. The Rietveld method is an analysis procedure that overcomes the problems associated with peak overlap in a power diffraction pattern by treating each point in the pattern as an individually observed intensity[3]. Using the given instrumental parameters describing the reflection shape and width, and the sample parameters describing the various position and intensities of the reflections, a structural powder diffraction model is obtained.

This model is then refined against the collected data using least squares methods to obtain the best fit. In this work the GSAS program suite and TOPAS Academic were adopted for the Rietveld refinement process[4].

Initially, the background and the scale are refined to obtain a reasonable structural model and subsequently the peak shape and other parameters such as unit cell, x y z atomic coordinates, the site occupancies and the Debye-Waller factors are refined. The quality of the refinement is estimated from the value of the weighted residual factor R_{wp}.

$$R_{wp} = \left\{ \frac{\sum_i w_i [y_i(obs) - y_i(calc)]^2}{\sum_i w_i [y_i(obs)]^2} \right\} \qquad (4)$$

Where $y_i(obs)$ and $y_i(calc)$ are the observed and the calculated intensities respectively and w_i is a suitable weight at the ith step.

The quality of the data can be evaluated and is represented by R_{exp} (R- expected), which is defined by the equation below, where *N* is the number of profile points and *P* the refined parameters.

$$R_{\text{exp}} = \left\{ \frac{(N-P)}{\sum_{i=1}^{n} w_i y_i^{\,2}} \right\}^{\frac{1}{2}} \qquad (5)$$

Evaluation of the data should lead the value of R_{wp} to approach that of R_{exp}, and this would be observed in the goodness of fit value χ^2 which should approach 1.

$$\chi^2 = \frac{R_{wp}}{R_{exp}} \qquad (6)$$

2.3 Scanning Electron Microscopy (SEM) and Energy Dispersive Spectroscopy (EDS)

Scanning electron microscopy (SEM) is a technique which allows investigation of the morphology, texture and topography of samples of up to hundreds of nanometers or tens of nanometres using the field emission electron microscope (FESEM).

An electron beam is thermo-ionically emitted from a tungsten or lanthanum hexaboride (LaB_6) wire or a field emission gun (FE). The electron beam is then accelerated by passing across a potential difference and is focussed onto the surface of the sample. The primary beam interacts with the sample, resulting in the emission of electrons and electromagnetic radiation, which are then focused onto a detector. The emitted electrons from the sample are used to produce detailed two-dimensional images, which due to high depth of focus have a high tri-dimensional quality. The detected electromagnetic radiation (X-rays) can provide information regarding the elemental composition of the sample; this is known as energy dispersive spectroscopy (EDS).

The primary electron beam ejects electrons from the core energy levels which then allows high energy electrons to drop down to lower energy levels which emit X-ray radiation. The EDS sensor is capable of detecting and discriminating the energy of the X-ray radiation emitted. The energy of the X-ray emission is specific to the constituent elements.

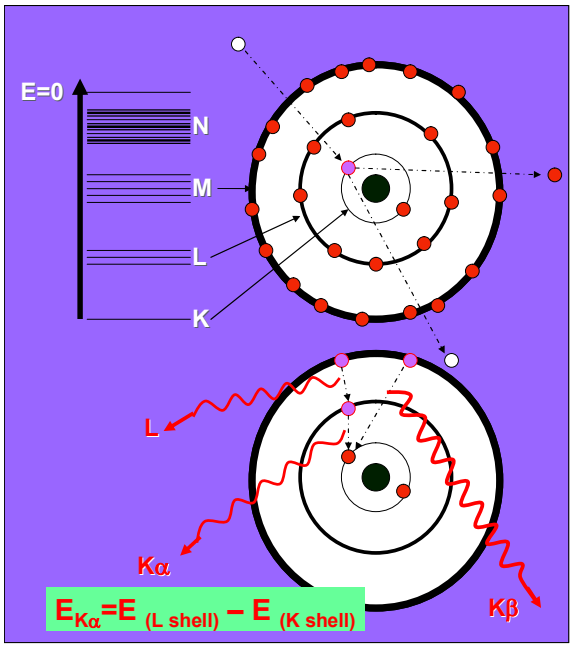

Figure 2.3 (a) Diagram of an electron knocking out an electron in the K-shell. (b) Diagram showing the upper shell electron moving in to compensate for the lower level loss and the corresponding X-ray being emitted.

Non-conductive samples require to be coated with an ultrathin layer of electrically-conducting material (usually gold or graphite) to prevent build up of charge during the scan, while no special preparation is needed for conductive samples.

For the work in this thesis, samples were examined using a JEOL JSM-5600 scanning electron microscope with a resolution of up to 3.5 nm and a field emission scanning electron microscope Hitachi Type II S-4800 with a resolution of 1 nm.

2.4 Transmission Electron Microscopy (TEM)

High resolution transmission electron microscopy is an extremely powerful characterisation technique, which allows observation of nano-scale samples to determine their morphology and it also can provide structural information down to ~0.2 nm spatial resolution. In addition electron diffraction can be performed to facilitate examination of the local crystal structure.

TEM works using a similar principle to that of SEM, whereby a beam of electrons is generated and then accelerated by passing a differential potential and focussed onto the sample.

The focussed, monochromatic electron beam interacts with and is transmitted through the sample, focussed into an image and projected onto a phosphor coated screen which emits visible light (see figure 2.4).

For the work in this thesis, samples were examined using a Jeol JEM 2011, which operates at 200 kV, with a maximum magnification of 1,500,000.

.

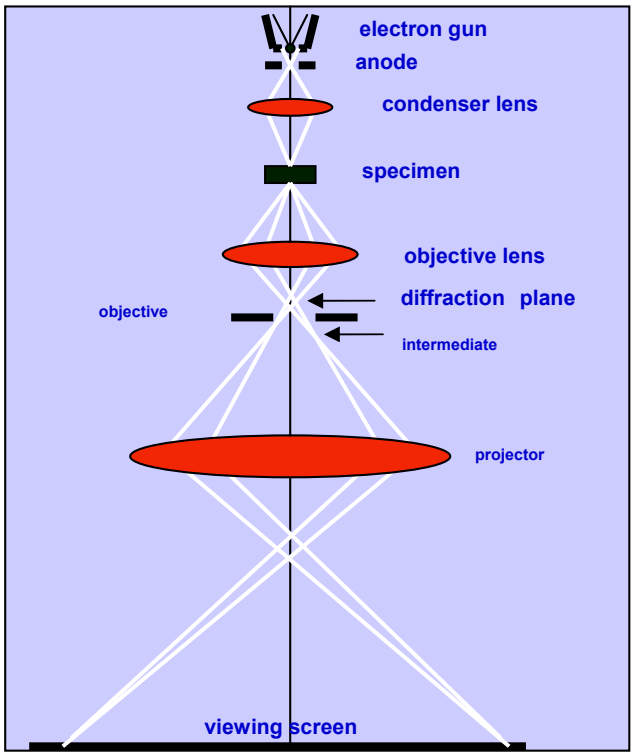

Figure 2.4 Diagram displaying the series of lenses the electron beam passes through.

2.5 BET surface area measurements

Surface area analysis using nitrogen gas is now being extensively used in order to estimate the accessible area within a solid via multilayer coverage of nitrogen atoms. Brunauer, Emmett and Teller extended the original theory from Langmuir by incorporating the concept of multi-layer absorption in a sample[5]. This theory is now known as BET theory, named after its founders. The theory is governed by the following equation:

$$\frac{1}{V[(P_0/P)-1]} = \frac{1}{V_m C} + \frac{C-1}{V_m C}\left(\frac{P}{P_0}\right) \qquad (7)$$

Where; P is the equilibrium pressure of nitrogen, P_0 is the saturation pressure of nitrogen at the adsorption temperature, V is the volume of adsorbed nitrogen on the solid, C is the BET constant and V_m is the quantity of adsorbed nitrogen via a monolayer mechanism.

In this thesis all the samples were run volumetrically using a Micromeritics ASAP 2020 surface area and porosity analyser. All experiments were carried out at 77 K using a liquid nitrogen bath. Prior to analysis, samples were degassed under vacuum and exposed to temperatures between at 200-250 °C for an extended time period.

2.6 Thermogravimetric analysis (TGA)

Thermogravimetric analysis (TGA) is a technique which allows quantification of the loss of mass in a given sample with increasing temperatures.

The sample is placed in an alumina crucible which is subsequently heated in a controlled manner under a gaseous flow (usually nitrogen). The change in mass of the specimen is recorded during the experiment and can provide information on degradation temperature, absorbed moisture content of materials as well as the level of inorganic and organic components, decomposition points and solvent residues.

Experiments were carried out using a Mettler Toledo SDTA 851^e instrument.

2.7 Raman Spectroscopy

Raman spectroscopy is used in material science to study vibrations (phonon modes) in a sample. It is often used as a fingerprint technique since vibrational information is specific to the chemical bonds in a material[6].

In a typical experiment laser light from the visible range of the spectrum interacts with molecular vibrations, phonons or other excitations in the sample, resulting in the photons of the laser being inelastically scattered, this is known as Raman scattering.

The difference in energy between the incident light and the emitted light is equal to the vibration of molecules in the sample. This energy is detected and a Raman spectrum plot of the scattered light versus the energy difference is recorded[6].

In an *ex situ* microscopy experiment a quartz capillary tube is filled with the sample under investigation (air sensitive samples are sealed in Ar atmosphere). The objective lens focuses the laser onto the sample in the capillary and the Raman spectrum of a single point is collected in a back-scattering configuration.

In situ Raman spectroscopy allows investigation of the changes in the electrode surface during potentiostatic or galvanostatic cycling to be recorded under Raman scattering conditions.

The electrode under investigation is mounted in a two electrode Raman cell (fig.2.5) specifically engineered for this type of experiment.

The two-electrode in situ Raman cell consists of a Teflon body and the cell set up consists of a working electrode (active mass < 1 mg) versus a lithium counter and reference electrode. The lithium counter/reference electrode sits on a moveable titanium current collector with adjustable height to optimise contact. The copper current collector for the working electrode possesses a hole < 1 mm diameter from

which the backside of the working electrode can be viewed and measured. Two polypropylene separators are placed between the electrodes and soaked with a few drops of a lithium-ion conducting electrolyte. Rubber seals ensure that the cell is air and moisture tight.

All the experiments were carried out in the laboratory of Prof. Duncan Graham at Strathclyde University in Glasgow. The instrument employed for the *ex situ* experiments was a Renishaw equipped with Leica optics (laser excitation wavelength 632.8 nm). The *in situ* Raman data was collected by a Renishaw InVia Raman inverted and upright microscope system (Renishaw, Wotton-under-Edge, UK), equipped with 50/0.5 long working distance objectives, combined with Solartron Modulab potentiostat. A laser excitation wavelength of 632.8 nm was used, with a filter employed to reduce the laser power to 3mW at the electrode surface. The measurement is carried out using a backscattering configuration through the glass window onto the upper electrode under investigation, which is visible through an opening in the current collector. Further details of the setup of the *in situ* Raman cell have been described previously elsewhere[7].

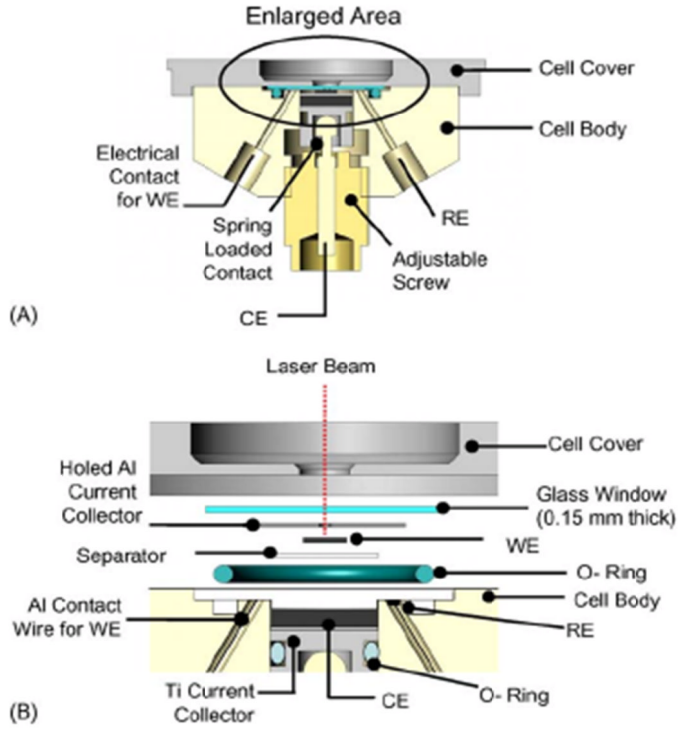

Figure 2.5 *In situ* Raman cell in (A) the fully assembled stage and in (B) an enlarged area showing the separate components (expanded, not in scale).

2.8 Fourier Transform Infrared Spectroscopy (FTIR)

Infrared spectroscopy yields similar and complementary information to Raman spectroscopy. This technique utilises the infrared region of the electromagnetic spectrum, which is characterized by having a lower frequency and a longer wavelength compared with visible light. The infrared region can be subdivided into three sections known as near , mid and far-infrared. The mid-infrared region (4000–400 cm^{-1}, 2.5–25 μm) is the most commonly studied segment as it contains

information regarding the fundamental vibration and associated vibrational structure of a specific sample.

Infrared spectroscopy relies upon the fact that materials have specific frequencies where they vibrate and these correspond to discrete energy levels. A change in permanent dipole is required for a vibrational mode in a material to be IR active.

An IR spectrum of a sample is recorded by focussing a beam of infrared light at the specimen. For the purpose of this thesis a Fourier transform infrared (FTIR) spectrophotometer was used. This method operates by having a moving mirror, which alters the distribution of the infrared light as it passes through the interferometer. The signal which is recorded represents the light output as a function of mirror position, specifically referred to the interferogram. This raw data is turned into the final spectrum (light output versus infrared wavelength or wavenumber) using a Fourier transform method. Comparison is then made with reference material.

All IR experiments reported in this thesis were carried out on a Nicolet 6700 FT-IR system, which is located in a nitrogen filled glove-box, to protect the air-sensitive samples from any moisture or air contamination.

Prior to each experiment a reference spectrum was recorded in order to correct the final spectra for background effects. Pellets were prepared by grinding a small amount of the specimen together with caesium iodide and placed in a mechanical press.

2.9 Photoelectron Spectroscopy

X-ray photoelectron spectroscopy (XPS) is a powerful technique for surface analysis. It provides both qualitative and quantitative information on the elements present on a given surface (except for H and He), by illuminating the surface under investigation with X-ray radiation and analysing the ejected electrons, as a consequence of the photoelectric effect.

The physics of this process can be effectively described by the following:

$$E_B = h\nu - E_K \quad (8)$$

where E_B is the binding energy of the electron in the atom, which depends on the type of atom and its chemical environment. The energy of the X-ray excitation source, is given by the known value hν, and E_K is the kinetic energy of the emitted electron which is measured by the spectrometer. Thus E_b is obtained from hν, known, and E_K, measured[8].

A typical XP spectrum consists of a series of discrete lines of different intensities over a background due to inelastic scattering, the intensity of which decreases with decreasing binding energy. Each of these lines is characterised by a position (eV), a full width at half maximum (FWHM) (eV) and an intensity (cps).

The peak position is related to the orbitals from which the electrons are emitted and the intensity is correlated to the amount of material present. By comparison with tabulated data it is possible to identify the element present in the spectrum and the surrounding environment.

The composition of the sample can be determined by quantitative analysis and by mathematically fitting the data. For this work CasaXPS software was used.

For the purpose of this thesis, XPS has been employed to investigate the surface composition of TiO_2 electrodes at different charges. The instrument used is a Kratos Axis Ultra high resolution XPS, equipped with monochromatic aluminum X-ray source (hν = 1486.69 eV), charge neutraliser and a hemispherical analyzer equipped with a Delay-Line detector (DLD) and multichannel plate. All the experiments reported in this thesis were performed in the Sasol laboratories in St Andrews.

2.10 Electrochemical Characterisation

2.10.1 Basic principles of Electrochemical Energy Storage and Conversion

In an electrochemical cell, the chemical energy, which is the Gibbs free energy associated with the cell reaction, is converted into electrical energy and vice versa. The energy –providing processes are the redox reactions taking place at the interface electrode with the electrolyte[9].

Faraday's law

The amount of electrical charge transferred in an electrochemical reaction: $Ox + ze^- \leftrightarrows Red$ is given by Faraday's law[10].

$$Q = zF\frac{m}{M} \quad (9)$$

Where Q is the total electric charge passed through; m is the mass of the substance undergoing the electrochemical process; M is the molar mass of the substance; F is Faraday's constant 96487 C mol^{-1} (26.8 Ah mol^{-1}) and z is the valence number, i.e.

the number of electrons transferred per mole of substance. Reorganising the equation:

$$m = \frac{Q}{F}\frac{M}{z} \quad (10)$$

From Faraday's law, the quantity of substance required to transfer a certain amount of charge during the redox reaction is proportional to the substance equivalent mass. Thus, it is desirable to choose an electrodic material with very low molar mass, *M,* and high equivalent number, *z*, in order to minimise the equivalent mass and maximise the amount of charge transferred, *Q*, per unit mass.

Cell potential

When two phases such as an electrode and an electrolyte are put in contact, an electrical double layer is formed at the interface, across which a potential difference exists. The potential difference between two electrodes immersed in the same electrolyte solution, each with its own double layer, can be obtained by the thermodynamics and kinetics of the reactions occurring at both the electrodes.

The equilibrium potential difference, ΔE, between the two electrodes is given by the following equation:

$$\Delta E = -\frac{\Delta G}{nF} \quad (11)$$

Where ΔG is variation of the Gibbs free energy for the overall cell reaction, n is the number of equivalents involved in the process and F is the Faraday's constant (96487 C mol^{-1}).

Specific capacity

The specific capacity (Q_{sp}) of the electrode is defined as the total amount of current (I) passed per unit mass (m) of electrode material during the time (t) necessary for complete discharge or charge:

$$Q_{sp} = I\frac{t}{m} \qquad (12)$$

In order to achieve improvements in current lithium-ion battery technology, electrode materials are required having high specific charge, in terms of both specific (mAh g^{-1}) and volumetric (mAh cm^{-3}) capacity, and also having high potential difference between the two electrodes, anode and cathode.

Specific Energy

The specific energy of a battery, W_e, is the amount of energy which can be stored per unit mass. The theoretical maximum specific energy W_e^{th} (Wh kg^{-1}) can be obtained from the following expression:

$$W_e^{th} = \frac{\Delta G}{\sum_i n_i M_i} \qquad (13)$$

Where n_i is the number of moles of reactant i involved in the process and M_i is the molar mass of reactant i. In practice, the specific energy associated with a battery is noticeably lower compared with its theoretical value.

For a simple two-phase redox process at constant potential, the specific energy is given by the following expression:

$$W_e = Q_{sp}\, V \qquad (14)$$

The weight of a battery is an important aspect to be considered with regard to possible applications, as it is necessary to minimise the weight of reactant for a given amount of energy stored, W_e.

Energy density

The energy density is the amount of energy stored per unit volume and is obtained from a very similar formula to expression (13), where the molar mass of reactant M_i is replaced with the molar volume of reactant V_i. For application in small devices (micro-batteries), such as implantable medical devices, it is necessary to minimise the molar volume of reactant in order to achieve high energy densities.

$$W_{dens} = W_e \rho \qquad (15)$$

Rate and Kinetics

Modern batteries require not only high energy and capacity, but they also need to provide high power working at a high discharge current regime. In other words, the electrode material needs to be able to supply charge also at high rates (> 1C, the full capacity in less than 1 h). This addresses the kinetics of the redox process at the electrodes and it is typically improved by reducing the size of the electrode active material.

The rate at which a battery can be discharged is the determining factor for its future application in different devices. It is strictly dependent on the rate of transportation of the mobile ions during the process. According to the law of electroneutrality, the rate of diffusion of the ions and charge must be equal to the rate of the electrons passing through the external circuit. It is thus the combined diffusion of Li^+ and e^-

down a concentration gradient that is important. Although in most cases of intercalation the rate limiting step is the mobility of the lithium ions.

2.10.2 Electrode fabrication and cell assembling

The electrochemical properties of the materials synthesised for this project were all thoroughly investigated for possible application in rechargeable lithium batteries.

Following successful synthesis of the materials, cells were assembled utilising the material as an electrode to allow testing using the following techniques: a.c. impedance, galvanostatic cycling and potentiodynamic cycling with galvanostatic acceleration (PCGA).

The electrodes were prepared by two different methods, either in pellet form or casting. The first method consisted of hand grinding the active material together with carbon (Super P, MMM Carbon) and binder (PVdF and HFP copolymer, Kynar). This was then pressed using a die set into a self-supporting pellet of 13 mm diameter. The second method involved the same mixture being suspended in a solvent (usually acetone or tetrahydrofuran) which is able to dissolve the binder and form homogenous slurry. This slurry was then cast onto aluminium foil, copper foil or glass (for self-supporting electrodes) using a doctor blade, which allowed the thickness to be set. Circles of 13 mm were then cut from these materials. These materials were then ready to be made into cells. The composition of the mixture was kept constant for all experiments.

For galvanostatic cycling and potentiodynamic cycling with galvanostatic acceleration (PCGA) two-electrode cells were assembled (fig.2.6). The active

material was tested versus lithium, run as the cathode, using a disk of lithium (in excess) as the anode. The two electrodes were separated by a glass fibre pad soaked in the electrolyte (normally 1 M $LiPF_6$ in ethylene carbonate /dimethyl carbonate 1:1, LP-30 Merck Selectipur, Battery Grade). This was then sealed into a coin cell (supplied by National Research Council of Canada. Cells were sealed in a glove box in air and moisture free conditions (O_2 < 0.1 ppm; H_2O < 0.1 ppm).

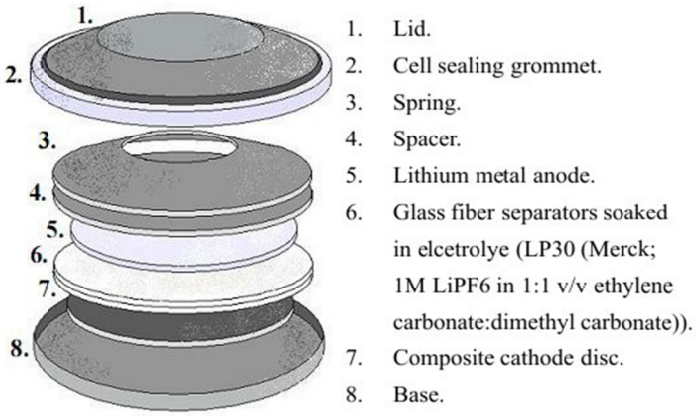

Figure 2.6 Expanded views of a coin cells.

The typical composition of the electrode consisted of 75 % active material (synthesised TiO_2), 15 % conductive carbon (Super P, MMM Carbon) and 10 % binder (PVdF, Kynar).

2.11 Electrochemical Methods

2.11.1 Galvanostatic Cycling

Galvanostatic cycling (or cyclic chronopotentiometry) is an important method for electrochemical evaluation of battery materials, where a constant current is applied between the working and counter electrodes and the resulting potential is measured as a function of time. A typical profile is shown in figure 2.7. When charging, a positive current is applied, causing an oxidation of the working electrode until a set upper potential limit is reached. On discharge, a negative current is applied until a lower limit is achieved and a reduction of the working electrode occurs.

The voltage range investigated must be wide enough to give access to the potentials at which the redox process of Li insertion and removal occur, yet narrow enough to avoid detrimental oxidation and reduction of the electrolyte.

Lithium insertion/removal on charge/discharge occurring via a two phase process gives a flat constant potential (*plateau*) in the voltage profile, e.g. figure 2.8. Lithium insertion/removal occurring by a single solid solution process tends to give a sloping voltage profile.

Theoretically the profiles during charge and discharge should coincide, however, experimentally this does not happen; this is due to different over-voltage phenomena, e.g. IR drops caused by the resistivity offered by the electrolyte. In this case the difference between the theoretical and experimental value of the voltage plateau follows Ohm's law.

The specific capacity (Q) of the electrode, as previously defined in paragraph 2.10.1 (eq.16), is the total amount of current (I) passed per unit mass (m) of electrode material during the time (t) necessary for complete discharge or charge[10]:

$$Q = I\,t\,/m \quad (16)$$

During the experiment, the cell voltage (V) is plotted as a function of the specific capacity (Ah g^{-1}). For an anode material, the so called *coulombic efficiency* (η) is defined as the ratio of the value of the capacity in charge and discharge.

$$\eta = Q_{charge}/Q_{discharge} \quad (17)$$

The *cyclability* of the material is a measure of the variation of the *capacity retention*, which is defined as the ratio:

$$Q_{ith\ cycle}/Q_{1st\ cycle} \quad (18)$$

and is usually displayed as the total charge (or discharge) capacity as a function of cycle number (figure 2.9).

The maximum theoretical capacity, Q, for an electrode compound M, into which the following insertion/removal process occurs

$$Li_xM + \Delta xLi^+ + \Delta e^- \leftrightarrows Li_{x+\Delta x}M$$

Can be calculated by:

$$Q = \frac{nF}{M\,3.6} \quad (19)$$

where n is the number of electrons exchanged during the process, F is Faraday's constant (96485 C mol^{-1} or 26.801 Ah mol^{-1}) and M is the molecular mass (g mol^{-1}).

Experiments were performed on either Biologic Macpile II or a Maccor Series 4000 battery cycler.

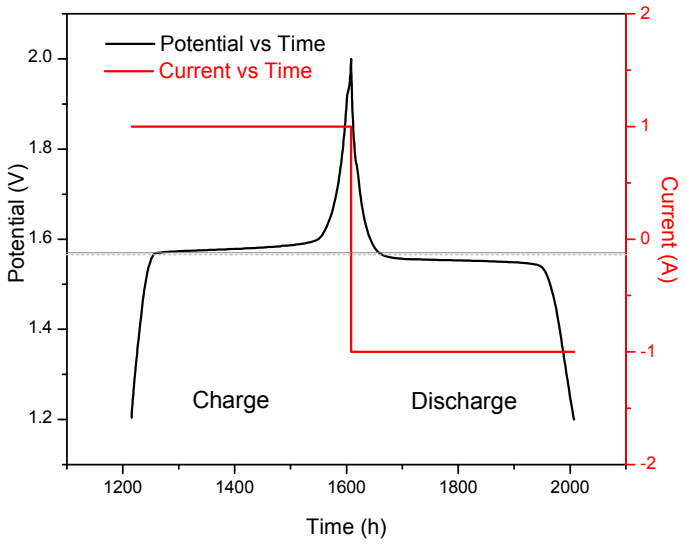

Figure 2.7 Variation of potential (—) and current (—) as a function of time during charge and discharge processes in a galvanostatic cycling experiment.

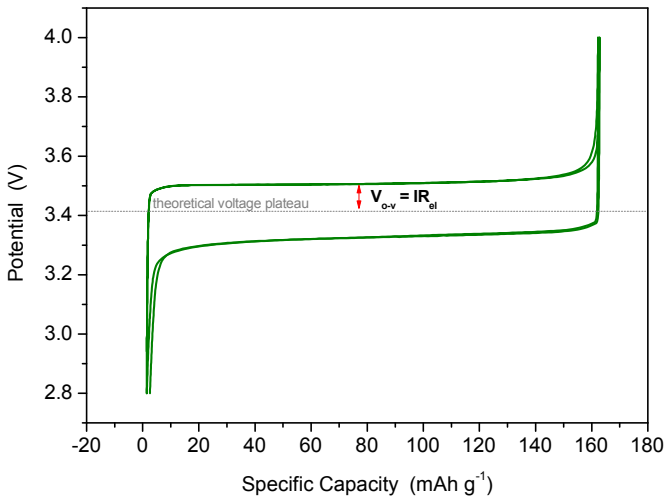

Figure 2.8 Variation of potential with state of charge for a galvanostatic cycling experiment, highlighting the over voltage effect.

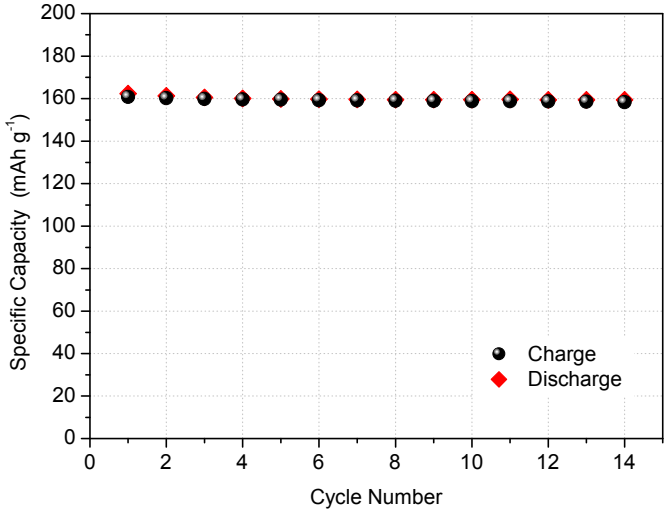

Figure 2.9 Variation of specific capacity, charge and discharge, with cycle number for a galvanostatic cycling experiment showing excellent capacity retention.

2.11.2 Potentiodynamic Cycling with Galvanostatic Acceleration (PCGA)

The potentiodynamic cycling with galvanostatic acceleration (PCGA) technique consists of discharging and charging the battery by iteration of 5 mV potential steps for either a predetermined time (9 h) or until the current decreases below a certain value. In all work carried out in this thesis this value set at 5 mA g^{-1}, corresponding to an equivalent galvanostatic regime.

The information provided by this technique is the evolution of current as a function of time during the discharge and charge; it is particularly suitable for the recognition, of phase domains evolved during these processes[11]. Compared with a standard cyclic voltammetry method, the PCGA measurements describes the thermodynamics of the electrochemical processes rather than the kinetics.

For the purpose of this work, PCGA measurements were performed on coin cells using a Biologic VMP3 multichannel cycler.

2.11.3 A.C. Impedance

Electrochemical Impedance Spectroscopy, EIS, employs the application of a.c. signals of selected frequencies and small amplitude (5-10 mV). By varying the frequency of the signal, a selective perturbation of different physic-chemical phenomena can be performed, thus allowing the identification of their separate contributions.

The response is usually interpreted in terms of equivalent circuit, i.e. the electrical circuit (a combination of electrical components connected in series/parallel) which gives the same response as the investigated real system. Each component represents a certain phenomenon (faradic resistance, solution resistance, double layer capacitance, etc.).

The impedance of an electrode or a battery is given by the following expression:

$$Z = R + j\omega X \quad (20)$$

where $= \omega L - \frac{1}{\omega C}$, $j = \sqrt{-1}$ and ω is the angular frequency ($2\pi f$); L is the inductance and C the capacitance.

In an ideal electrode, activation processes exhibit a semicircular behaviour with a frequency that is characteristic of relaxation processes; concentration processes exhibit a 45° behaviour characteristic of diffusion processes, also known as Warburg behaviour. Ohmic polarizations have no capacitive character and do not depend on frequency.

The frequency of the maximum, f_m, of the semicircle give the relaxation time:

$$\tau = 1/f_m = RC \quad (21)$$

Where R is related to the exchanged current for the reaction and C is the polarisation capacitance Cp, usually of the order of the hundreds of μF cm^{-1}, which is almost ten times larger than the double layer capacitance, C_{DL}, at the electrode-solution interface.

Each electrode reaction has a distinctive, characteristic impedance signature. Usually, battery electrodes have large surface areas and, therefore, show large capacitances. It is common for cells to have a capacitance of farads and resistance of milliohms[9].

Impedance data are usually represented in the Nyquist plot (imaginary part of Z, Z_{im}, *vs* its real part, Z_{real}) and the Bode plot (Z modulus and φ *vs* ω), but several other representation plots can be used (e.g. Z_{real} and Z_{im} *vs* ω).

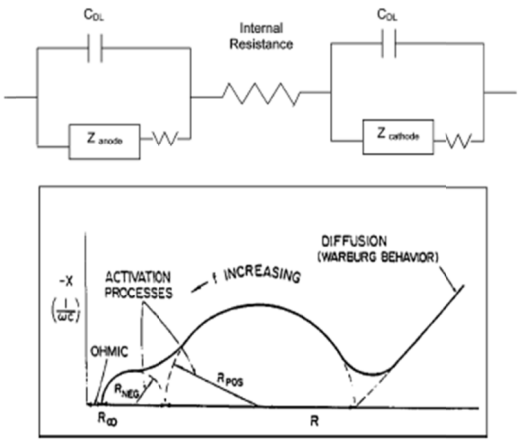

Figure 2.10 Simple battery circuit diagram (top); Corresponding Argand diagram of the behaviour of the impedance with frequency f for an idealised battery system where the characteristic behaviours of ohmic, activation and diffusion are shown (bottom). (Reprinted from reference 11, Copyright (2002), with permission from ACS journals)

References

1. Cheetham , A.K. and Day, P. *Solid State Chemistry Techniques* Oxford University Press (1991).

2. Bragg, W.L. Proc. *Camb. Phil. Soc.* (1912) **17** 43.

3. Bruker AXS ltd, TOPAS V3.0: *General Profile and Structure Analysis Software for Powder Diffraction Data*. 2004.

4. Reitveld, H.M. *Acta Cryst*., (1969) **2** 65.

5. Brunauer, S.; Emmett, P.H.; Teller, E. *J. Am. Chem. Soc.* (1938) **60** 309.

6. Long, D.A., *Raman Spectroscopy*, McGraw-Hill International Book Company 1977.

7. Hardwick, L.J.; Holzapfel, M.; Novak, P.; Dupont, L.; Baudrin, E. *Electrochimica Acta* (2007) **52** 5357–5367.

8. Ratner, B.; Castner, D. *Electrospectroscopy for Chemical Analysis in Surface Analysis*, Editor J.C. Vickerman, Wiley 1997.

9. Winter, M. and Brodd, R.J. *Chem. Rev.* (2004**) 104** 4245-4269.

10. Vincent, C.A. and Scrosati, B. *Modern Batteries, 2nd Edition*, Arnold Publ. Ltd., London, 1997.

11. Morcrette, M.; Calin, C. and Masquelier, C. *Solid State Sci.* (2002) **4** 239.

Chapter 3

Synthesis and Characterisation of TiO_2(B) materials

3.1 Introduction

Titanium dioxide, TiO_2, materials have received much attention in recent years due to their potential use in a wide variety of applications ranging from catalytic supports, photocatalysts, solar energy conversion, gas sensing and intercalation electrodes for rechargeable lithium batteries or supercapacitors.

Titanium dioxide is present in nature as different polymorphs, however, not all of these have the ability to intercalate lithium within their structures. The only polymorphs that can intercalate Li in the bulk material are TiO_2(B) (335 mAh g^{-1})[1] and anatase (168 mAh g^{-1})[2], although all can do so in nanostructured form, including brookite and rutile[3-9]. TiO_2(B) is the fifth polymorph of titanium dioxide with an open structure which can host lithium, reaching almost 1 equivalent of lithium per formula unit resulting in a specific capacity of 330 mAh g^{-1}.[1]

It is for this reason that TiO_2(B) has created much interest for electrochemical applications as an alternative anode to graphite in lithium–ion batteries. Although, titanium dioxide works at a higher potential (1.5 V *vs* lithium) than graphite, the

intrinsic safety of the material combined with low toxicity and low cost are significant advantages over the conventional graphite anodes[10].

This work investigates and compares three morphologies of TiO_2(B). In this chapter the synthesis of the three morphologies; bulk, nanowires and nanotubes are reported together with the physical characterisation of the investigated materials.

3.2 Synthesis procedures

3.2.1 Synthesis of bulk TiO_2(B)

Bulk TiO_2(B) was prepared via the layered precursor $K_2Ti_4O_9$[11]. Stoichiometric amounts of TiO_2 (anatase, Aldrich 99.8 %) and K_2CO_3 (Fisher, 99 %) were ground together using an agate mortar and pestle and subsequently calcined in air at 800 °C for 15 h. The product was ground again and calcined for a second time under the same conditions to produce single phase $K_2Ti_4O_9$. The product was subjected to proton exchange by stirring it at room temperature for 72 h in 3 M hydrochloric acid, in order to form isostructural $H_2Ti_4O_9$. The product was filtered, washed with distilled water and dried at 80 °C overnight. In order to form TiO_2(B) the resulting powder was annealed in air at 400 °C for 4 h.

3.2.2 Synthesis of TiO_2(B) nanowires and nanotubes

In 1998 Kasuga *et al*. first reported the synthesis of TiO_2 nanotubes via a simple hydrothermal procedure, with no requirement for sacrificial templates[12]. Initially the nanotubes were believed to be composed of anatase, however, this assumption was called into question by Du *et al*.[13] and further investigation suggested that these

nanotubes were composed of the layered titanate $(Na,H)_2Ti_3O_7$ instead. Further work by a variety of research groups has confirmed the titanate nature of the nanotubes[14-15]. However, the successful synthesis of the titanate nanotubes by Kasuga paved the way for the synthesis of titanium dioxide nanotubes and nanowires.

In this work two 1D nano-morphologies were investigated. Titanate nanotubes and nanowires were synthesised, following hydrothermal procedures previously reported by Armstrong *et al.*[16,17]. The synthetic procedures for both titanate nanowires and nanotubes are very similar; however, they differ in a few crucial points, such as the molarity of the sodium hydroxide solution and the temperature used during the hydrothermal treatment. The optimised synthesis conditions for each of the different morphologies are reported in table 3.1.

In a typical experiment a calculated amount of titanium dioxide (anatase, Aldrich 99.8 %) was dispersed in an aqueous solution of NaOH (12 or 15 M). After the mixture was stirred for 1 h, the resulting suspension was transferred to a Teflon-lined reaction vessel and treated at 150-170 °C for 72 h, depending on the desired morphology. The product was acid washed, which involved stirring the sample in 0.1 M HCl solution for 2 h. The material was then filtered, washed with distilled water until a neutral pH was reached, and dried at 80 °C overnight under vacuum. The TiO_2(B) nano-morphologies were obtained by annealing the acid-washed titanate at 400 °C for 2 h in air.

Sample	NaOH M	Na/Ti	Hydrothermal process conditions	Annealing conditions
TiO_2(B) nanowires	15	13.5	170 °C for 72 h	400 °C for 2 h 150 °C h^{-1}
TiO_2(B) nanotubes	12	11.6	150 °C for 72 h	400° C for 2 h 150 °C h^{-1}

Table 3.1 Synthesis conditions of TiO_2(B) nanowires and nanotubes.

3.2.3 The mechanism of the hydrothermal growth of nanostructured titanates

An understanding of both the formation mechanism and how the synthesis conditions affect the properties of the nanostructured materials is extremely important in order to tailor the material to specific needs.

Since Kasuga reported the synthesis, many attempts have been made to describe the mechanism of formation of the titanate nanotubular structure from raw TiO_2. Initially Kasuga *et al*. suggested that the nanotubular morphology occurred during the post hydrothermal acid washing[18]. This hypothesis is still maintained by other researchers[19]; however it was demonstrated by washing the samples with other solvents, such as ethanol and acetone[13, 20], that the nanotubular sodium titanate is actually formed during the alkaline hydrothermal process.

It has since been observed that all titanate nanotubes produced via alkaline hydrothermal treatments have multi-layered walls. Following this observation, Walsh *et al*. have highlighted the fact that the transformation of the titania in strong alkaline conditions and the resulting formation of single-layered and multi-layered titanate nanosheets play a key role in the production of the nanotubular morphology[21]. The

authors also suggested that the transformation of raw TiO_2 to nanotubular titanate occurs in several stages: the partial dissolution of raw TiO_2 accompanied by the epitaxial growth of layered nanosheets of sodium trititanate; the exfoliation of nanosheets; crystallization of dissolved titanate on nanosheets resulting in mechanical tensions, which induce the curving and wrapping of nanosheets into nanotubes; growth of nanotubes along the length and exchange of sodium ions to protons[21, 22].

When the alkaline hydrothermal treatment exceeds a temperature of 170 °C and/or the experiment is carried out in the presence of a concentrated alkaline solution, the formation of titanate nanofibres occurs[21, 22].

3.3 Characterisation

3.3.1 Structural analysis

The crystal structure of TiO_2(B) is monoclinic (space group C2/m). A diagrammatical representation of the structure is shown in figure 3.1. It is similar to other polymorphs of TiO_2, as it is composed of TiO_6 octahedra sharing corners and edges; however this polymorph has an open structure with perovskite-like channels. This open structure allows facile Li^+ transport within the framework and it is therefore responsible for the superior intercalation of Li^+, compared with the other titania polymorphs.

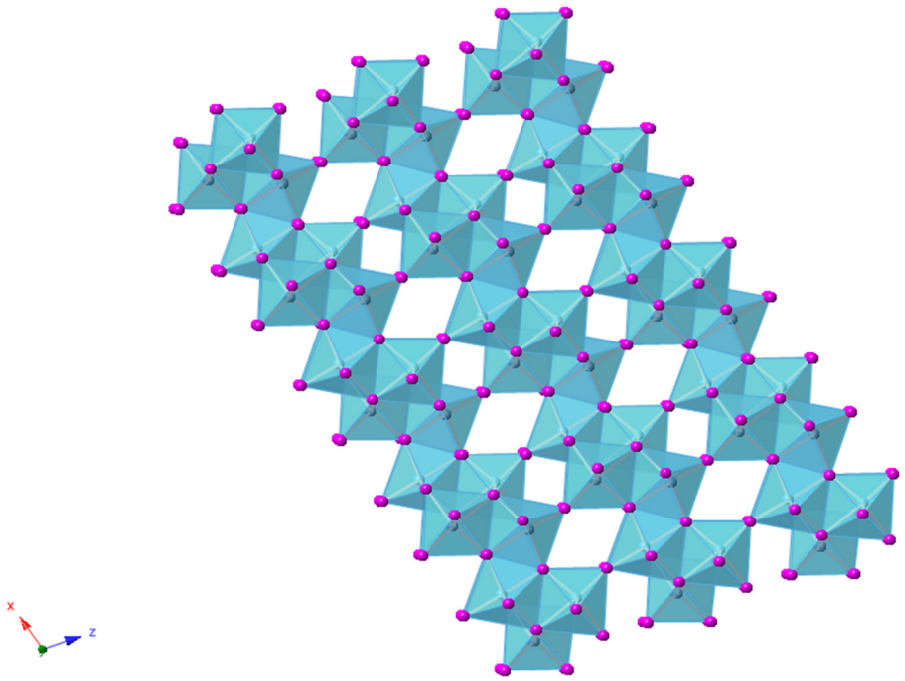

Figure 3.1 Diagrammatical representation of the TiO_2(B) structure.

Powder X-ray diffraction was used to investigate the crystal structure of the produced TiO_2(B) samples. In figure 3.2 the XRD patterns of the materials under investigation are reported together with the calculated pattern of TiO_2(B).

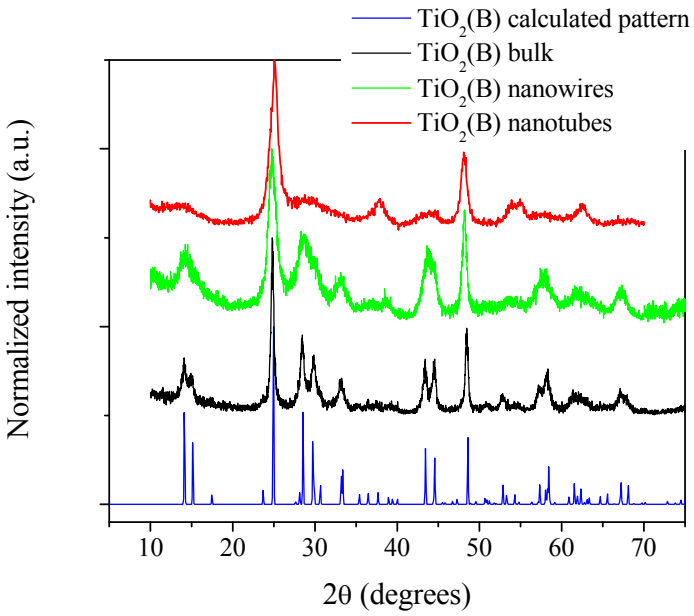

Figure 3.2 Experimental XRD pattern of bulk TiO_2(B) (in black); TiO_2(B) nanowires (in green); TiO_2(B) nanotubes (in red) and the TiO_2(B) calculated pattern (in blue).

Here the powder diffraction patterns of TiO_2(B) nanowires and nanotubes are compared with that of bulk TiO_2(B). In both bulk and nanowire samples no significant evidence of the presence of other TiO_2 phases was observed. In the nanotube pattern, however, traces of the anatase phase were found.

As expected, the peaks of the nanowires are much broader than those in the bulk sample. The peak broadening is due to the reduced dimensions of the nano-structured material, going from 0.1-0.5 μm to 20-50 nm, which results in an X-ray coherence length smaller than 600 Å. The peak broadening effect is much more pronounced for

the nanotube sample, since the tubes have a wall thickness ranging between 25 and 30 Å.

The structure of the TiO_2(B) samples was further investigated using Raman spectroscopy. The Raman spectra are presented in figure 3.3.

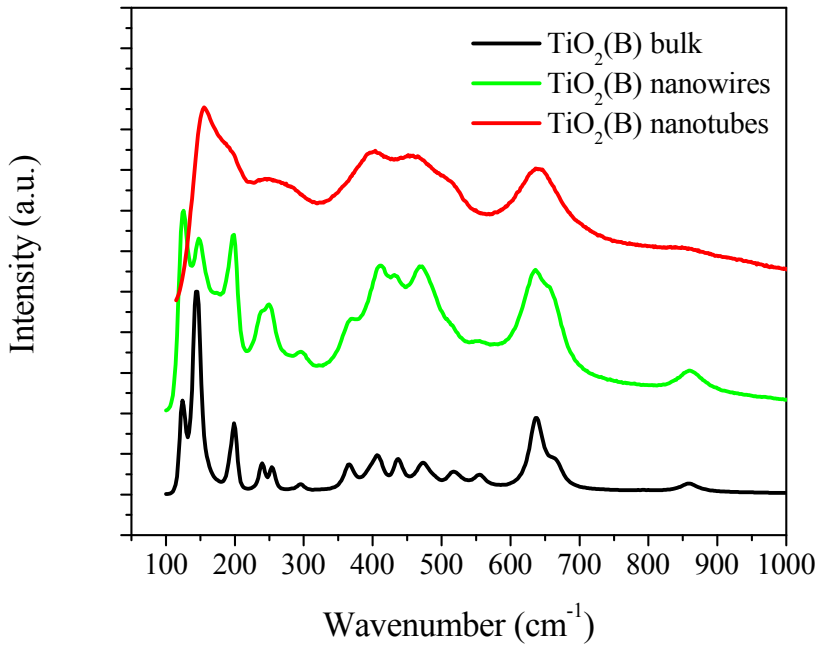

Figure 3.3 Raman spectra of bulk TiO_2(B) (in black); TiO_2(B) nanowires (in green) and TiO_2(B) nanotubes (in red).

The TiO_2(B) spectral features are present for all morphologies; however, as expected, the reduced dimensions of the nanostructured samples cause the peaks to broaden in the Raman spectra. This effect is particularly evident in the nanotube spectrum. Despite this, good agreement was observed between the spectra of the nanowire, nanotube and bulk TiO_2(B) samples.

3.3.2 Morphology

The morphology of the produced TiO_2(B) was examined using transmission electron microscopy (TEM) and scanning electron microscopy (SEM). In figure 3.4 TEM images of bulk TiO_2(B) are reported.

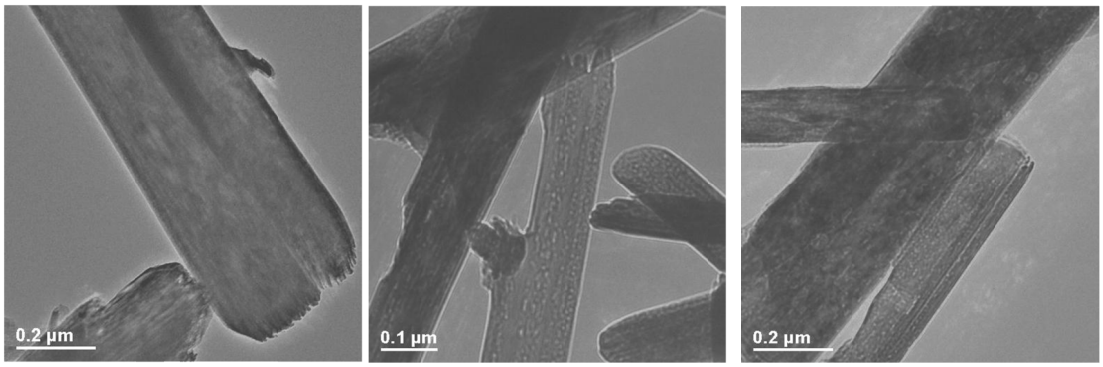

Figure 3.4 TEM images of bulk TiO_2(B).

The images clearly show a wire-like morphology for the bulk material. Figure 3.5 illustrates the TEM images for the TiO_2(B) nanowires. From the TEM image analysis an estimation of the nanowires dimensions can be made. The nanowires exhibit a diameter in the range of 20 nm to 50 nm and a length which can reach up to 10 μm.

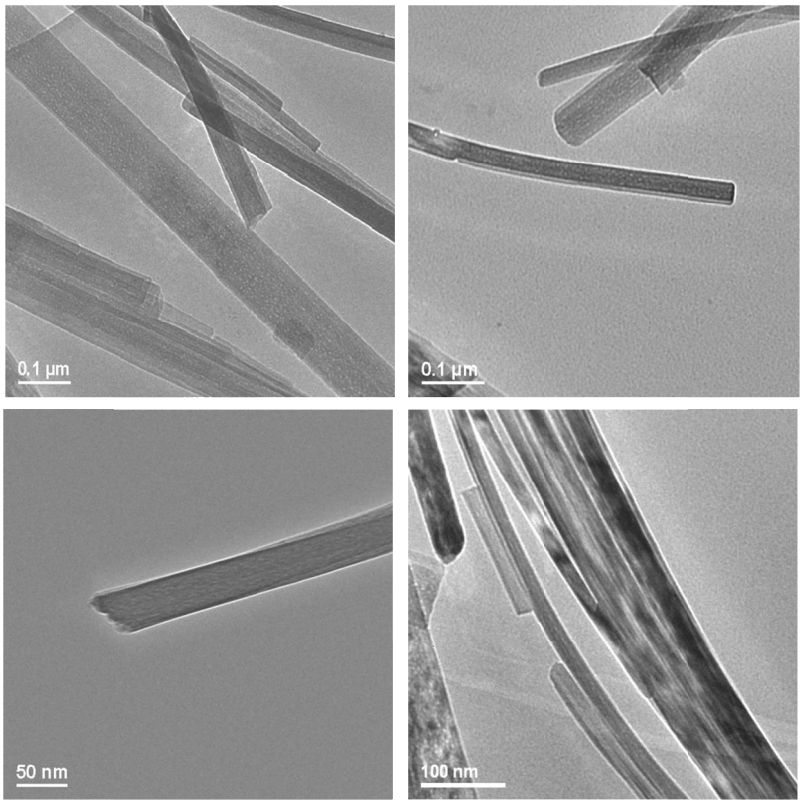

Figure 3.5 TEM images of TiO_2(B) nanowires.

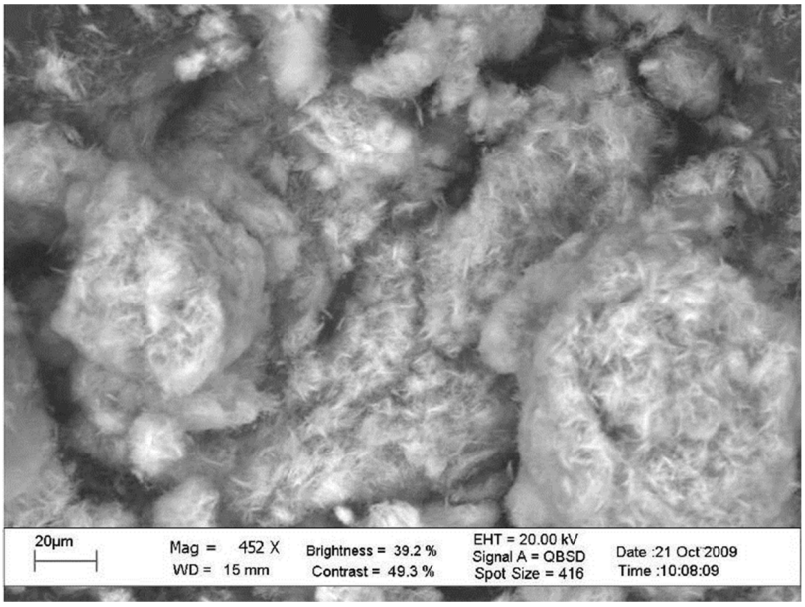

Figure 3.6 SEM image of TiO_2(B) nanowires.

Scanning electron microscopy (SEM) studies confirmed the high morphological homogeneity and the high quality of the sample, consisting mainly of fibrous nano-particulates. An image taken at the SEM is reported in figure 3.6.

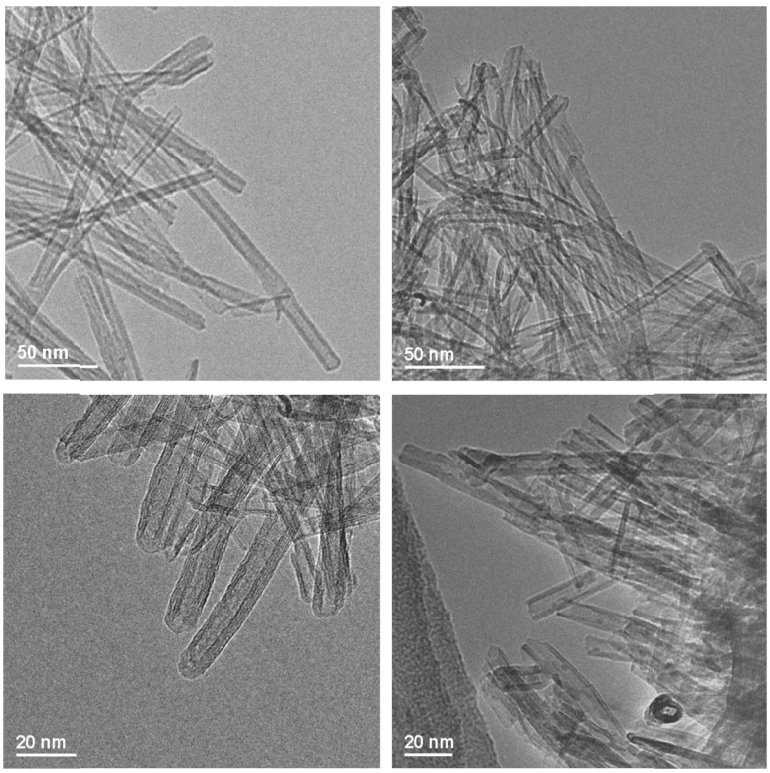

Figure 3.7 TEM images of TiO_2(B) nanotubes.

The TEM images reported in figure 3.7 clearly highlight the nanotubular morphology of the sample. An estimate of the size was obtained by TEM image analysis; the nanotubes show an outer diameter of 8-12 nm and an internal diameter of 5-8 nm. The material displayed high homogeneity.

3.3.3 Surface area analysis

Surface area measurements were carried out on the TiO_2(B) samples and the nanotube titanate precursor using the Brunauer-Emmett-Teller (BET) method. The obtained surface area values are reported in table 3.2.

BET Surface area (m^2 g^{-1})	
Bulk TiO_2(B)	18.4
TiO_2(B) nanowires	27.7
TiO_2(B) nanotubes	205-215
Titanate nanotubes	240

Table 3.2 Surface area values for the TiO_2(B) samples and the titanate nanotube precursor.

As expected, the nanowires exhibit a larger surface area (~28 m^2 g^{-1}) compared with the bulk material (~18 m^2 g^{-1}). The nanotube precursor has a very large surface area which is almost one order of magnitude larger than the nanowire sample. However, after the annealing and the formation of the TiO_2(B) structure, the surface area of the nanotubes decreases. This is believed to be due to damage sustained by some of the nanotubes which occurs during the calcination stage, leading to the partial collapse of the nanotube morphology.

3.4 Chapter conclusions

Three morphologies of TiO_2(B) were successfully synthesised. Bulk TiO_2(B) was prepared via the layered precursor $K_2Ti_4O_9$. Nanowire and nanotube samples of TiO_2(B) were prepared via a hydrothermal route. Specific conditions for the hydrothermal treatment led to the formation of single-layer nanosheets of sodium titanate followed by the scrolling of the sheets which produces the nanotube morphology. When the Na/Ti ratio was increased and the temperature of the hydrothermal process exceeded 170 °C, the formation of nanowires occurred.

These materials were fully characterised using several techniques including XRD, TEM, SEM and BET surface area measurements.

References

1. Marchand, R.; Brohan, L. and Tournoux, M.; *Material Research Bulletin* (1980) **15** 1129.

2. Cava, R.J.; Murphy, D.W. and Zahurak, S.; *Journ. Solid State Chem.*,(1984) **53** 64-75.

3. Sudant, G.; Baudrin, E.; Larcher, D.; Tarascon, J.M.; *J. Mater. Chem.* (2005) **15** 1263.

4. Baudrin, E.; Cassaignon, S.; Koesch, M.; Jolivet; J.P.; Dupont L.; Tarascon, J.M.; *Electrochem. Commun.,* (2007) **9** 337.

5. Wagemaker, M.; Borghols,W.J.H.; Mulder, F.M.; *J. Am. Chem. Soc.* (2007) **127** 4323.

6. Reddy, M.A.; Kishore, M.S.; Pralong, V.; Varadaraju, U.V.; Raveau, B. *Electrochem. Solid-State Lett.*; (2007) **10** A29.

7. Borghols, W.J.H.; Wagemaker, M.; Lafont, U.; Kelder, E.M.; Mulder, F.M. *Chem. Mater.* (2008) **20** 2949.

8. Hu, Y.-S.; Kienle, L.; Guo, Y.-G.; Maier, *J. Adv.Mater*. (2006) **18** 1421.

9. Dambournet, D.; Belharouak, I. and Amine, K. *Chem. Mater.*(2010) **22** 1173-1179.

10. Armstrong, A.R., Armstrong, G.; Canales, J.; Garcia, R.; Bruce, P.G. *Adv. Mater.* (2005) **17** 862.

11. Armstrong, A.R.; Arrouvel, C.; Gentili, V.; Parker, S.C.; Saiful Islam, M. and Bruce, P.G. *Chem. Mater.* (2010) **22** 6426–6432.

12. Kasuga, T.; Hiramatsu, M.; Hoson, A.; Sekino, T.; Niihara, K. *Langmuir* (1998) **14** 3160.

13. Chen, Q.; Zhou, W.; Du, G.; Peng, L.M. *Adv. Mater.* **2002**, *14*, 1208.

14. Sun, X. and Li, Y. *Chem-Eur J.* (2003) **9** 2229.

15. Yang, J.; Jin, Z.; Wang, X.; Li,W.; Zhang, J.; Zhang, S.; Guo, X. and Zhang, Z. *J. Chem. Soc.*, *Dalton Trans.* (2003) 3898.

16. Armstrong, A.R.; Armstrong, G.; Canales, J.; Bruce, P.G., *Angew. Chem., Int. Ed.* (2004) **43**, 2286-2288.

17. Armstrong, G.; Armstrong, A.R.; Canales, J. and Bruce, P.G., *Chem. Commun.* (2005) 2454-2456.

18. Kasuga, T.; Hiramatsu, M.; Hoson, A.; Sekino, T.; Niihara, K. *Adv. Mater.* (1999) **11** 1307.

19. Tsai, C.C. and Teng, H. *Chem. Mater*. (2006) **18** 367-373.

20. Zhang, M.; Jin, Z.; Zhang, J.; Guo, X.; Yang, J.; Li, W.; Wang, X.; Zhang, Z. *J. Mol. Catal. A* (2004) **217** 203.

21. Bavykin, D.V.; Friederich, J.M.; and Walsh, F.C. *Adv. Mater.* (2006) **18** 2807–2824.

22. Bavykin D.V. and Walsh F.C., *Titanate and Titania Nanotubes*, RSC Nanoscience and Nanotechnology, RSC publishing, 2010.

Chapter 4

Electrochemical performance of TiO_2(B) materials

4.1 Introduction

In this chapter the electrochemical performance of the TiO_2(B) bulk, nanowires and nanotubes is reported. In particular, the capability of the different morphologies to intercalate lithium is compared both at low and high rates and also their performance over a large number of cycles was tested. The investigation of the mechanism of lithium insertion using neutron powder diffraction is discussed for both bulk TiO_2(B) and nanowires. In addition, *ex situ* and *in situ* Raman microscopy experiments have been carried out on bulk TiO_2(B) and nanotubes for the first time, to help characterise the intermediate stages of lithium uptake during charge and discharge.

4.2 Electrochemical performance

4.2.1 Load curves

The variations of voltage with lithium content for TiO_2(B) bulk, nanowires and nanotubes are presented in figure 4.1. All three materials under investigation exhibit a very similar voltage profile, suggesting that the same redox processes occur in all of the materials.

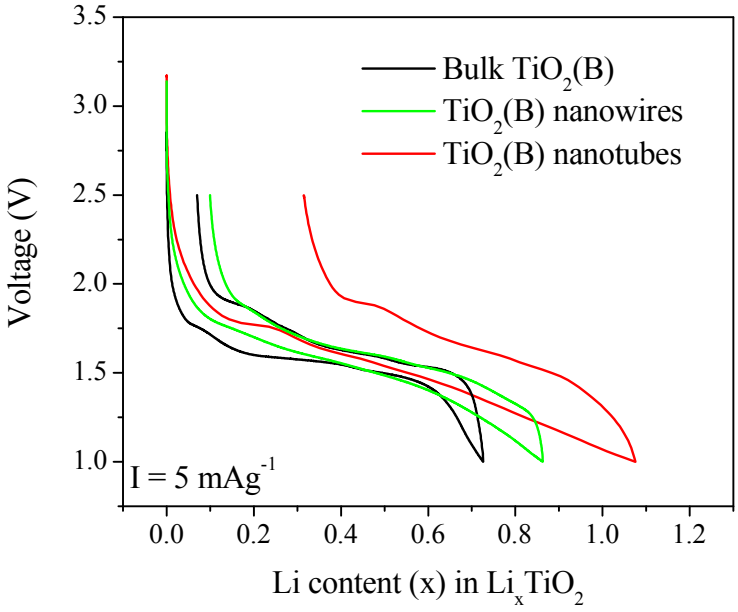

Figure 4.1 Load curves of different TiO_2(B) morphologies : bulk (black); nanowires (green) nanotubes (red) recorded during PGCA measurements with a current rate of 10 mA g^{-1}.

The load curves appear not to be smooth functions of lithium content; instead they consist of a series of plateaux and sloping regions; the former can be identified as two-phase regions and the latter as solid solutions.

Analysis of the TiO_2(B) samples load curves shows two plateaus that can be clearly distinguished. The first is observed at 1.75 V, whereas a second, much larger one is observed at 1.5 V.

The location of the plateaus are more clearly visible in the bulk TiO_2(B) differential capacity plot, presented in figure 4.2, in which the derivative of the state of charge with respect to the potential is displayed. (The incremental capacity plots provide a useful and well-established means of probing the load curves in more detail.)

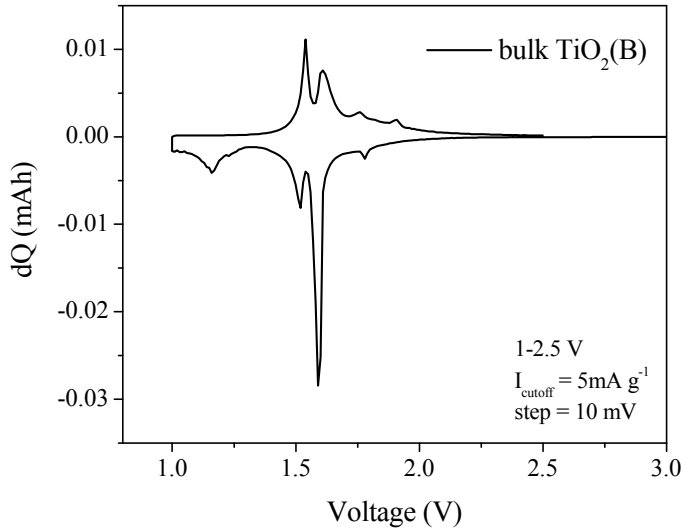

Figure 4.2 Bulk TiO_2(B) incremental capacity plot, recorded during PGCA measurements, collected n a voltage range between 1-2.5 V with a current cut-off of 5 mA g^{-1} and step of 10 mV.

In the plot three different peaks are recognisable: the first at 1.75 V, and two further peaks at 1.55 V and 1.45 V, which in the load curve were observable as one large region.

As can be seen from the bulk material load curve, 0.72 equivalents of lithium were inserted into the TiO_2 structure, corresponding to a discharge capacity in the first

cycle of 241.8 mAh g^{-1}. The corresponding curve for the nanowires appears much smoother.

The capacity to intercalate lithium in the structure is greater for the TiO_2(B) nanowires compared with the bulk material. The uptake of lithium in the structure was 0.87, which corresponds to a specific capacity of 291.4 mAh g^{-1}. Good correspondence is also observable in the differential capacity plots, reported in figure 4.3, where the three peaks of the two-phase regions are still clearly recognisable, though the peaks are smoother and broader.

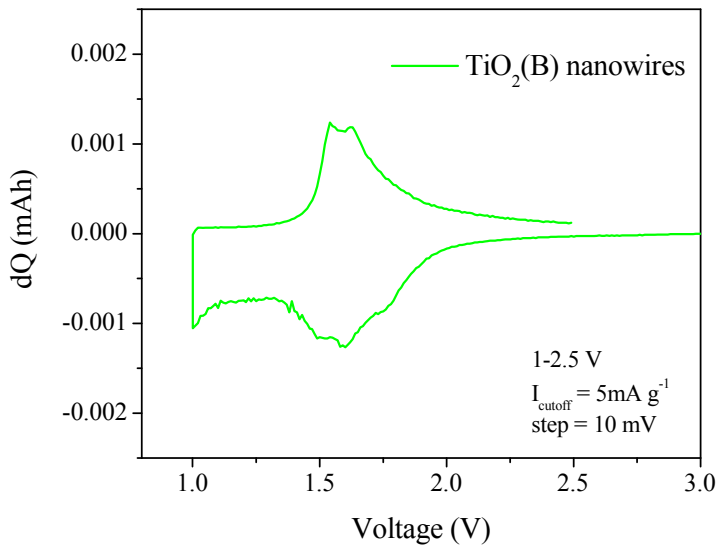

Figure 4.3 TiO_2(B) nanowires incremental capacity plot, recorded during PGCA measurements, collected n a voltage range between 1-2.5 V with a current cut-off of 5 mA g^{-1} and step of 10 mV.

As can be noted from figure 4.1, the nanotubes show an extraordinary discharge capacity at the first cycle, exceeding one equivalent of lithium accommodated, and equal to a capacity of 360 mAh g^{-1}. This greater discharge capacity is believed to be

due to the larger surface area exhibited by the nanotubes, (205 m^2 g^{-1} compared with the 28 m^2 g^{-1} shown by the nanowires), suggesting that an additional charge storage mechanism is present. The nanotubes load curve also shows greater polarisation compared with that of the nanowires and the bulk material. The larger polarisation exhibited seems to be related to the reduced dimensions of the sample.

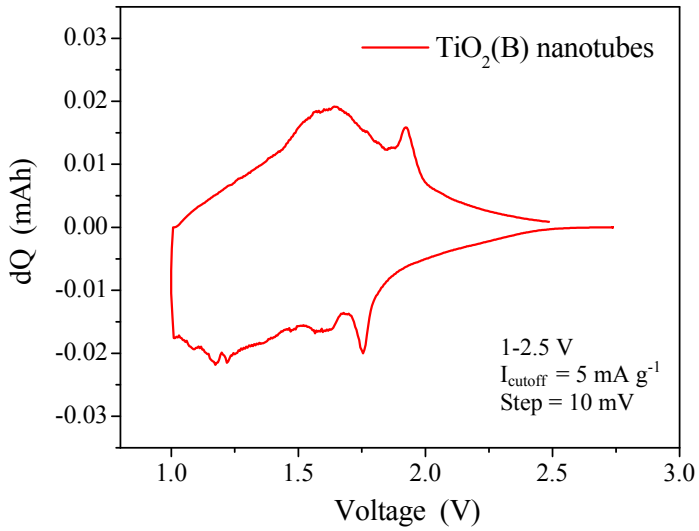

Figure 4.4 TiO_2(B) nanotubes incremental capacity plot, recorded during PGCA measurements, collected n a voltage range between 1-2.5 V with a current cutoff of 5 mA g^{-1} and step of 10 mV.

The larger polarisation is evident in the incremental capacity plot. In the plot presented in figure 4.4, the typical TiO_2(B) features at 1.55 V and 1.45 V are still recognisable. However the peak at 1.75 V is covered by a more intense peak at 1.65 V which can be associated with anatase phase impurities.

4.2.2 Galvanostatic cycling

The galvanostatic cycling of the material under investigation is presented in figure. 4.5. The measurements were performed at room temperature at a charge/discharge rate of 100 mA g^{-1}, C/3, where C corresponds to complete discharge in one hour. All the electrodes were prepared by casting, with an electrode composition of 75 % active material, 15 % carbon and 10 % binder.

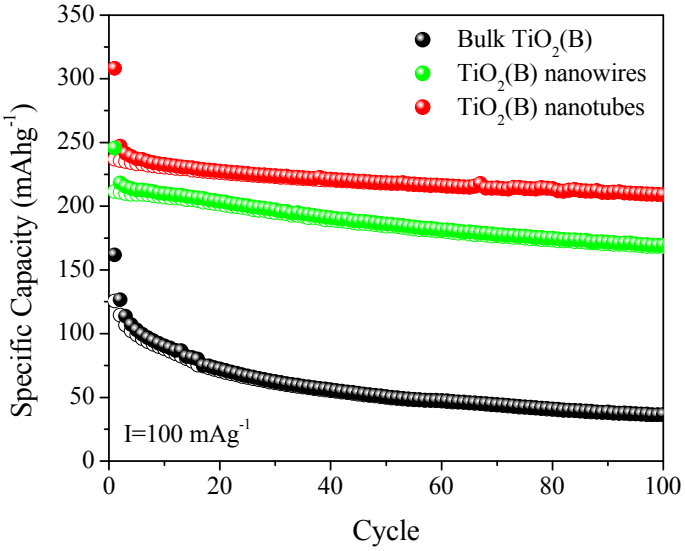

Figure 4.5 Specific capacities in charge (hollow) and discharge (filled) over 100 cycles for different TiO_2(B) morphologies: bulk (black); nanowires (green) nanotubes (red) .

As can be observed, the bulk material exhibits a lower value of discharge capacity at the first cycle, which fades thereafter. However, it is important to note that in order to obtain the optimum rate capability for any material, it is necessary to optimise the composite electrode manufacturing (e.g. electrode composition), which in this case has not been carried out for the bulk material.

As previously observed at a low rate (5 mA g^{-1}), and also at a higher charge /discharge rate (100 mA g^{-1}), the nanotube electrode shows a larger discharge capacity at the first cycle (320 mAh g^{-1}). This is believed to be due to the nano-sizing effect. In fact, the reduction in the dimensions of the material shortens the lithium diffusion path, thus enhancing the properties of this material.

TiO_2(B) nanowires exhibit good capacity retention of charge upon cycling, however the nanotube electrode have better capacity retention.

4.2.3 Coulombic efficiency and irreversible capacity

It was noted that at both low and high cycling rates there was a loss in the capacity between the first discharge and the first charge, as some of the charge gained during the discharge is not returned during charge and is therefore irreversibly lost. The coulombic efficiency (the ratio between the quantity of charge at the first charge and the first discharge) is a measure of this phenomenon. This behaviour is particularly evident for the nanotube based electrode. In table 4.1, the value of the irreversible capacity and the relevant coulombic efficiency at the first cycle for both current rates are reported for the samples under investigation.

Coulombic efficiency at 1st cycle			**Irreversible capacity (mAh g^{-1})**	
	I=100 mA g^{-1}	I=5 mA g^{-1}	I=100 mA g^{-1}	I=5 mA g^{-1}
TiO_2(B) nanotubes	77%	71%	71.11	105.62
TiO_2(B) nanowires	86%	88%	34	33.07
bulk TiO_2(B)	78%	90%	36.17	23.42

Table 4.1 Coulombic efficiency and irreversible capacity after the first cycle for the different TiO_2(B) materials run at 5 and 100 mA g^{-1}.

The nanotube electrode seems to be the most affected by the irreversible capacity, at both high and low rates, with remarkable loss in capacity of 105.62 mAh g^{-1} and 71.11 mAh g^{-1} for 100 and 5 mA g^{-1}, respectively. From these preliminary results, it appears that the irreversible capacity is related to the larger surface area exhibited by the nanotubes. However, the phenomenon of the irreversible capacity of the TiO_2(B) nanotubes will be discussed in more detail in chapter 5.

4.3 Li insertion mechanism for TiO_2(B) bulk and nanowires

In order to understand the process of the lithium insertion in the TiO_2(B) host material, it is important to establish the location of the lithium ions within the structure.

Broham and Marchand have described some possible intercalation sites for lithium in the TiO_2(B) structure and labelled them C, A1 and A2[1], as shown in figure 4.6. The C site is at the centre of the channel along the b-axis, surrounded by a square-planar arrangement of oxygen atoms. The A1 and the A2 sites are 5-fold coordinated, the first within the (001) plane and the latter lies between the oxygen atoms which bridge the adjacent layers in the (001) plane[1].

The three sites where lithium is inserted in the structure correspond to the three features observed in the differential capacity plots of the bulk TiO_2(B) and nanowires and are indicated in figure 4.7.

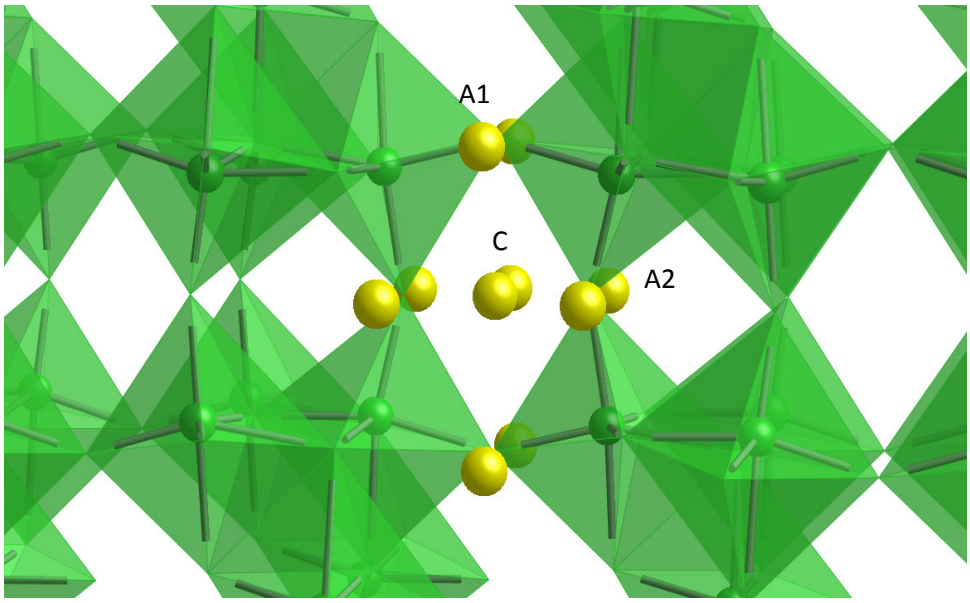

Figure 4.6 Bulk crystal structure of TiO_2(B) showing TiO_6 octahedra and lithium intercalation sites.

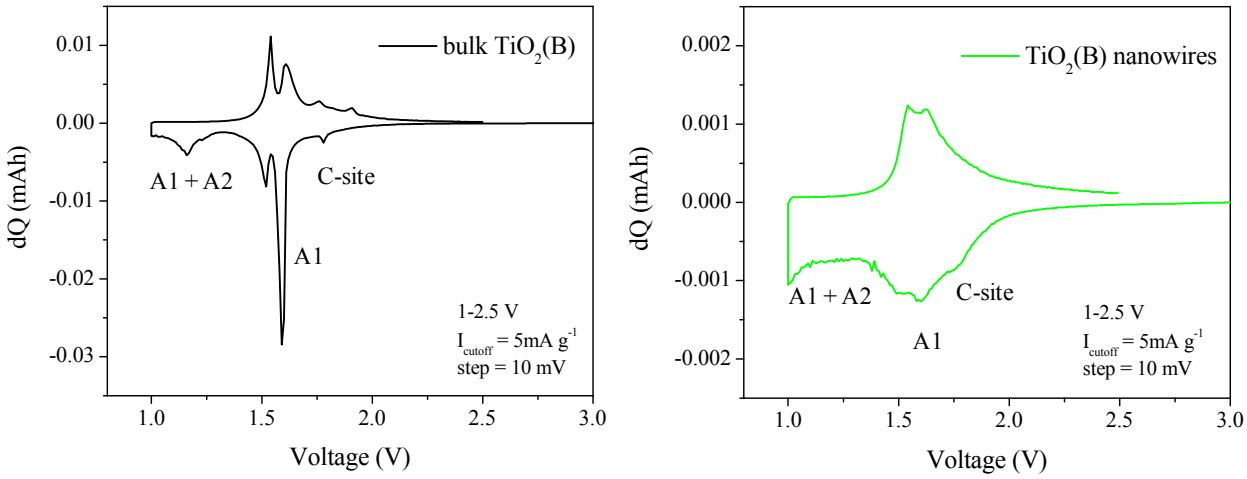

Figure 4.8 TiO_2(B) bulk and nanowires incremental capacity plots.

Powder neutron diffraction was used to investigate the structure of the TiO_2(B) at various lithiation stages. The experiments were performed on bulk TiO_2(B) and nanowires for three compositions: $Li_{0.15}TiO_2$; $Li_{0.5}TiO_2$ and $LiTiO_2$[3]. Each composition studied crystallises in space group *C2/m*.

Time of flight powder neutron diffraction data were obtained on GEM and POLARIS diffractometers at ISIS at the Rutherford Appleton laboratory. The structures were refined by Dr A.R. Armstrong by Rietveld method, using the program TOPAS Academic[2].

$Li_{0.15}TiO_2$(B)

The data collected for $Li_{0.15}$ TiO_2 composition could not be fitted using a single phase, however successful fitting was achieved using two phases. These corresponded to TiO_2(B) and $Li_{0.25}TiO_2$(B). The coexistence of two phases at an average Li content of 0.15 is not compatible with the information obtained from the load curve, which suggests that such a composition should be found in the single phase region and before the beginning of the plateau. However, disagreement between the chemical and electrochemical lithiation is not unexpected. The diffraction data are consistent with lithium intercalation into only a portion of the material, resulting in a mixture of non-reacted TiO_2(B) and reacted $Li_{0.25}TiO_2$(B). The lithium coordination site for the lithiated phase was established by refinement and was found to be the C site, with some displacement along the *b* axis away from the ideal site. Anisotropic expansion is also observed upon lithium insertion, with a significant increase along the *a* axis, a moderate increase along the *b* axis and a slight

contraction along the *c* axis. A fit of the data are shown in figure 4.8 and the refined parameters are reported in table 4.2.

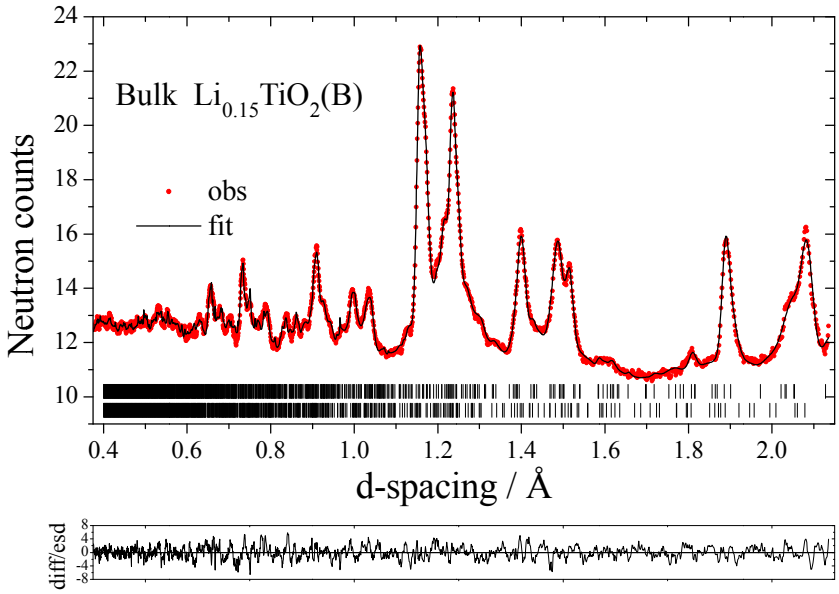

Figure 4.8 Refined powder neutron diffraction data for bulk $Li_{0.15}TiO_2$ (B) showing improved fit. Convergence achieved at Re=0.62 %, Rwp=1.15 %, Rp=0.93 %.

Phase	Space Group	a (Å)	b (Å)	c (Å)	β
$Li_{0.25}TiO_2$(B)	*C2/m,a*	12.884(5)	3.8019(8)	6.501(2)	108.72(4)°
Fractional coordinates					
	x	**y**	**z**	**B_{iso} (Å²)**	**Occupancy**
Ti_1	0.3051(15)	0.0	0.691(3)	0.32(6)	1
Ti_2	0.4139(18)	0.0	0.305(3)	0.32(6)	1
O_1	0.3393(12)	0.0	0.994(2)	0.46(3)	1
O_2	0.2317(12)	0.0	0.339(2)	0.46(3)	1
O_3	0.1227(11)	0.0	0.714(2)	0.46(3)	1
O_4	0.4266(9)	0.0	0.672(2)	0.46(3)	1
Li_1	0.0	0.33(2)	0.0	0.4	0.5

Table 4.2 Final parameter values for $Li_{0.15}TiO_2$(B) bulk refinement.

$Li_{0.5}TiO_2$(B)

A second sample with an average lithium content of 0.4 was examined. Once again, the diffraction pattern was best fitted using two phases, a mixture of $Li_{0.25}TiO_2$(B) and $Li_{0.5}TiO_2$(B), in agreement with the plateau observed in the load curves. Insertion of additional lithium leads to occupancy of an alternative site, the 5-coordinate A1 in the $Li_{0.5}TiO_2$(B) phase. Once this site is occupied the C-site is depopulated. A fit of the data are shown in figure 4.9 and the refined parameters are reported in table 4.3

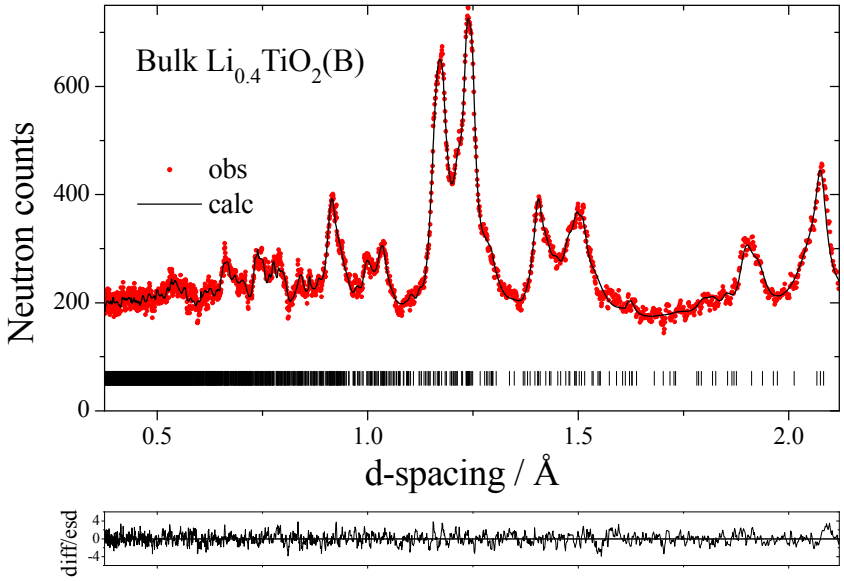

Figure 4.9 Refined powder neutron diffraction data for bulk $Li_{0.4}TiO_2$ (B) showing improved fit. Convergence achieved at Re=3.61 %, Rwp=5.48 %,Rp=4.54 %.

Phase	Space Group	a (Å)	b (Å)	c (Å)	β
$Li_{0.4}TiO_2$(B)	*C2/m,a*	12.451(5)	3.8168(8)	6.456(3)	107.78(3)°
Fractional coordinates					
	x	**y**	**z**	**B_{iso} (Å²)**	**Occupancy**
Ti_1	0.3128(16)	0.0	0.694(3)	0.1(1)	1
Ti_2	0.3991(17)	0.0	0.318(3)	0.1(1)	1
O_1	0.3508(14)	0.0	0.002(2)	0.41(5)	1
O_2	0.2325(12)	0.0	0.337(2)	0.41(5)	1
O_3	0.1270(11)	0.0	0.697(2)	0.41(5)	1
O_4	0.4507(14)	0.0	0.634(2)	0.41(5)	1
Li_1	0.928(3)	0.0	0.669(8)	0.4	1

Table 4.3 Final parameter values for $Li_{0.4}TiO_2$(B) bulk refinement.

Powder neutron diffraction was also carried out on the TiO_2(B) nanowires with a lithium content of 0.4 and it was found to have a similar behaviour to the bulk. The pattern fitted a mixture of two phases, $Li_{0.25}TiO_2$(B) and $Li_{0.5}TiO_2$(B), as expected from the load curves. The fit is reported in figure 4.10.

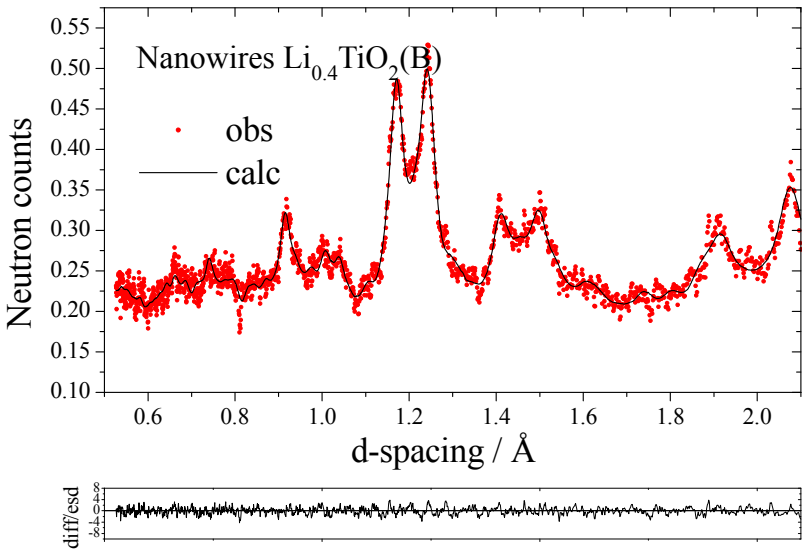

Figure 4.10 Refined powder neutron diffraction data for $Li_{0.4}TiO_2$ (B) nanowires showing improved fit.

Li_xTiO_2 (B), 0.5 < x < 1

The maximum lithium content that can be obtained, both chemically and electrochemically, corresponds to a composition for the bulk and nanowires of $Li_{0.8}TiO_2$(B) and $Li_{0.9}TiO_2$(B), respectively.

Insertion of lithium beyond x = 0.5 resulted in the occupation of a third coordination site A2, also with 5-coordinate lithium. For this lithium rich phase, lithium was found to partially occupy the A1-site along with partial occupancy of this new A2-site.

The diffraction patterns for both the bulk and nanowire samples were best fitted by a single phase. A misfit can be noted in the bulk sample refinement, at the d-spacing value of 1.5 Å, due to the presence of traces of lithiated anatase phase. The fit of the data are shown in figures 4.11 and 4.12 and the refined parameters are reported in tables 4.5 and 4.7.

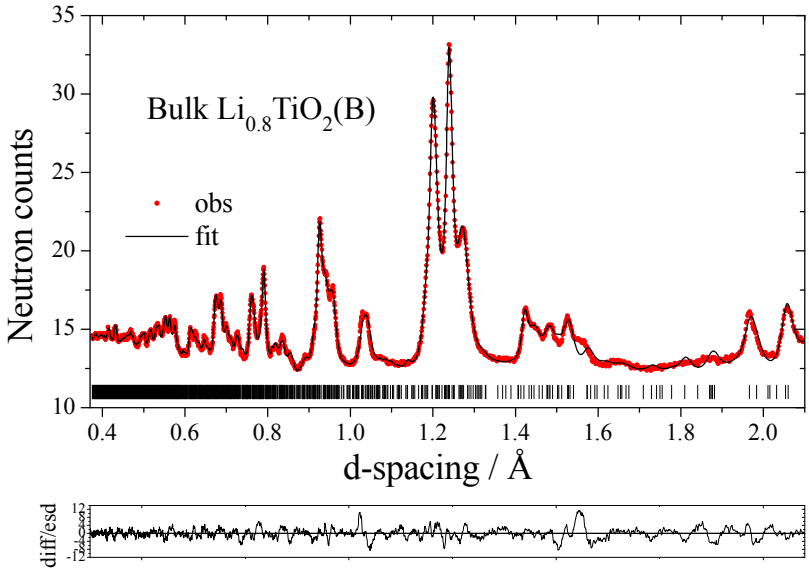

Figure 4.11 Refined powder neutron diffraction data for bulk $Li_{0.8}TiO_2$ (B) showing improved fit. Convergence achieved at Re=0.57 %, Rwp=1.44 %, Rp=1.07 %.

Phase	Space Group	a (Å)	b (Å)	c (Å)	β
$Li_{0.8}TiO_2$(B)	*C2/m,a*	12.7799(18)	3.9319(3)	6.5128(3)	108.89(3)°
Fractional coordinates					
	x	**y**	**z**	**B_{iso} (Å²)**	**Occupancy**
Ti_1	0.2996(11)	0.0	0.6906(15)	0.31(6)	1
Ti_2	0.4017(14)	0.0	0.3215(19)	0.31(6)	1
O_1	0.3418(7)	0.0	0.9983(15)	0.25(2)	1
O_2	0.2341(8)	0.0	0.3488(10)	0.25(2)	1
O_3	0.1272(6)	0.0	0.6774(11)	0.25(2)	1
O_4	0.4428(8)	0.0	0.6662(12)	0.25(2)	1
Li_1	0.935(2)	0.0	0.641(3)	0.4	0.75(5)
Li_2	0.185(2)	0.0	0.008(4)	0.4	0.85(5)

Table 4.5 Final parameter values for $Li_{0.8}TiO_2$(B) bulk refinement.

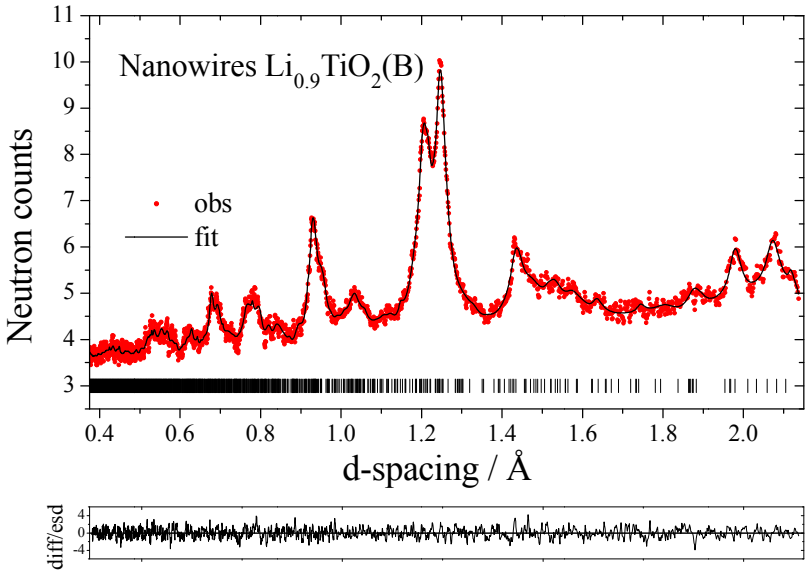

Figure 4.12 Refined powder neutron diffraction data $Li_{0.9}TiO_2$ (B) nanowires showing improved fit. Convergence achieved at Re = 2.29 %, Rwp = 2.76 %, Rp =2.27 %.

Phase	Space Group	a (Å)	b (Å)	c (Å)	β
$Li_{0.9}TiO_2$(B)	*C2/m,a*	12.513(7)	3.9361(8)	6.493(2)	108.12(4)°
Fractional coordinates					
	x	**y**	**z**	**B_{iso} (Å²)**	**Occupancy**
Ti_1	0.295(2)	0.0	0.668(5)	0.6(2)	1
Ti_2	0.414(2)	0.0	0.317(4)	0.6(2)	1
O_1	0.3449(12)	0.0	0.993(3)	0.33(6)	1
O_2	0.2252(17)	0.0	0.685(2)	0.33(6)	1
O_3	0.1269(14)	0.0	0.649(3)	0.33(6)	1
O_4	0.4399(16)	0.0	0.661(9)	0.33(6)	1
Li_1	0.964(4)	0.0	0.641(3)	0.4	0.75(5)
Li_2	0.162(5)	0.0	-0.007(11)	0.4	0.85(5)

Table 4.7 Final parameter values for $Li_{0.9}TiO_2$(B) nanowires refinement

TiO_2(B) bulk and nanowires were found to have a similar behaviour upon lithium insertion. From the investigation it can be concluded that the most favourable lithium insertion site at low concentrations ($x < 0.25$) is in the (010) channel at the square planar site named C-site, with a slightly off-centre position. Additional insertion of lithium ($0.25 < x < 0.5$) results in the depopulation of the C-site, which becomes unfavourable and occupation of the 5-coordinate A1-site. At higher lithium content, ($0.5 < x < 1$) both A1 and A2 sites are occupied.

An increase of the unit cell volume is observed with increase of the lithium content. Lithium insertion induces an isotropic variation of the cell parameters, including a pronounced expansion along the *b* axis[3].

4.4 Raman study of Li insertion mechanism for TiO_2(B) materials

4.4.1 *Ex situ* Raman study of Li insertion mechanism for bulk TiO_2(B)

An investigation via Raman microscopy of the mechanism of lithium insertion in the TiO_2(B) structure is reported here for the first time. In fact, apart from the Raman spectra of pristine TiO_2(B)[4], there is no literature describing lithium insertion in TiO_2(B) using Raman microscopy.

During the course of this work *ex situ* Raman microscopy was performed on TiO_2(B) samples with various lithium contents.

In figure 4.13 the evolution of the Raman spectra of bulk TiO_2(B) upon lithiation are reported. The various degrees of lithium content were achieved via chemical and electrochemical lithiation, respectively.

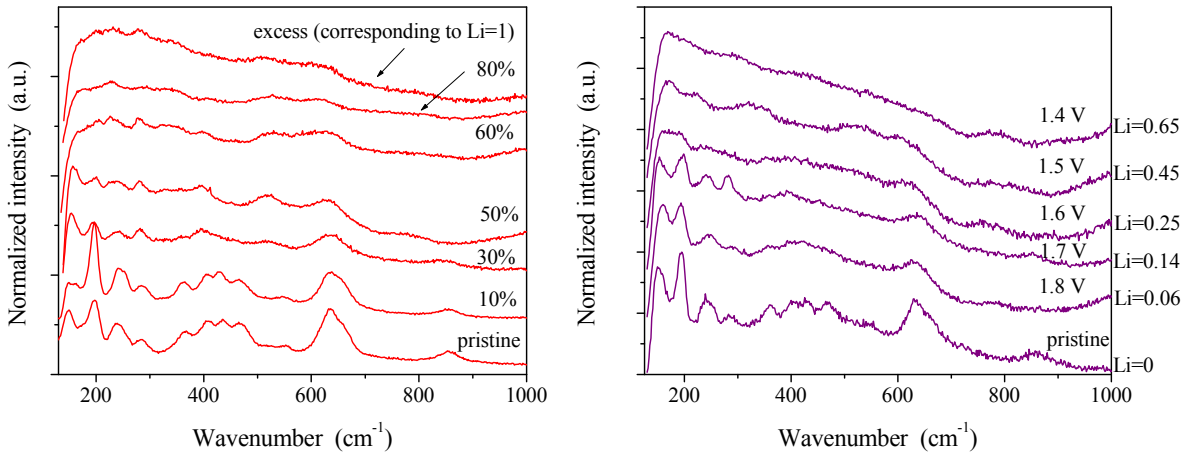

Figure 4.13 Raman spectra of bulk TiO_2(B) at various degrees of lithium content achieved via chemical (a) and electrochemical lithiation (b).

The spectra obtained from the two sets of measurements are in acceptable agreement with each other. In both cases at low lithium content, the typical TiO_2(B) features are

recognisable. As expected, a decrease of these features is observed upon lithiation. An exception to this observation can be seen for the peak around 281 cm^{-1} which increases with lithiation, until a certain composition is reached. For the electrochemically lithiated sample this composition is $Li_{0.25}TiO_2$, in agreement with what was observed in the powder neutron diffraction analysis, and for the sample obtained via chemical lithiation this composition corresponds to $Li_{0.6}TiO_2$. This disparity between the compositions is not unexpected as it is extremely difficult to accurately quantify the lithium content of samples that have been lithiated using two such drastically different methods.

Following additional lithium insertion, the signals are observed to become broad and weak, suggesting that the lithiated states of the materials may be less active in Raman microscopy. As can be seen, at high lithium concentration only four broad shoulders are recognisable from the Raman spectra, making recognition and interpretation of the spectra difficult.

4.4.1 *In situ* Raman investigation of Li insertion mechanism for TiO_2(B) nanotubes

Following the *ex situ* investigation of the bulk material, a study of the evolution of lithium insertion and removal in TiO_2(B) nanotubes was carried out using *in situ* Raman microscopy.

The Raman spectra of as-prepared TiO_2(B) nanotubes were collected using both *ex* and *in situ* measurements and are shown below in figure 4.14. As can be seen the two spectra of the pristine material are in good agreement.

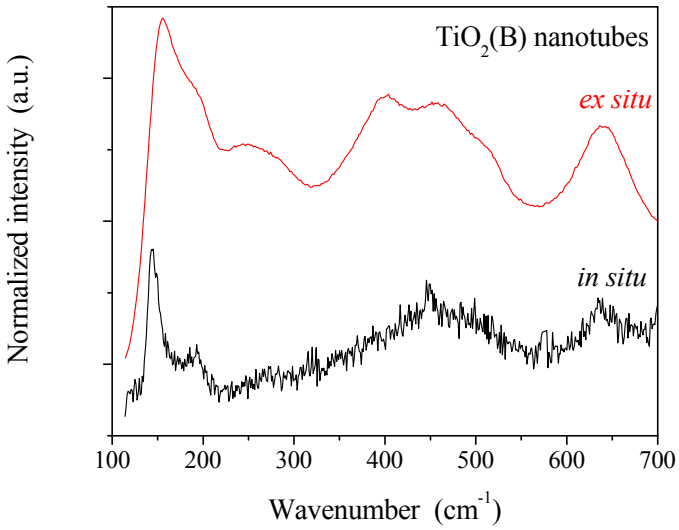

Figure 4.14 Raman spectra of as TiO_2(B) nanotubes collected *ex situ* (red) and *in situ* (black).

During the *in situ* measurement, Raman spectra were recorded during first discharge and following charge in galvanostatic conditions, with a current rate of 100 mA g^{-1} (C/3). The relative load curve is presented in figure 4.15.

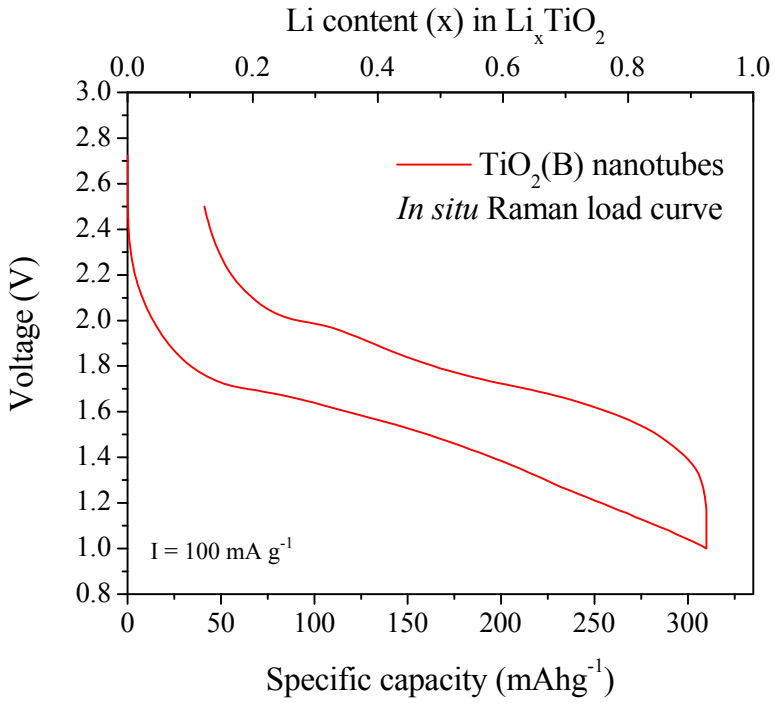

Figure 4.15 Discharge and charge curves recorded in galvanostatic conditions, with a current rate of 100 mA g^{-1}.

In figure 4.16, the Raman spectra collected during the experiment are reported.

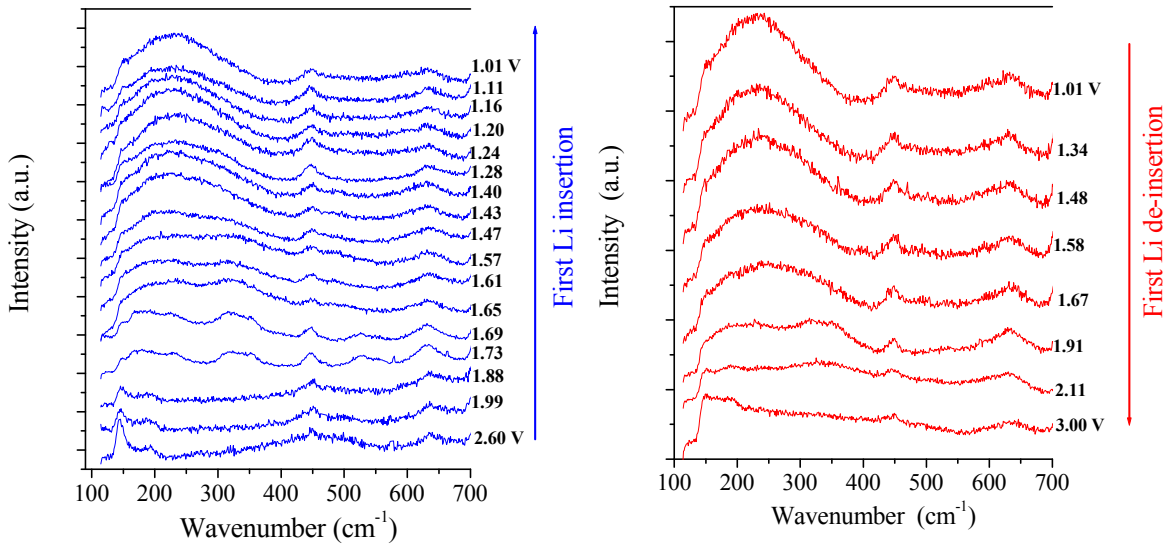

Figure 4.16 Raman spectra collected during discharge (in blue) and charge (in red).

As expected, during discharge, a decrease in the intensity of the typical TiO_2(B) features is observed. At a voltage value of 1.73 V the spectrum changes appearance, suggesting that the spectrum has lost the characteristics of the pristine material. This voltage value corresponds to a lithium content of 0.15 and is consistent with the beginning of the plateau in the load curve, where a two-phase transition occurs. The new features disappear at a voltage of 1.61 V, corresponding to a lithium content of 0.35, and the end of the plateau in the load curve. Further lithium insertion results in broadening of the signals, which has been already observed in the *ex situ* experiment carried out on the bulk material. Again four main shoulders are observed in the Raman spectra, however, the interpretation of these becomes difficult since the lithium rich phases of TiO_2(B) appear to be poorly active in Raman microscopy.

For the same reason, the early spectra collected during charge are characterised by broad peaks at 146, 238, 448 and 629 cm^{-1}. When a voltage value of 1.91 V is reached, at a composition of $Li_{0.38}TiO_2$, a change in the characteristics of the Raman spectra is observed. Further removal of lithium results in the reappearance of the features observed in the early stages of the discharge curve. This confirms the reversibility of the process; however, a complete reversible transformation is not observed, due to some lithium trapped in the structure which is the irreversible capacity mentioned above that is exhibited by the TiO_2(B) nanotubes.

4.5 Chapter conclusions

In this chapter the electrochemical performance of the TiO_2(B) bulk, nanowires and nanotubes has been investigated. All three materials exhibit a very similar voltage profiles, suggesting that the same redox processes occur. As expected, an increase in the capability of inserting lithium is observed with a decrease in the dimensions. The nanotubes show a superior discharge capacity at the first cycle, exceeding one equivalent of lithium insertion. This greater capacity is believed to be due to the larger surface area exhibited by the nanotubes, (205 m^2 g^{-1}), suggesting that an additional charge storage mechanism, occurring on the electrode surface, is present. However, with the nano-scaling of the materials, an increase in the polarisation in the load curves and the differential capacity plots is also observed.

The performance of the three materials was also tested using galvanostatic cycling, at a current rate of 100 mA g^{-1}. The TiO_2(B) nanotubes outperformed the other samples, and also showed superior capacity retention over a number of cycles. However, the nanotube electrode also seemed to be the most affected by irreversible capacity. It exhibited a significant loss in capacity at both low and high rates, 105.6 mAh g^{-1} and 71.1 mAh g^{-1} for 100 and 5 mA g^{-1}, respectively. These preliminary results suggest that the irreversible capacity is related to processes occurring at the surface of the electrode. The nanotubes, due to their larger surface area, are therefore the most affected.

Powder neutron diffraction was used to investigate the lithium insertion mechanism in TiO_2(B). This study was carried out on the bulk material and the nanowires. Both the materials were found to exhibit similar behaviour upon lithium insertion. It was found that the most favourable lithium insertion site at low concentrations ($x < 0.25$)

is in the (010) channel at the square planar site, named C-site, with a slightly off-centre position. At a lithium content ranging between 0.25 and 0.5, the C-site becomes unfavourable and lithium was found to occupy a 5-coordinate site, within the (001) plane, named A1-site. At higher lithium contents, ($0.5 < x < 1$) along with the A1-site a second 5-coordinate lithium site is occupied, the A2-site, which lies between the oxygen atoms bridging the adjacent layers in the (001) plane.

An attempt to investigate the lithium insertion and removal processes in the TiO_2(B) samples was carried out using Raman microscopy. In particular an *ex situ* study on both chemically and electrochemically lithiated bulk material was attempted. For the nanotubes an *in situ* Raman experiment was set up, and the Raman spectra were recorded during galvanostatic cycling at 100 mA g^{-1}. Unfortunately, beyond certain lithium content, the Raman spectra of the lithiated samples became too broad, making the interpretation of the spectra difficult. Despite the difficulty in interpreting the spectra of the lithiated stages, the *in situ* experiment carried out on the nanotubes, confirmed that a good level of reversibility was present in the lithium insertion and removal process. However, a complete reversible transformation was not observed, due to the lithium trapping phenomenon and the irreversible capacity which affects the TiO_2(B) nanotubes.

References

1. Brohan, L.; Marchand, R. *Solid State Ionics* (1983) **9-10** 419.

2. Coelho, A. A. *J. Appl. Crystallogr.* (2000) **33** 899.

3. Armstrong, A. R., Arrouvel, C.; Gentili,V.; Parker, S. C.; Saiful Islam M. and Bruce P.G. *Chem. Mater.* (2010) **22** 6426–6432.

4. Armstrong, A.R.; Armstrong, G.; Canales, J. and Bruce, P. G., *Chem. Commun.* (2005) 2454-2456.

Chapter 5

An investigation into the irreversible capacity of TiO_2(B) nanotubes

5.1 Introduction

Since the formation of a solid electrolyte interphase (SEI) layer at the lithium electrode was first reported by Peled in 1979[1], a large amount of research has been focussed on the interface between the electrode and the electrolyte. This film is formed on the surface of the active electrode materials during the electrochemical process or during the storage in the electrolyte[2]. If this passivating film is stable, it can suppress any further solvent decomposition at the electrode interphase and limit the breakdown of the electrode[3, 4]. However, the formation of the SEI layer also induces an irreversible capacity loss in the initial charge/discharge cycle[2].

One of the advantages offered by TiO_2 materials over the conventional graphite anodes is the fact that they work at higher potential (~1.5 V) within the electrolyte electrochemical stability window[5]. It is suggested that they should therefore not be affected by the formation of a solid electrolyte interphase layer. However, as noted in chapter 4, the TiO_2(B) samples showed an irreversible capacity loss in the first cycle. The bulk and the nanowire electrodes showed similar and moderate values of capacity loss. On the other hand, the TiO_2(B) nanotubes appeared to be significantly affected by this phenomenon. Both at high and low rates the nanotube electrodes

showed a remarkable loss in capacity: 106 mAh g^{-1} and 71 mAh g^{-1} for 100 and 5 mA g^{-1}, respectively. The higher surface area of the nanotubes suggests that the irreversible capacity loss may arise from surface reactions.

In this chapter the nature of the irreversible capacity for the TiO_2(B) nanotubes is investigated and possible solutions to this phenomenon are discussed.

5.2 Investigation of the effect of water contamination

As discussed in chapter 4, TiO_2(B) nanotubes exhibit a large surface area and it is also well-known that TiO_2 is hygroscopic. It is therefore not unexpected that the TiO_2(B) nanotubes can absorb moisture. The effect of water contamination on the electrochemical performance was investigated, to establish if there was any quantitative relationship with the irreversible capacity.

The following different treatments were investigated for the TiO_2(B) nanotubes:

1. post-annealing at 120 °C under vacuum for 2 h
2. post-annealing at 200 °C under vacuum for 2 h
3. annealing at 380 °C in dry air flow for 2 h

After the various treatments all samples were stored in a moisture free environment in an argon filled glove-box.

Thermogravimetric analysis was used to quantify the mass loss due to water for each sample, whilst simulating the post-annealing treatments (with the exception of the TGA being carried out under air-flow and not under vacuum). In figure 7.1 the thermogram is shown for hydrated titanate nanotubes. The measurement was run under air flow conditions, with a heating rate of 3 °C min^{-1}, with the addition of an

isothermal step at 400 °C of 2 h, in order to simulate the annealing process. Following this, the temperature was then raised to 800 °C.

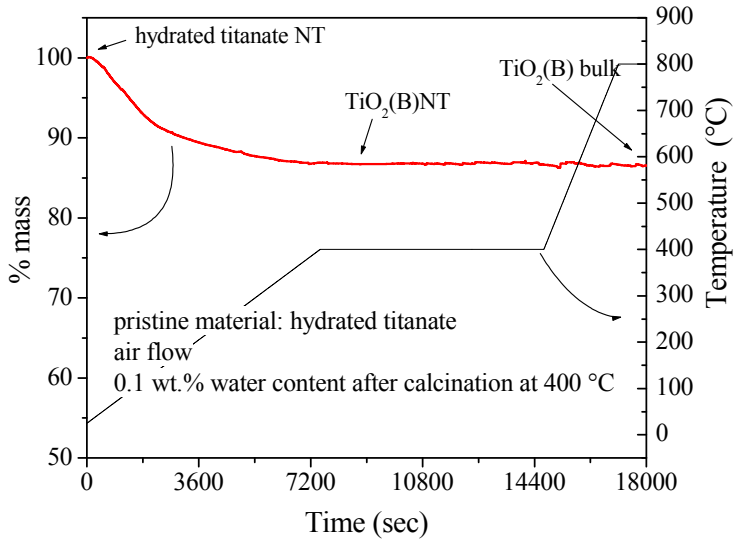

Figure 5.1 Thermogram of hydrated titanate nanotubes performed under flowing air up to 800 °C with an isothermal step at 400 °C of 2h.

The residual water in the structure was estimated to be 0.1 % after calcination at 400 °C. A further increase in the temperature led to the collapse of the tubular structure and sintering of the materials. After the treatment at 800 °C the product obtained was bulk TiO_2(B).

In figures 5.2 and 5.3 the thermograms are reported for the TiO_2(B) nanotubes carried out under air flow. The experiments were run in one case with an isotherm at 120 °C for 2 h and in the other with the isotherm at 200 °C for 2 h, to simulate similar conditions to the two post-annealing treatments. Subsequently the temperature was raised to 800 °C.

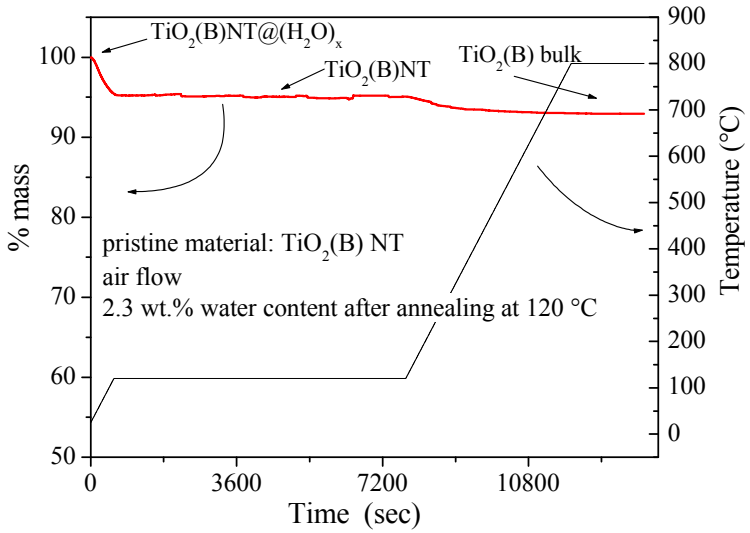

Figure 5.2 Thermogram of TiO_2(B) nanotubes performed under flowing air up to 800 °C with an isothermal step at 120 °C of 2 h.

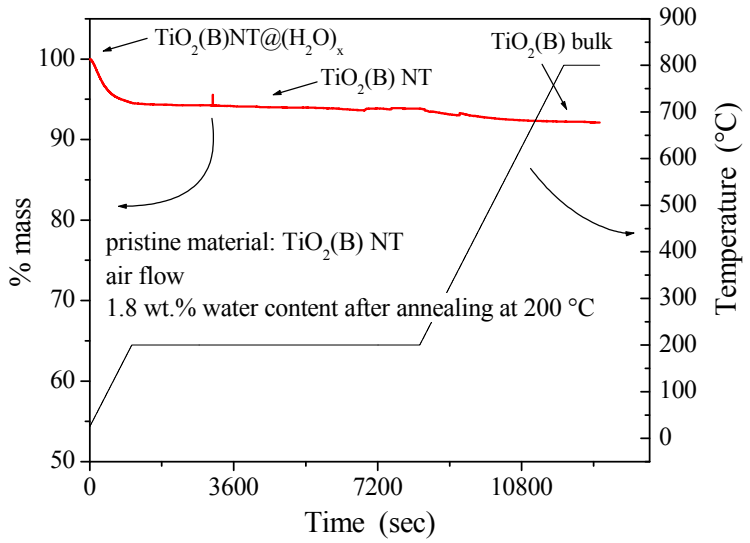

Figure 5.3 Thermogram of TiO_2(B) nanotubes performed under flowing air up to 800 °C with an isothermal step at 200 °C of 2 h.

The sample subjected to the post-annealing treatment at 120 °C, shows a residual content of 2.3 % by weight. For the TiO_2(B) nanotubes treated at 200 °C the water content after the post-annealing treatment was estimated to be 1.8 % by weight. In

both cases the content of residual water after the post-annealing treatment can be considered minor.

FTIR measurements were also run on the samples which underwent the different treatments. The spectra are reported in figure 5.4.

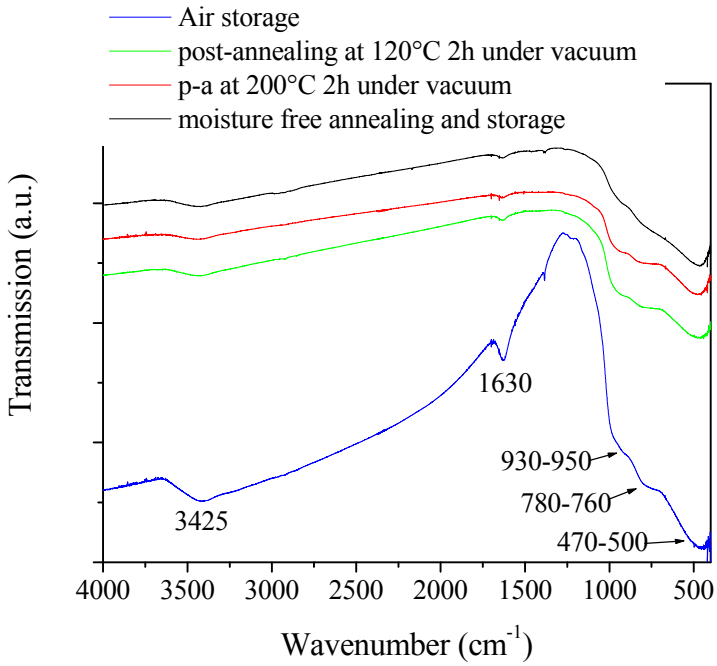

Figure 5.4 FTIR spectra of TiO_2(B) nanotubes that have undergone different thermal procedures.

The IR spectrum of the standard TiO_2(B) nanotubes (in blue) shows the ν(O-H) stretching bands in the region between 3740 and 3300 cm^{-1} and the band at 1630 cm^{-1} associated with the δ(H-O-H) bending. The large bands observed in the ranges: 470-500; 760-780 and 930-950 cm^{-1} are associated with TiO_2[6]. In this spectrum the presence of water absorbed by the nanotubes is clearly evident.

As can be observed from figure 5.4, both the specimens that underwent the post-annealing treatments and the sample calcined in dry air conditions show a dramatic reduction in water content compared with the standard annealing treatment.

However, the bands associated with the presence of residual OH groups are still observable. The presence of residual OH groups on the surface of TiO_2 when calcined at 400 °C has already been reported in the literature[7].

Having established from the FTIR spectra that the standard TiO_2(B) nanotubes have significant water content compared with the sample annealed under dry air, the electrochemical performance of both samples was then investigated. This was to establish the effect of water contamination on the electrochemical performance of the materials and to establish if it was responsible for the irreversible capacity at the initial cycle. The performance of the two samples is shown in figure 5.5, where the specific capacity over a large number of cycles is reported for galvanostatic cycling at a current rate of 100 mA g^{-1} (C/3).

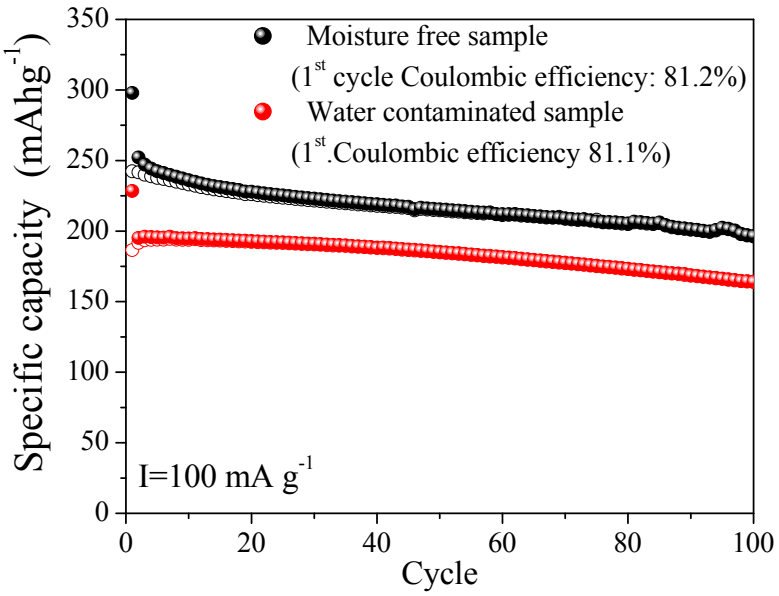

Figure 5.5 Specific capacities in charge (hollow) and discharge (filled) over 100 cycles for the moisture contaminated (in red) and the moisture free (in black) TiO_2(B) nanotubes.

As can be seen, the nanotubes treated in moisture free conditions exhibit better performance in terms of capacity cycled compared with the nanotubes treated in air.

However, both electrodes show similar coulombic efficiency at the first cycle of around 81 %. This result suggests that the water absorbed by the nanotubes is not the direct cause of the irreversible capacity.

The coulombic efficiencies of both materials at the first cycle for different current rates are reported in figure 5.6.

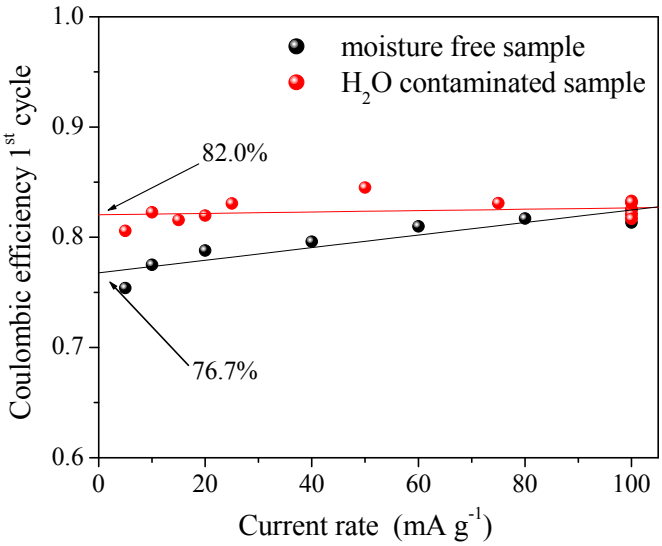

Figure 5.6 The coulombic efficiencies of moisture contaminated (in red) and the moisture free (in black) TiO_2(B) nanotubes at the first cycle for different current rates.

As can be seen, different trends are observable for the H_2O contaminated and the moisture free samples. In fact, while the moisture contaminated nanotubes exhibit a constant coulombic efficiency for the various current rates, with a value of about 82 %, the moisture free sample displays a lower coulombic efficiency (76 %) at low current rates and is therefore more affected by the irreversible capacity loss.

These preliminary results suggest that the water absorbed on the surface of the nanotube electrode interacts with the electrolyte, thus reducing the amount of

reversible cycled capacity: this process does not depend on the current rate at which the battery is discharged.

5.3 Investigation into the nature of the irreversible capacity

In order to understand the nature of the irreversible capacity, it was necessary to inspect the processes occurring during the lithium insertion and the removal in the initial and subsequent cycles. This type of information is obtained from PGCA measurements, which are presented in figure 5.7a for the moisture contaminated nanotubes and figure 5.7b for the moisture free sample. The measurements were carried out in the voltage range between 1-2.5 V, with a current cut off of 5 mA/g and step of 10 mV. In the PGCA curves the differential capacity is plotted as a function of the voltage over several cycles.

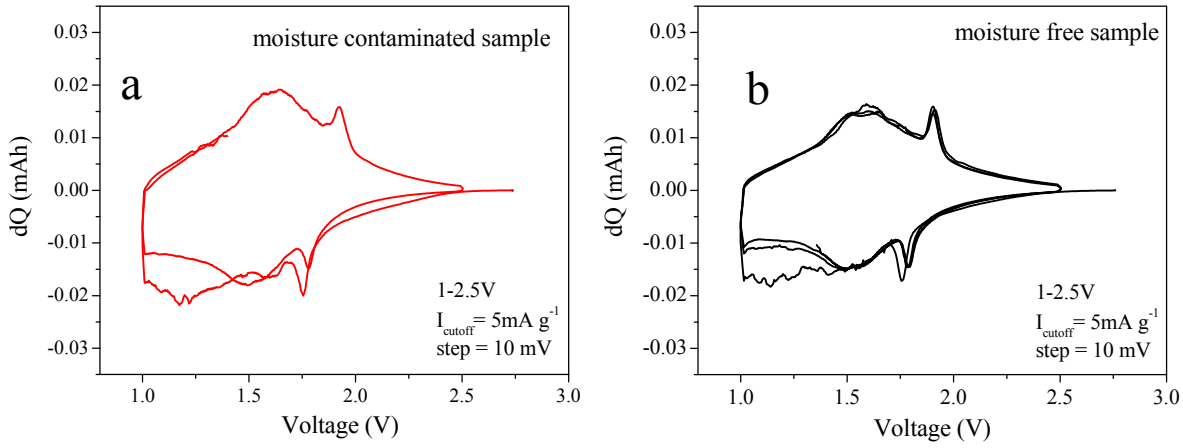

Figure 5.7 PCGA curves of moisture contaminated (a) and the moisture free (b) TiO_2(B) nanotubes, collected n a voltage range between 1-2.5 V, with a current cut-off of 5 mA g^{-1} and step of 10 mV.

The PGCA curves for the moisture contaminated and the moisture free nanotubes look very similar. In both cases the first discharge, corresponding to the first lithium insertion, appears to be different from subsequent cycles. Two processes in two different regions are observable. The first process occurs in the high voltage region (V>1.5 V), which is particularly evident in the moisture contaminated sample. The second, more noticeable, process occurs in the low voltage region (V<1.5 V) and is very similar for both samples. Both these processes are absent in subsequent cycles, which also exhibit good reversibility. This suggests that the origin of the irreversible capacity has to be looked for in the processes occurring in these two voltage regions.

The performance, in terms of coulombic efficiency, for both samples was investigated at various voltage cut-offs during galvanostatic cycling. The measurements were carried out at a current rate of 100 mA g^{-1} (C/3). The relative plots are reported in figure 5.8.

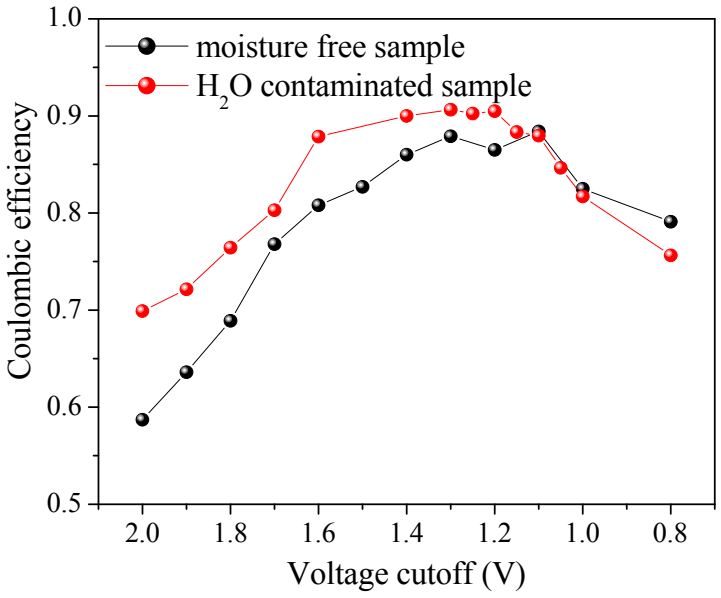

Figure 5.8 Coulombic efficiencies for the moisture contaminated (in red) and the moisture free (in black) TiO_2(B) nanotubes at various voltage cut-offs during galvanostatic cycling at 100 mA g^{-1}.

As can be observed from the plot, it appears that the moisture contaminated sample performs better in the high voltage regions compared with the moisture free sample.

To investigate this phenomenon in more detail, the voltage cut-off measurements were repeated on the moisture free sample with the addition of a potentiostatic step at the end of the charge, which maintains the cell on hold for 10 h at 2.5 V. The relevant plot is reported in figure 5.9 together with the plot relative to the procedure without the potentiostatic step at 2.5 V.

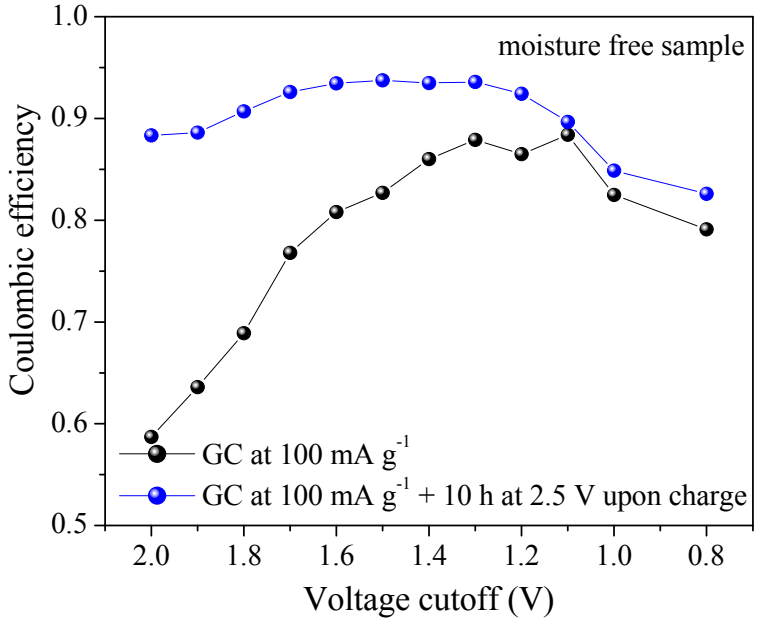

Figure 5.9 Coulombic efficiencies for moisture free TiO_2(B) nanotubes at various voltage cut-offs during galvanostatic cycling at 100 mA/g with (in blue) and without (in black) potentiostatic step.

As can be seen, the two trends observed for the coulombic efficiency in the high voltage region are totally different. This suggests that the poor performance at high voltage cut-off (V>1.5 V) is due to kinetically limited reversible processes, such as lithium trapping or the re-oxidation of possible electrolyte decomposition products. Thus, the performance can be enhanced by adding a potentiostatic step at 2.5 V to

allow these kinetically limited processes to complete. The decoupling of these effects will be addressed in the following paragraph.

On the other hand, the trend observed in the low voltage region appears to be very similar for both samples.

Measurements were also taken on the moisture free TiO_2(B) nanotubes at different charge/discharge rates and the relative trends are reported in figure 5.10.

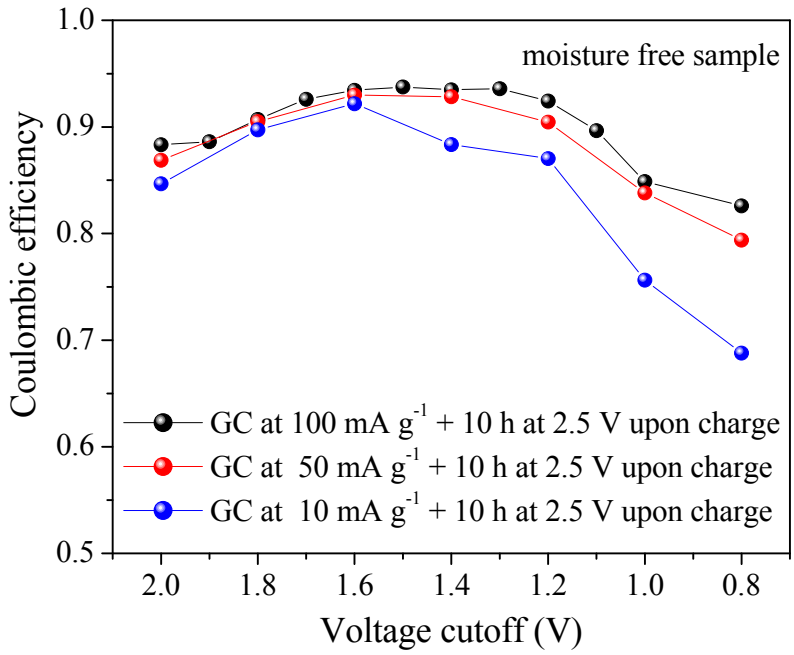

Figure 5.10 Coulombic efficiencies for moisture free TiO_2(B) nanotubes at various voltage cut-offs during galvanostatic at different current rates.

As can be seen the trends are very similar. At high voltage cut-offs the trend is unaltered for all rates. However, for low voltage cut-offs, the low rates worsen the columbic efficiency, which decreases dramatically, in particular for voltage values below 1.2 V.

These observations suggest that the main irreversible electro-active processes may be occurring on the electrode surface at low voltages (V < 1.2 V). A possible cause could be the presence, though minimal, of the residual OH groups on the surface, as observed in the IR analysis.

To investigate the formation and the stability of a passivating film at the interface with the electrolyte during the initial cycle, AC impedance spectroscopy was performed on the TiO_2(B) nanotube electrode during the first cycle.

The relative Nyquist plots for the first discharge and first charge are reported in figures 5.11a and 5.12a respectively, together with the relative values of resistance and capacitance reported as a function of the lithium uptake (fig. 5.11b and 5.12b).

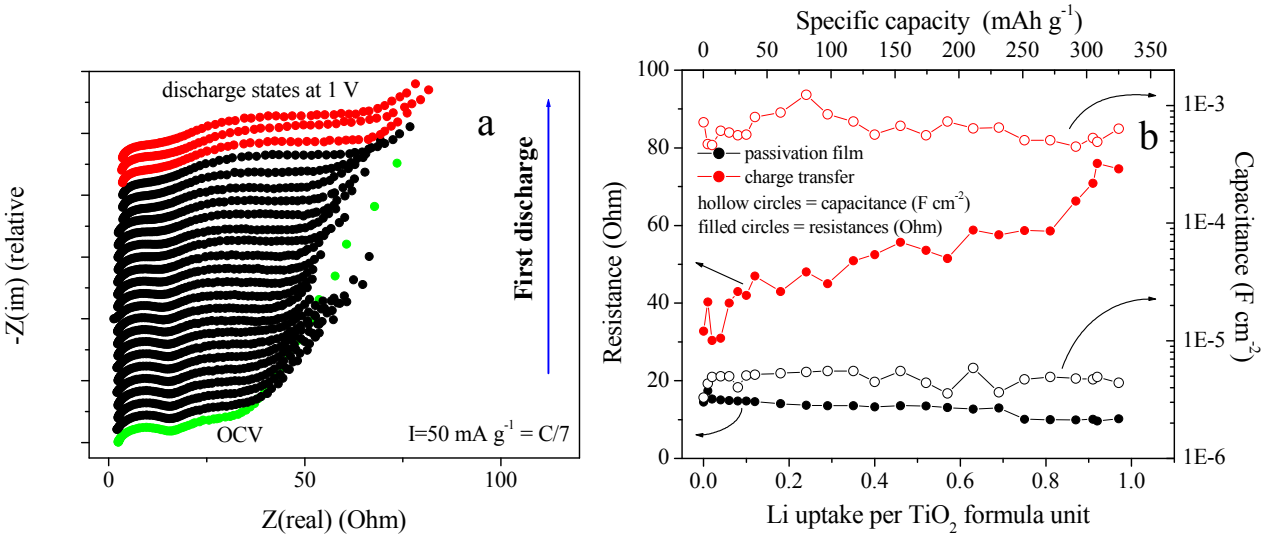

Figure 5.11 Nyquist plots recorded during discharge for the moisture free TiO_2(B) nanotubes (a) and relative resistances and capacitance values associated with the passivating film and the charge transfer *vs* lithium uptake (b).

In the Nyquist plots two semicircles are recognisable. The first semicircle at high frequency can be associated with the formation and the evolution of the

electrode/electrolyte double layer and, therefore, it is evidence of the formation of a solid electrolyte interphase (SEI). The second semicircle at lower frequency is associated with the charge transfer and is followed by the final diffusion observed at low frequencies.

During discharge the resistance offered by the passivating layer does not show dramatic changes. The passivating film is maintained constantly throughout the lithium insertion and only a slight decrease in the resistance is observed at low voltages. On the other hand, as expected, the amplitude of the semicircle associated with the charge transfer and, therefore, the resistance increases during discharge.

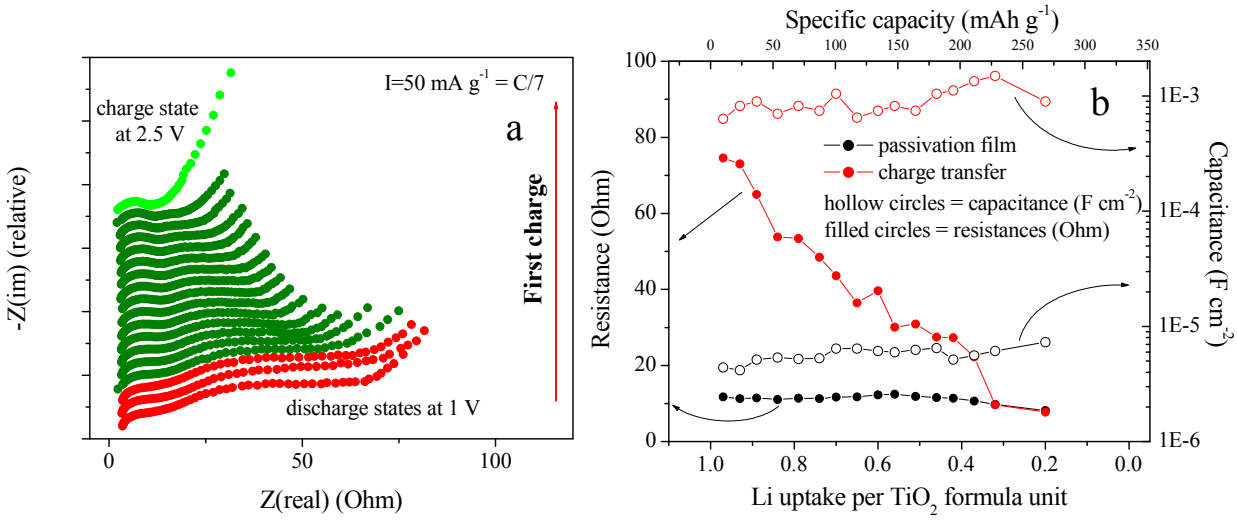

Figure 5.12 Nyquist plots recorded during charge for the moisture free TiO_2(B) nanotubes (a) and relative resistances and capacitances values associated with the passivating film and the charge transfer *vs* lithium uptake (b).

This is evident from the graph reported in figure 6.12a where the resistance and the capacitance associated with the two processes are reported as functions of lithium uptake.

Similar behaviour is observed during the first charge reported in figure 5.12a. The semicircle associated with the double layer undergoes very little change. The major variation observed for the semicircle is associated with the charge transfer process, which, as expected, decreases drastically at the end of the charge. This is summarised in figure 5.12b.

The AC impedance spectroscopy results suggest a certain stability for the passivating layer formed at the interface between the TiO_2(B) nanotube electrode and the electrolyte.

In order to establish the nature of the passivating film, FTIR analysis was performed on the electrodes at different states of charge. The spectra are reported in figure 5.13. Prior to the measurements, the samples were washed in dimethyl carbonate (DMC) and tetrahydrofuran (THF) in order to remove the electrolyte and the glass fibres of the separator.

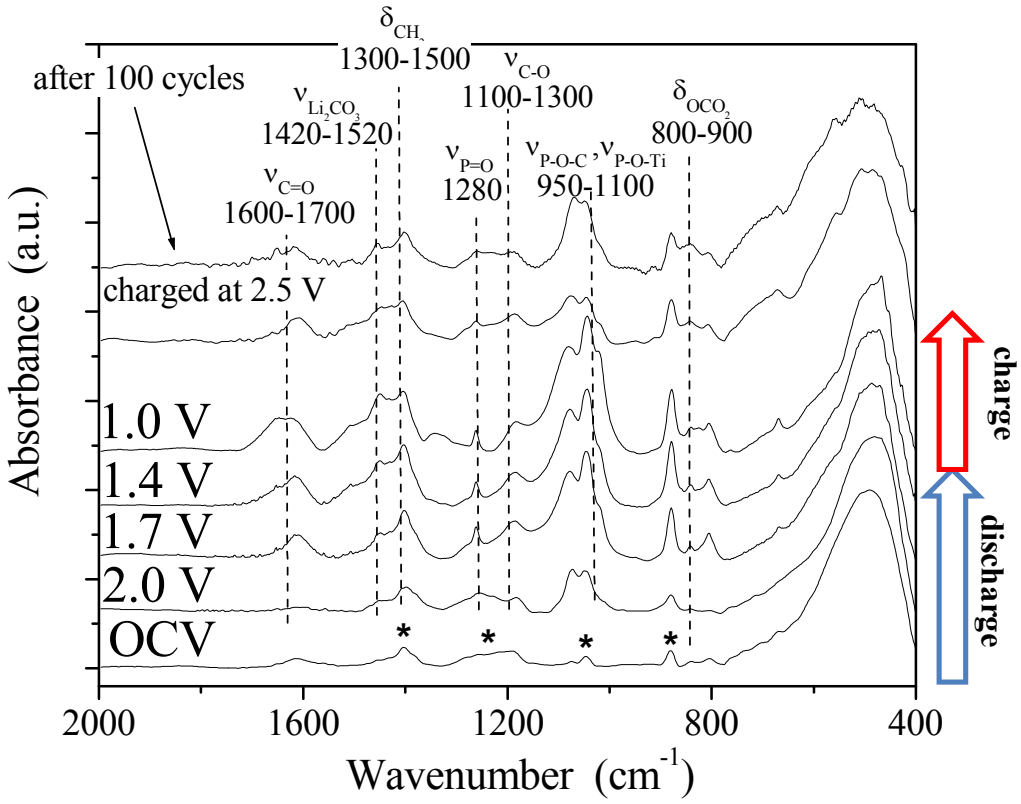

Figure 5.13 FTIR spectra of the moisture free TiO_2(B) nanotube electrodes collected at different states of charge. (* binder, PVdF).

The appearance of certain bands, associated with different species, has been noted during discharge and this is believed to be indicative of the formation of the passivating film on the electrode surface. There are two bands associated with phosphorus-based species, the first of which is observable between 950-1100 cm^{-1} and corresponds to the ν(POC) and the ν(POTi) stretching[8]. The second sharp band is seen at 1280 cm^{-1} and is associated with the ν(P=O) stretching. There are several carbon-based species which are also noted to increase during discharge. The most significant of these was found to be the broad lithium carbonate stretching ν(Li_2CO_3) between 1420-1520 cm^{-1}, the carbonyl group stretching ν(C=O) between 1600-1700 cm^{-1} and the carbonate bond bending δ (OCO_2) between 800-900 cm^{-1} [8].

These bands are not present in the pristine electrode and appear at the beginning of the discharge and become more significant over discharge. If the reactions forming these species were fully reversible then these bands would disappear during the charge. As can be seen, however, while the bands associated with the phosphate species reduce after the charge, the features associated with the carbonate species remain during charge and even after the electrode has been cycled 100 times, the bands are still present.

These observations suggest that the species being produced: phosphates and the carbonates, Li_2CO_3 and RCO_3Li, comprise the passivating film formed during the initial discharge and that, once the film has formed, it is stable and still present even after 100 cycles.

This result also provides the first evidence that this film could potentially be responsible for the TiO_2(B) nanotubes irreversible capacity.

Following the results obtained from the FTIR spectroscopy, X-ray photoelectron spectroscopy (XPS) experiments were then carried out on the electrodes at different states of charge.

There were five samples investigated: the pristine electrode at the OCV; the sample discharged down to 1.7 V; the sample discharged at 1 V; the sample subjected to the first discharge and then fully charged up to 2.5 V and finally the electrode fully charged and subsequently subjected to a potentiostatic hold at 2.5 V for 6 h. Prior to the measurements the samples were washed in dimethyl carbonate (DMC) and tetrahydrofuran (THF) in order to remove the electrolyte and the glass fibres of the separator.

The survey spectrum was collected for all samples, however only the regions of interest are reported. These are the Ti 2p, O 1s, P 2p and F 1s regions.

The spectra of the regions of the four elements reported are shown below in figure 5.14. The results concerning each individual element will be discussed separately.

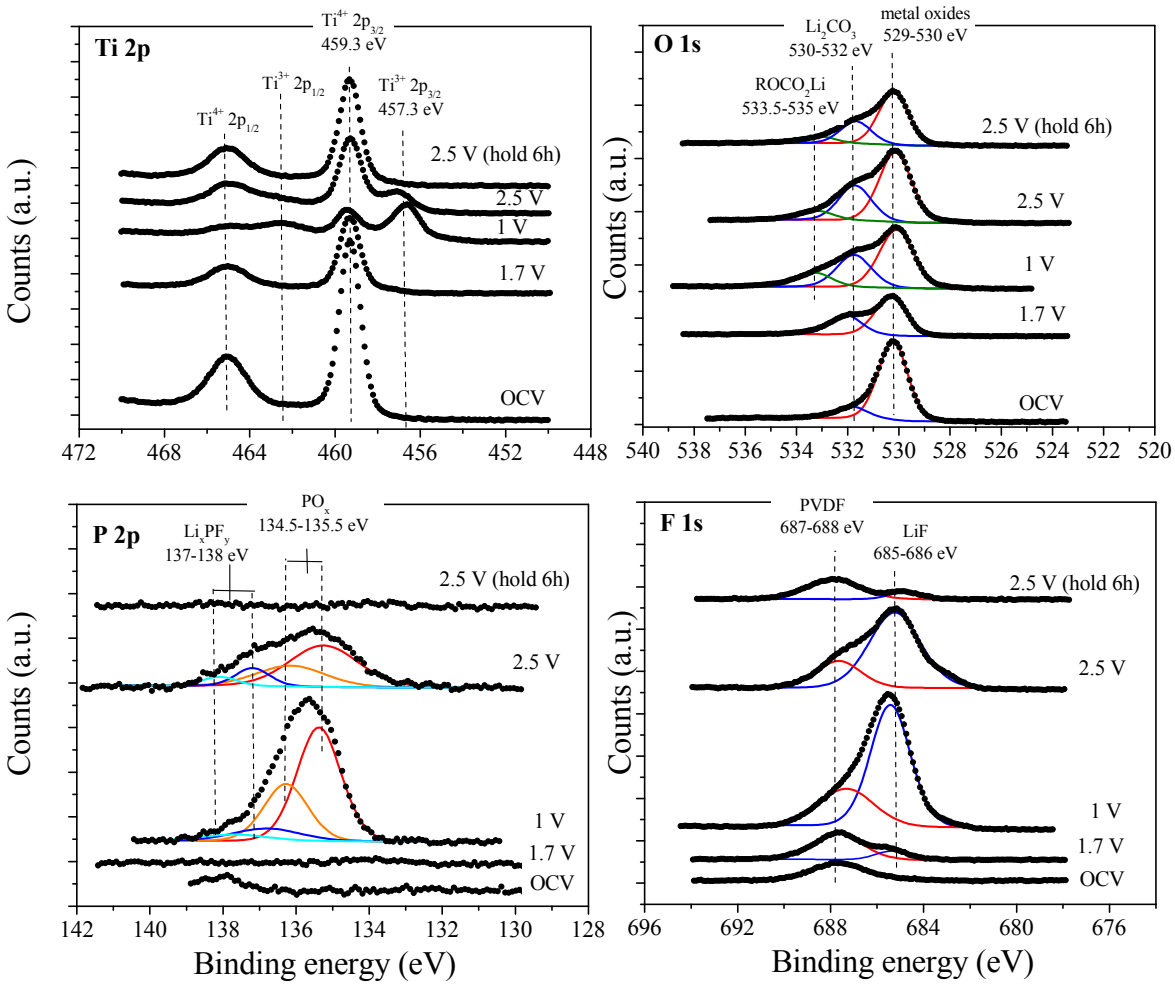

Figure 5.14 XPS spectra of Ti 2p, O 1s, P 2p and F 1s regions for moisture free TiO_2(B) nanotubes electrodes collected at different states of charge.

The Ti 2p region of the OCV sample shows two peaks at 459.3 eV and 465 eV which can be attributed to the Ti^{4+} $2p_{3/2}$ and Ti^{4+} $2p_{1/2}$ respectively[9]. In the sample discharged to 1.7 V the appearance of a shoulder is observable at lower binding energies suggesting the onset of the Ti^{3+} species which is expected due to the reduction of the Ti^{4+} to Ti^{3+} upon lithium insertion. In the sample discharged at 1 V the Ti^{3+} $2p_{3/2}$ is clearly visible at 457.3 eV. As expected, the Ti^{3+} species is dominant compared with the Ti^{4+}. When the electrode is charged up to 2.5 V the Ti^{3+} should be oxidised back to Ti^{4+}, however, in the spectra of the fully charged sample the peaks associated with the $Ti^{3+}$are still present. This confirms that a certain amount of lithium is still trapped in the structure. Only in the sample fully charged and kept at 2.5 V for 6 h is there evidence of the disappearance of the peaks associated with the Ti^{3+}. This was already observed in the galvanostatic cycling at various voltage cut-offs with and without the voltage hold. This suggests that the irreversible capacity loss exhibited by the sample without the voltage hold upon charge is mainly due to the phenomenon of kinetic lithium trapping occurring. This phenomenon can be overcome by adding the potentiostatic step upon charge. The long step at high voltage allows the complete removal of lithium.

In the O 1s an evolution of its peak is observed upon lithium insertion. In the sample at the OCV the peak associated with the metal oxide is observed at 530 eV. Upon lithium insertion the growth of a second peak is observed at 532 eV followed by a third peak at 533.5 eV. These peaks are associated with the oxygen present in the carbonate group of Li_2CO_3 and RCO_3Li, respectively[10]. These peaks are present in all the subsequent spectra, confirming the presence of the species already noted in the FTIR analysis.

In the P 2p region, the peak at 134 eV associated with the phosphate is visible for the sample at 1.7 V, and in the sample at 1V is accompanied by a second peak at 135 eV associated with the species Li_xPF_y which is a product of the decomposition of the electrolyte[10]. However, in the spectrum of sample kept at 2.5 V for 6 h these peaks are no longer visible confirming what was also observed in the FTIR experiments.

In the region of F 1s the peak at 687 eV associated with the C-F of the binder (PVdF) is present for all samples[11]. In addition the growth of a second peak at 685 eV is observed upon lithiation. This peak is associated with the LiF species and is still present for the sample fully charged[10]. However the peak is significantly reduced in the sample subjected to the potentiostatic step at 2.5 V.

Evidence of the formation of the passivating film on the electrode surface was also found using transmission electron microscopy.

In figure 5.15 the images are reported for the TiO_2(B) nanotube electrode at the OCV (a), the sample discharged at 1.4 V (b), the fully discharged sample at 1V (c) and finally the sample fully charged (d).

As can be seen, the nanotubes are clearly observable as pristine materials in the OCV image. However, even at an intermediate stage of discharge an amorphous layer can be seen present on the tubes, which becomes more evident on the sample fully discharged at 1 V as a thicker layer and is still present in the sample that has been fully charged.

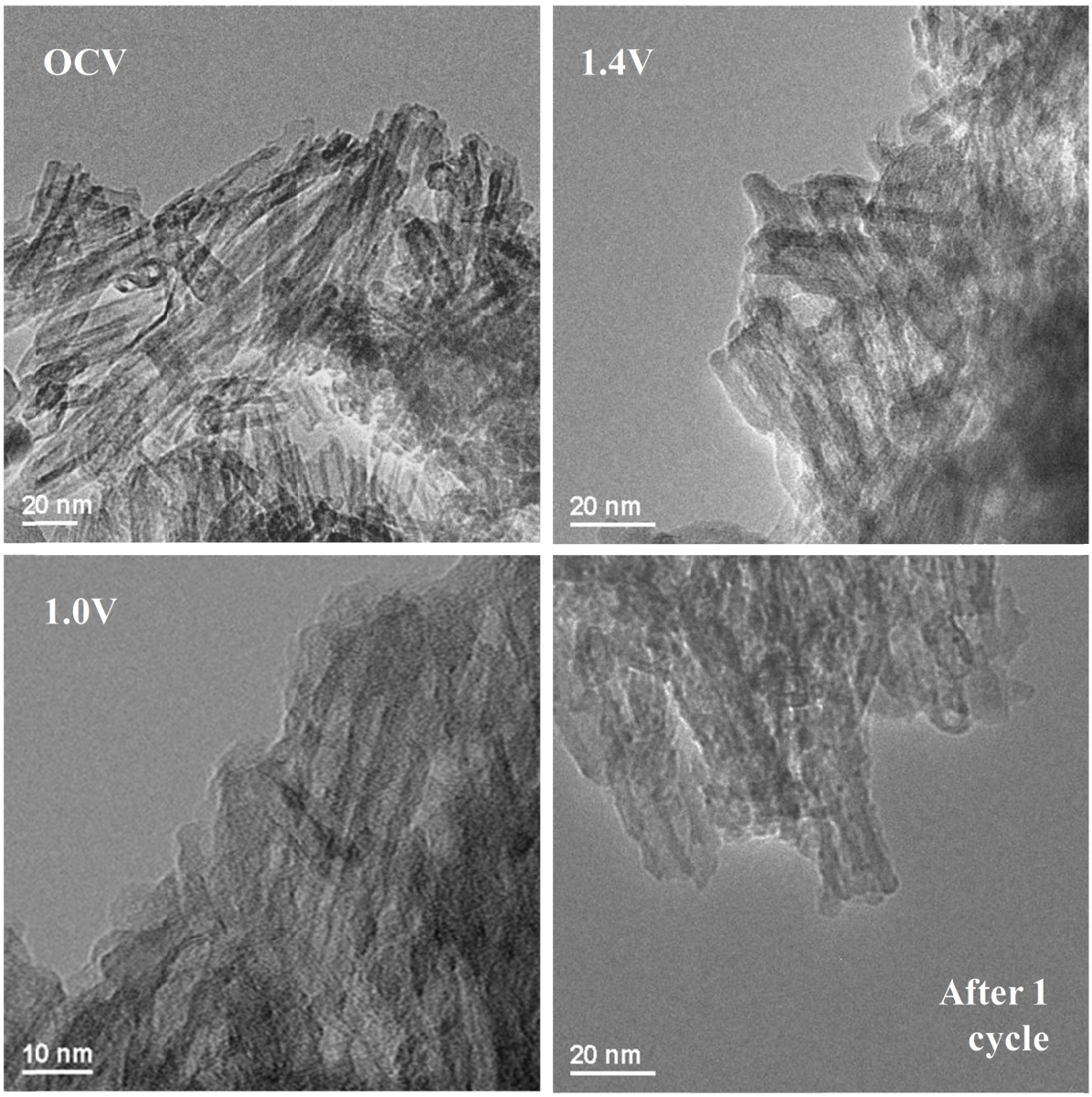

Figure 5.15 TEM images of composite electrodes of TiO_2(B) nanotubes at different states of charge.

From the investigation into the nature of the irreversible capacity it can be concluded that the irreversible capacity loss is due to two distinct phenomena, which occur in two different voltage regions. The first is the kinetic lithium trapping. It has been proven that this phenomenon can be overcome by applying the potentiostatic step at the end of the lithium removal.

The second cause of the irreversible capacity is to be found in the side-reactions occurring between the lithium salt ($LiPF_6$) and the electrodes active species which induce the formation of a passivating layer.

Both FTIR and XPS experiments have provided evidence of the formation of the surface electrolyte interphase between the TiO_2(B) nanotubes electrode and the electrolyte. Inorganic and organic carbonate species are formed upon cycling together with the formation and subsequent decomposition of surface phosphates.

5.4 Technological implementation

In order to minimise the irreversible capacity loss exhibited by the TiO_2(B) nanotubes, different strategies have been proposed and investigated.

The chosen strategies have the common aim of inhibiting or compensating for the side-reactions occurring between the lithium salt, $LiPF_6$, and the electrode active species which induce the formation of a passivating layer, in particular, the crystal OH groups present on the electrode surface.

The first strategy investigated was the introduction of nano-lithium powder (LECTRO) in the composite electrode. The amount of lithium introduced was 20 % in moles versus the titanium. Therefore, the final composition of the electrode was

73.7 % titanium dioxide annealed in dry conditions; 1.3 % nano-lithium; 15 % conductive carbon (super P) and 10 % binder (PVdF).

The second procedure investigated to reduce the irreversible capacity of the TiO_2(B) nanotubes was the treatment of the titanium dioxide powders, annealed and stored in moisture free conditions, with a solution of n-butyllithium 10% in moles versus titanium. The butyllithium reacts with the OH groups on the active material surface forming Li_2O and lithiates the first TiO_2 layers, and inhibiting any further reactivity on the surface. Any residual organic products are removed by washing with hexane and the powder is then dried under dynamic vacuum. The composite electrode was then prepared following the usual composition of 75 % of active material, pre-treated with butyllithium, 15 % of the conductive carbon and 10 % of binder.

The final procedure was the pre-treatment of the moisture free TiO_2(B) nanotubes with 100 % in moles of lithium ethoxide. In this case, the lithium ethoxide reacts with the OH groups on the surface in accordance with the following reaction:

$$Ti\text{-}OH + C_2H_5OLi \rightarrow Ti\text{-}O\text{-}Li + C_2H_5OH$$

Ethanol is then easily removed by washing with hexane and evaporated under dynamic vacuum. Once again, the composite electrode was then assembled using the standard composition of 75 % of pre-treated active material, 15 % of the conductive carbon and 10 % of binder.

In figure 5.16 the performance of the treated materials is reported together with those of the moisture contaminated and the moisture free TiO_2(B) nanotubes under galvanostatic cycling, at a current rate of 100 mA g^{-1} (C/3), with the addition of a potentiostatic step of 10 h upon charge.

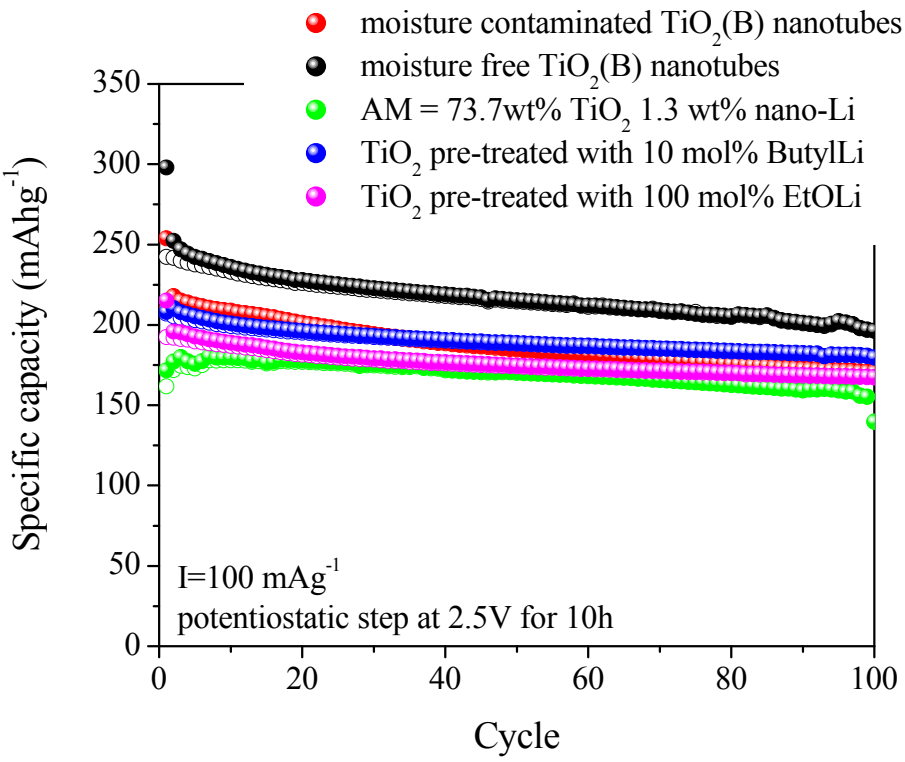

Figure 5.16 Specific capacities in charge (hollow) and discharge (filled) over 100 cycles for the TiO_2(B) nanotubes for the different treatments.

As can be seen, the introduction of the nano-lithium in the composite electrode and both pre-treatments procedures cause a decrease of the first discharge capacity. This is due the reduction of Ti^{4+} to Ti^{3+} in the electrode in the first surface layers induced by the intercalation of lithium. This is particularly evident for the composite electrode with nano-lithium powder.

However, in all treated samples, the irreversible capacity loss is dramatically reduced and they all exhibit good capacity retention over cycling.

In table 5.1 the coulombic efficiency for the first cycle for each of the different samples is reported. A remarkable improvement in the coulombic efficiency is observed for the pre-treated TiO_2(B) nanotubes and the composite electrode with addition of nano-lithium.

Coulombic efficiency at 1st cycle	
Moisture contaminated TiO_2(B) NT	82%
Moisture free TiO_2(B) NT	81%
TiO_2(B) NT + nano-Li	96%
TiO_2(B) NT pre-treated with ButylLi	97%
TiO_2(B) NT pre-treated with EtOLi	92%

Table. 5.1 Coulombic efficiency at the first cycle for the different TiO_2(B) nanotube electrodes.

5.5 Chapter conclusions

In this chapter the nature of the irreversible capacity for the TiO_2(B) nanotubes was investigated and discussed.

In particular, the effect of water contamination on the electrochemical performance was investigated, to establish if there was any relationship with the irreversible capacity.

Several annealing treatments were tested. Despite an enhancement in the capacity over a large number of cycles exhibited by the nanotubes treated in dry air and stored in argon, no improvement in the reduction of the irreversible capacity was achieved.

FTIR analysis suggested the presence of residual OH groups on the surface of TiO_2, even for the samples treated and stored in a moisture free environment.

Following this, the nature of the irreversible capacity was investigated. In particular, the performance in terms of coulombic efficiency for the TiO_2(B) nanotubes was tested at various voltage cut-offs during galvanostatic cycling, to establish the voltage windows at which the irreversible processes occurred. This analysis identified two phenomena occurring in two different voltage regions: high voltages ($V>1.5$ V) and low voltages ($V<1.2$ V). The poor performance at high voltage cut-off ($V>1.5$ V) was proven to be due mainly to a reversible kinetic lithium trapping. The phenomenon could be overcome and the performance enhanced by adding a potentiostatic step upon charge at 2.5 V to allow the complete removal of the lithium from the TiO_2 structure. The low coulombic efficiency exhibited at low voltages possibly originates in further side-reactions occurring on the electrode surfaces. This may be due to the presence of the residual OH groups on the surface of the electrode.

Following these results the formation and evolution of the SEI layer was investigated using AC impedance spectroscopy and the nature of the passivating film was studied using FTIR spectroscopy and X-ray photoelectron spectroscopy. Both techniques provided evidence of the formation of a surface electrolyte interphase, comprising of inorganic and organic carbonate species formed upon cycling and surface phosphates which are formed and decomposed upon cycling. The formation of the passivating layer was also proven by TEM imaging.

In order to minimise the irreversible capacity loss exhibited by the TiO_2(B) nanotubes, three different strategies were proposed and investigated.

The purpose was to inhibit or compensate for the side-reactions occurring between the lithium salt, $LiPF_6$, and the electrode active species which induce the formation of the passivating layer.

The three procedures consisted of:

1. The addition of nano-lithium to the composite electrode;
2. Pre-treatment the TiO_2(B) nanotubes with n-butyllithium (10 mol% versus titanium);
3. Pre-treatment the TiO_2(B) nanotubes with lithium ethoxide (100 mol% versus titanium).

All three strategies resulted in the reduction of the first discharge capacity due to lithium pre-loading. However, in all cases the irreversible capacity loss was dramatically reduced, and all samples exhibited a coulombic efficiency of over 90 %.

References

1. Peled, E. *J. Electrochem. Soc.* (1979) **126** 2047.
2. Shu, J. *Electrochemical and Solid-State Letters* (2008) **11** 12 A238-A240.
3. Shu, J.; Li, H.; Yang, R. Z.; Shi, Y. and Huang, X. J. *Electrochem. Commun.* (2006) **8** 51.
4. Wu, X.D.; Wang, Z.X; Chen, L. Q. and Huang, X. J. *Electrochem. Commun.* (2003) **5** 935.
5. Moshkovich, M.; Gofer, Y.; Aurbach, D. *J. Electrochem. Soc.* (2001) **148** E155−E167.
6. Soria, J.; Sanz, J.; Sobrados, I.; Coronado, J.M.; Maira, A.J.; Hernandez-Alonso, M.D.; Fresno, F. *J. Phys. Chem. C* (2007) **111** 10590-10596.
7. Morterra, C.*J. Chem.Soc., Farady Trans. 1* (1988) **84** 1617-1637.
8. Pouchert, C.J. *The Aldrich Library of Infrared Sectroscopy* Aldrich Chemical Company, INC (1978)
9. Orendorz, A.; Wusten, J.; Ziegler, C.; Gnaser, H. *Appl. Surface Science* (2005) **252** 85–88.
10. Eriksson, T.; Andersson, A.M.; Bishop, A.G; Gejke, C.; Gustafsson, T. and Thomas, J.O. *J. Electrochem. Soc.* (2002) **149** A69-A78.
11. Chiang, C.Y.; Shen, Y. J.*;* Reddy, M. J.; Chu, *P. P. J. Power Sources* (2003) **123** 222-229.

Chapter 6

Synthesis and Characterisation of TiO_2 Anatase nanotubes

6.1 Introduction

Anatase nanotubes have a variety of potential industrial applications such as photovoltaic cells[1], gas sensors[2], direct oxidation methanol fuel cells[3], proton conductors[4], solar energy conversion[5], photocatalysts[6-8] and, of course, lithium-ion technologies[9].

Many different synthetic approaches have been investigated to produce anatase nanotubes including anodisation, hydrothermal and template-based techniques[10-14]. Amongst all these synthesis techniques, the nanotubes of TiO_2 obtained via a hydrothermal route are of major significance due to the fact that the other synthesis techniques are either more expensive (for example template-based synthesis) or do not allow the same scale of nano-sizing in the final product (anodisation). Therefore the hydrothermal route is the synthetic process which allows production of small size anatase titania at a reasonable cost, with almost 100 % yield[13].

As previously discussed for the synthesis of TiO_2(B) nanotubes (see paragraph 3.2), the formation mechanism of TiO_2 nanotubes during the hydrothermal process involves the exfoliation of single-layer nanosheets from the pristine bulk TiO_2 in a

highly alkaline solution with subsequent scrolling of the sheets to give the nanotubular morphology[12, 15].

During this work, anatase nanotubes were prepared using a hydrothermal route, making use of the knowledge gained from the TiO_2(B) nanotubes[16]. The synthesis conditions were optimised in order to obtain both high purity and yield of an anatase structured material similar in both morphology and size to the previously discussed TiO_2(B) nanotubes.

6.2 Synthesis conditions

The TiO_2 precursor used for the nanotubes production was bulk titanium dioxide anatase powder (Aldrich, 98 % pure). In a typical synthesis, the bulk titania was dispersed in a 10 M sodium hydroxide solution, with a Ti and Na molar ratio of 1:13. The solution was then placed in a Teflon-lined autoclave and heated at 150 °C for 72 h.

The hydrothermal treatment led to the formation of single-layer nanosheets of sodium titanate following the scrolling of the sheets which produces the peculiar morphology. The product obtained at this stage of the process was hydrated titanate nanotubes, $Na_yH_{2-y}Ti_nO_{2n+1}$.

After the treatment and subsequent cooling, the product was filtered and subjected to ion exchange, using a 0.1 M aqueous solution of hydrochloric acid, until neutrality was reached, resulting in a hydrated titanate, $H_2Ti_nO_{2n+1}$.

Tsai *et al.*[17] observed that further acidic post-treatment washing, resulting on pH values of 1-2, led to high-porosity nanotubes having an X-ray diffraction pattern analogous to that of anatase TiO_2 rather than that of titanates. However, TEM images

revealed that this acidic post-treatment could compromise the nanotube morphology, in particular, on the surface of the tube walls. Clearly, the ion exchange is a very important and delicate stage for the successful synthesis of anatase nanotubes.

Moreover, EDX performed on the nanotube precursor of TiO_2(B) revealed the presence of residual sodium content between 2-3 % with respect to titanium.

Based on these observations, it was deduced that in order to obtain anatase structured nanotubes, a further acid-washing of the hydrated precursor treatment was required, until a pH value of 2-3 is reached. This results in the acidification of the titanate surface, without damaging the nano-morphology. In addition, no residual sodium was detected by EDX analysis of the anatase nanotube precursor subjected to the acidic post-treatment.

As shown in figure 6.1, the XRD patterns of these hydrated titanate nanotube precursors are very similar, although, a slight difference is observed in the intensity of the peak at 2θ equal to 28°, which is more pronounced in the TiO_2(B) precursor (in black) compared with the anatase precursor (in red).

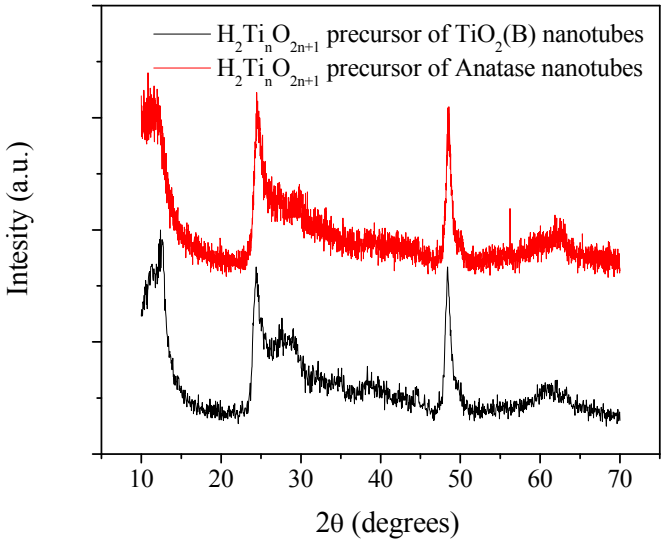

Figure 6.1 XRD pattern of hydrated titanate nanotubes precursors of TiO_2(B) (in black) and anatase (in red).

The washed precipitate is dried in an oven at 80 °C and finally annealed in order to remove the crystal water and to form the desired anatase phase, by heating the sample at 0.15 °C min^{-1} up to 380 °C where it was held for 10 min. The XRD pattern of the synthesised nanotubes is reported in figure 6.2.

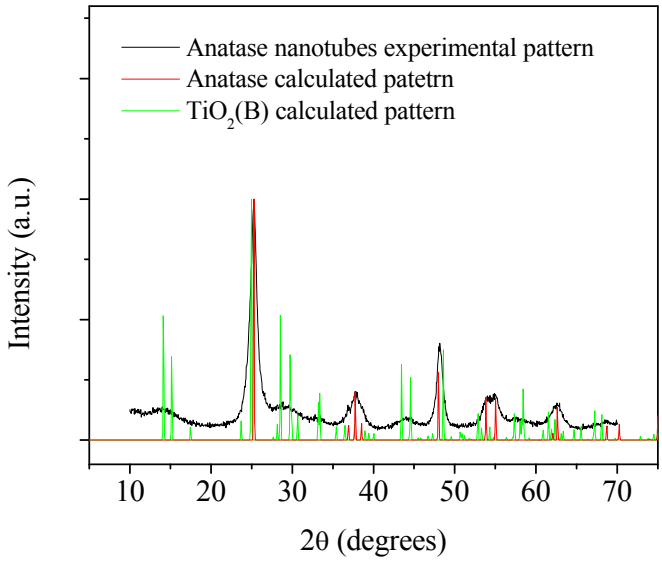

Figure 6.2 Experimental XRD pattern of anatase nanotubes (in black), anatase calculated pattern (in red) and TiO_2(B) calculated pattern (in green).

As can be observed, traces of the TiO_2(B) phase are present in the experimental pattern for the anatase nanotubes. It is noticeable at 2θ values of 12; 15; 30; 44 and 45° there are shoulders present in the experimental pattern that match the positions of the main peaks in the calculated TiO_2(B) pattern. This is not unexpected as the synthesis conditions for both products are very similar and thus a minimal amount of TiO_2(B) impurity would be likely to be found in all anatase nanotube sample.

6.3 Optimisation of the annealing conditions

As described in paragraph 3.2, TiO_2(B) nanotubes were obtained following the calcination of the hydrated titanate nanotubes at 400 °C for 2 h, with a heating rate of 2.5 °C min^{-1}. However, these annealing conditions were found to be unsuitable for the anatase nanotubes. In fact, the full width at half maximum (FWHM) value of the main anatase peak (2θ = 25.2°), in the XRD pattern of the anatase nanotubes, suggested the presence of crystalline impurities in the sample. Furthermore using the Scherrer equation[18] (eq. 6.1) the particle size was estimated to be 18 nm confirming the presence of crystalline impurities.

$$\tau = \frac{K\lambda}{\beta cos\theta} \tag{6.1}$$

The particle size was estimated using K as the shape factor, λ as the X-ray wavelength, β as the line broadening at half the maximum intensity (FWHM) in radians and θ as the Bragg angle.

It was, therefore, necessary to investigate and optimise the annealing conditions, in particular investigating each of the following aspects: annealing temperature, heating rate and the length of the isothermal step.

Prior to this, a thermogravimetric experiment was carried out in order to characterise the process involving the removal of the crystal water. The measurement was performed under flowing air with an heating rate of 2 °C min^{-1}. The thermogram of the experiment is reported in figure 6.3.

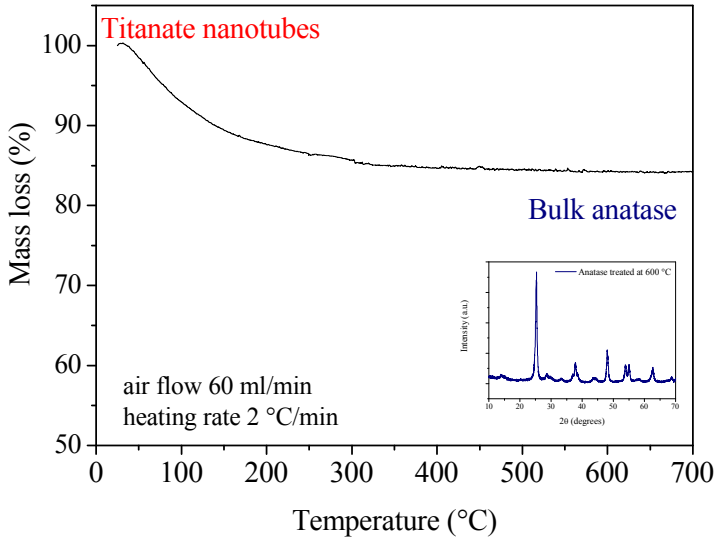

Figure 6.3 Thermogravimetric experiment performed under flowing air with a heating rate of 2 °C min^{-1} on the titanate nanotubes precursor.

It can be seen that the loss in mass associated with the removal of the crystal water occurs between 50-300 °C. Therefore, the minimum temperature required for the annealing is 300 °C.

6.3.1 Investigation of the optimal annealing temperature

Following the thermogravimetric measurements, various annealing temperatures in the range 300-500 °C were investigated. The XRD patterns of the samples after annealing are reported in figure 6.4 (a,b).

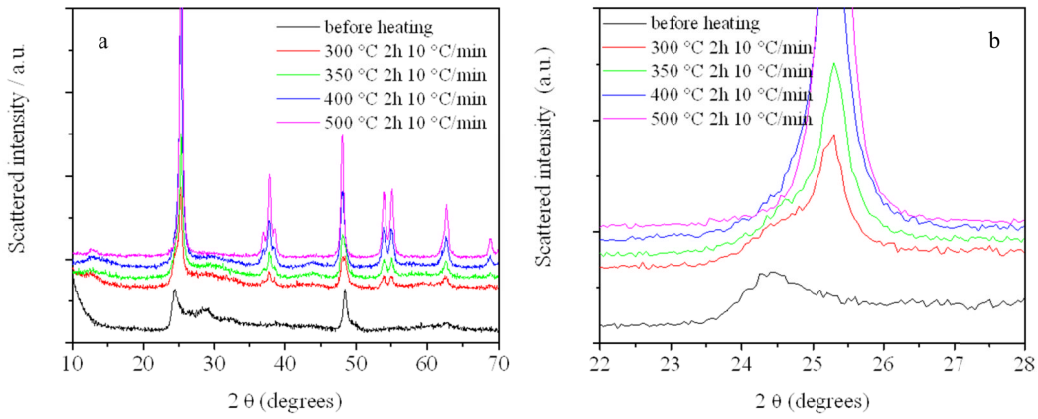

Figure 6.4(a) XRD pattern of anatase nanotubes annealed at different temperatures and (b) an enhanced picture of the main peak.

The purpose of this analysis was to establish the most suitable temperature, which allows the complete formation of the anatase structure from the titanate precursor, whilst avoiding the possible collapse of the nano-morphology and the formation of bulkier material.

It is evident from figure 6.4a that the intensity of the peaks, and therefore, the crystallinity of the samples increased with increasing annealing temperature. This was to be expected. However a closer look at the detailed picture of the main peak of anatase ($2\theta = 25.2°$) it can be seen that the titanate at $2\theta = 24.5°$ is still present for the sample annealed at 350 °C, implying that the 300 °C annealing temperature suggested by the TGA is not sufficiently high enough to fully convert the hydrated titanate precursor into the anatase structure. Further analysis of the detailed XRD

shows that above 400 °C the intensity of the main peak is increasing and the FWHM values of the same peak are decreasing, suggesting the structure is becoming more crystalline. Therefore, the ideal annealing temperature appears to range between 350 and 400 °C. In this temperature range the intensity of the dominant anatase peak at $2\theta = 25.2°$ still suggests a nanostructure.

TEM images were then taken for the samples calcinated at different temperatures. These are shown in figure 6.5. The homogeneous nanotubular morphology can be observed for the samples calcined at 300 and 350 °C. However, it can be seen that at 400 °C the sample has already started to lose its morphology suggesting the collapse of the nanotubular structure and formation of bulkier material. Furthermore, the sample treated at 500 °C clearly shows loss of nanotubes and presence of larger size particulates of anatase.

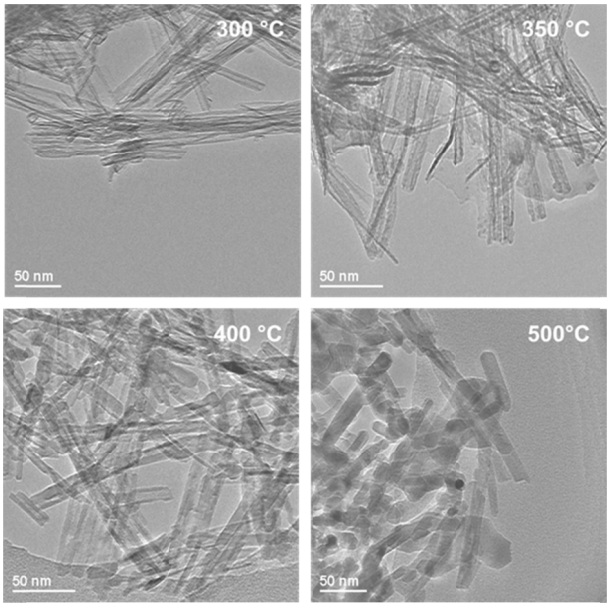

Figure 6.5 TEM images of anatase nanotubes annealed at different temperatures.

It can therefore be concluded that the optimal annealing temperature should be between 350 and 400 °C. The temperature chosen for the annealing was 380 °C, as reported in paragraph 6.2.

6.3.2 Investigation of the optimal heating rate

In order to optimise the heating rate, various rates were investigated, as reported in figure 6.6. Figure 6.6b shows a more detailed picture of the evolution of the main peak ($2\theta = 25.2°$) with increasing heating rate.

This analysis suggests that a high heating rate favours the formation of larger crystals in the sample and therefore a slower heating rate is required to prevent crystal growth in the sample.

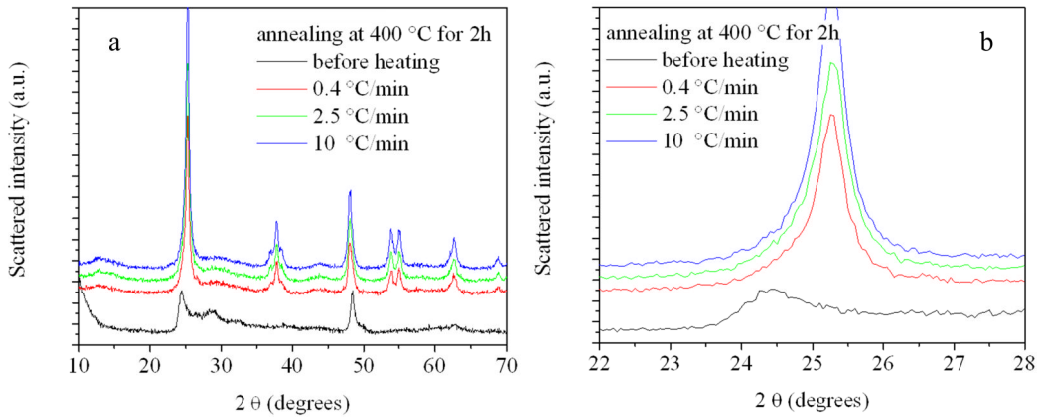

Figure 6.6 (a) XRD pattern of anatase nanotubes annealed at different heating rates and (b) an enhanced picture of the main peak.

TEM evidence has also confirmed the observation deducted from the XRD pattern, showing an increase in the presence of larger morphologies in the specimens annealed at a higher heating rate.

6.3.3 Investigation of the optimal isothermal step

The effect of the total time spent at the isothermal step was also investigated. The XRD patterns are shown in figure 6.7. It was observed that a long isothermal step favours crystal growth in the sample.

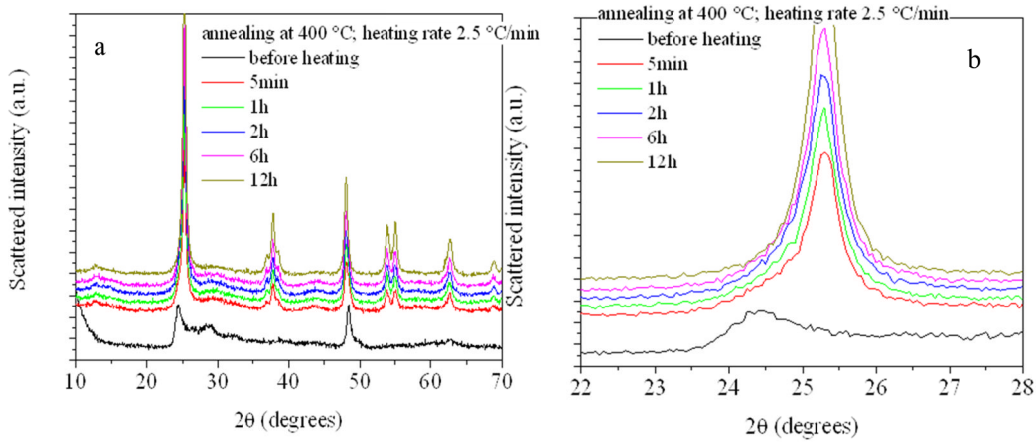

Figure 6.7 (a) XRD pattern of anatase nanotubes annealed at different length of the isothermal step and (b) an enhanced picture of the main peak.

It was confirmed with TEM images (fig. 6.8) whereby impurities can be seen in the annealed sample with an isothermal step of 2 h, and bulkier particles are evident for the samples calcinated with an isothermal step of 6 and 12 h. Therefore it was decided to use an isothermal step of less than 1 h to try and preserve the nanotubular morphology as much as possible.

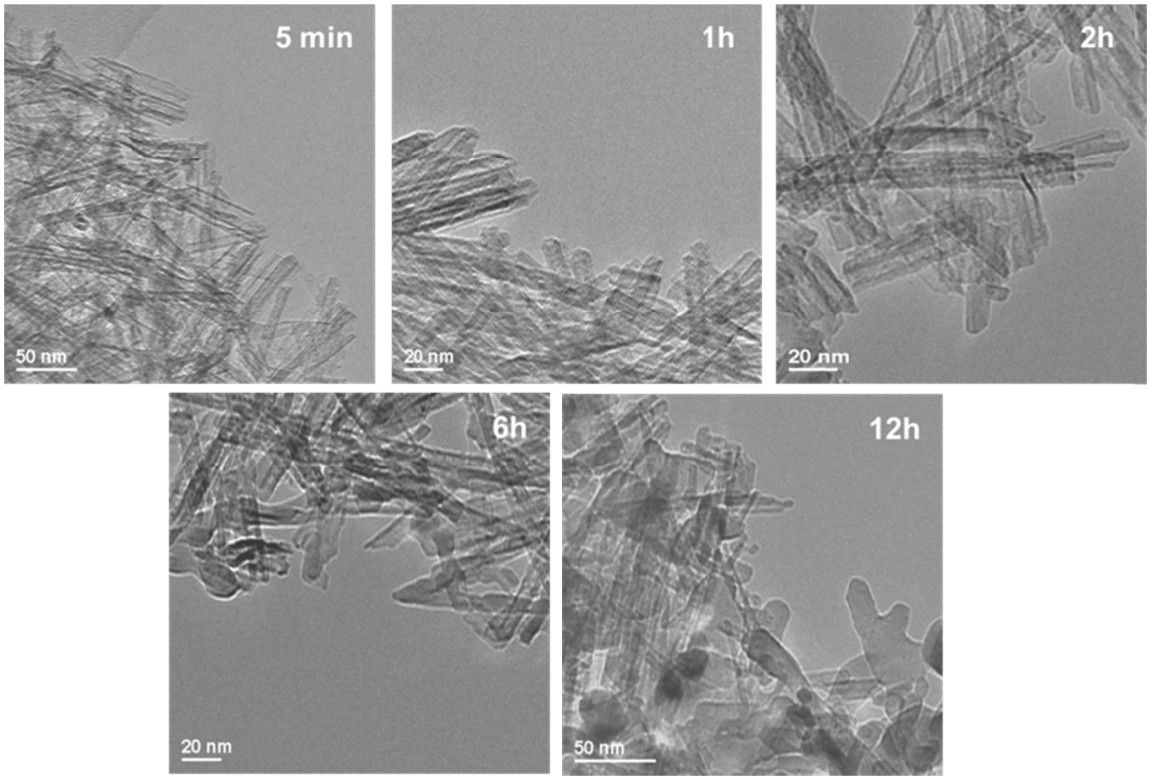

Figure 6.8 TEM images of anatase nanotubes annealed at different length of isothermal step.

6.3.4 Optimised conditions

Following all the research into optimising the annealing step of the synthesis, including results from XRD patterns and TEM image analysis, it was possible to produce the optimum conditions for maintaining nanotubes, whilst at the same time ensuring that the anatase structure has been formed. The particle size of the optimised sample was estimated using the Scherrer equation to be 8.7 nm which agrees with the TEM images of the nanotubes. The conditions are as follows: heating the sample at 0.15 °C min^{-1} up to 380 °C where it is held for 10 min.

6.4 Morphological characterisation of the anatase nanotubes

The morphology of the anatase nanotubes was investigated using the transmission electron microscope (TEM). TEM images confirmed the sample constituted mainly of nanotubes and this can be seen in figure 6.9. Evaluation of the dimensions of the nanotubes was then carried out. The wall thickness was estimated to range between 2-3 nm, the outer diameter between 8-10 nm and lengths of the tubes between 30-100 nm.

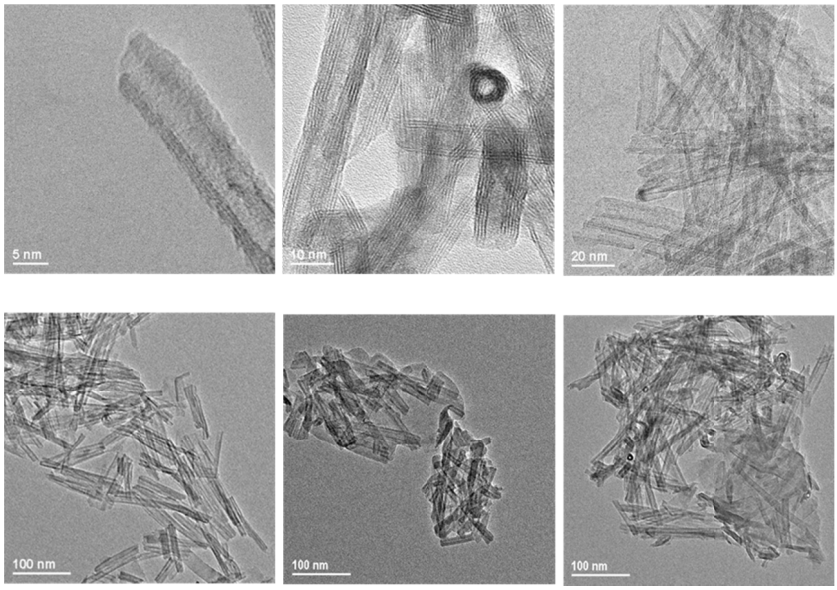

Figure 6.9 TEM images of anatase nanotubes at high (top) and low (bottom) resolution.

From the TEM images taken at high resolution, the presence of few morphological impurities, such as sintered fragments of broken tubes or collapsed tubes was also observed, whereas low resolution images showed the minor presence of unfolded sheets in the specimen. The morphological impurity of the sample based on TEM imaging analysis can be estimated to be around 10 %.

Images collected using a field emission scanning electron microscope (FESEM) (reported in figure 6.10), confirmed the high morphological homogeneity of the sample, consisting mainly of tubular nanoparticulates. Indeed, impurity contamination was not observable, thus suggesting that the percentage of the impurities present in the specimen must be rather low and very difficult to quantify.

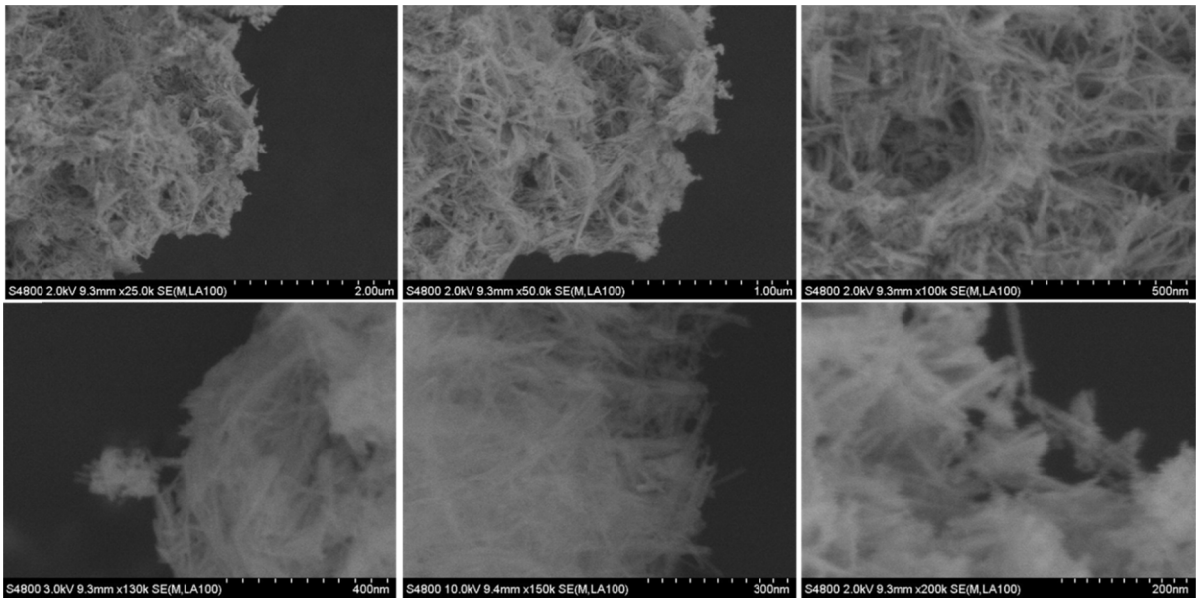

Figure 6.10 FESEM images of anatase nanotubes at high (top) and low (bottom) resolution.

An estimation of the level of morphological purity of the optimised sample can be obtained using BET surface area measurements. The theoretical surface area for an ideal (100 %) nanotube sample can be predicted by using the dimensions of the tubes (length and thickness) evaluated from the TEM images.

The surface area per unit mass (S) of a nanotube is given by the following equation:

$$S = \frac{2(L_{NT}+h_{NT})}{\rho L_{NT} h_{NT}} \qquad 6.2$$

Where L_{NT} and h_{NT} are the length and the wall thickness of the tube respectively, and ρ =3.896 g cm^{-3} is the density of the material. The expression can be further simplified to the following, which does not take into consideration the thickness of the nanotubes, thus assuming the area of the cross section is negligible:

$$S = \frac{2}{\rho h} \qquad 6.3$$

Using the values obtained from the TEM images, the theoretical surface area of a 100 % nanotube sample, with a wall thickness of 2 nm, was calculated to be 250 m^2 g^{-1}. The experimental surface area of the hydrated titanate precursor was found to be 240 m^2 g^{-1}, which is very similar to the surface area of the theoretical 100 % sample.

The experimental surface area of the optimised anatase nanotubes sample was found to be 220 m^2 g^{-1}, suggesting 80-85 % level of morphological purity.

This value of the BET surface area obtained for the anatase nanotubes is very close to the one obtained for the TiO_2(B) nanotubes, which means the optimised annealing allowed anatase nanotubes to be produced with the same degree of morphological purity as the TiO_2(B) nanotube sample.

Nevertheless, these surface area values for both the TiO_2 phases are lower compared with the titanate precursors, suggesting once again that the annealing step is the most delicate stage of the synthesis, where the nanotubular morphology is damaged and most of the impurities are formed, as already observed from the TEM image analysis in paragraph 6.3.

6.5 Other Anatase nano-morphologies investigated

In order to establish the improvement provided by the size and the morphology of the nanotubes produced in terms of application as an anode material for lithium-ion batteries, it was necessary to compare them with anatase samples of a different morphology and different size.

For this purpose four different anatase samples were used: three nanoparticle samples with a diameter of 6 nm (Amt-100, Tayco), 15 nm nanoparticles (Tronox) and larger nanoparticles of 45 nm (Alfa Aesar). Also used as a comparison was bulk anatase which has particles of 196 nm (Sigma Aldrich).

The XRD patterns of the synthesised anatase nanotubes are reported in figure 6.11 together with the anatase samples investigated for comparison.

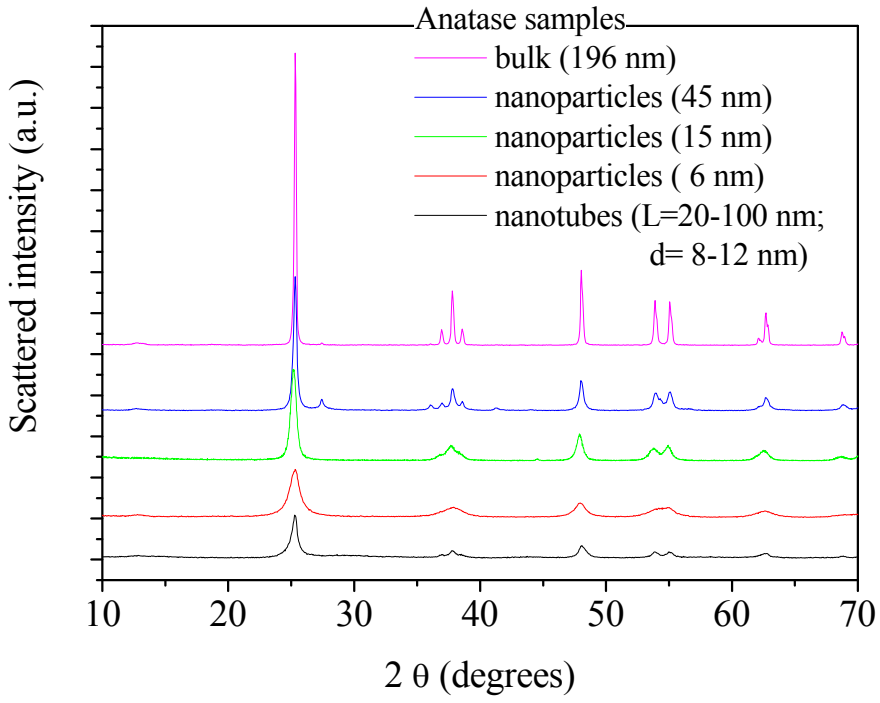

Figure 6.11 Experimental XRD patterns of anatase samples.

As expected, the larger particles show a higher degree of crystallinity. It is also evident that traces of the rutile phase are present in both of the larger particles, as shown by the presence of a peak 28° in the XRD pattern.

In order to fully appreciate the minor differences in the XRD patterns for the three nanomaterials, a more detailed comparison is shown in figure 6.12, where the anatase nanotubes are compared with the two nanoparticle materials, which have dimensions close to the produced nanotubes.

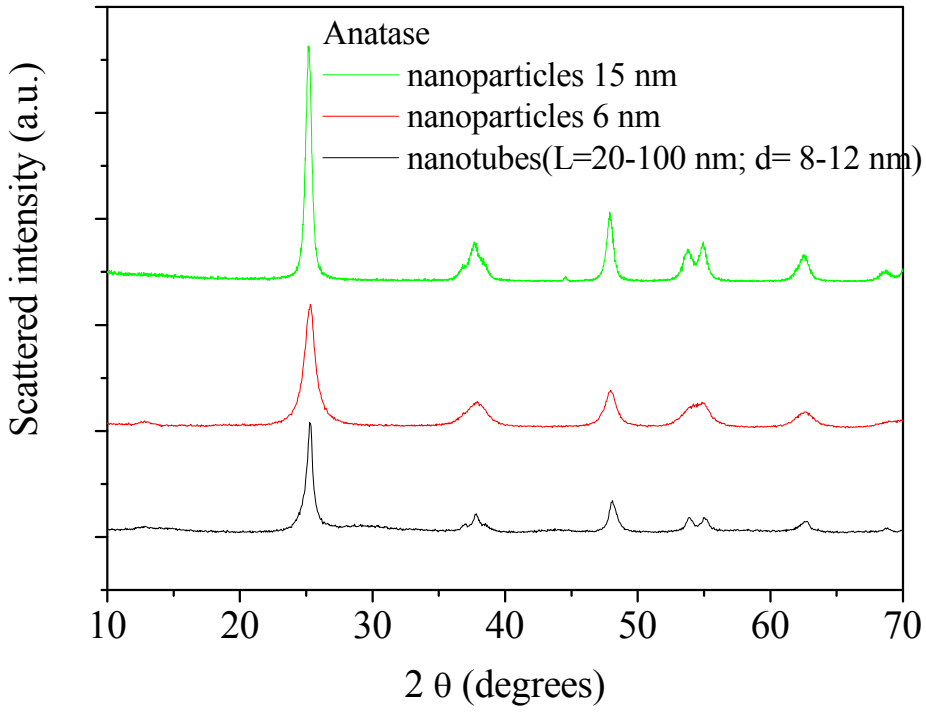

Figure 6.12 Experimental XRD pattern of anatase nanotubes (in black), anatase 6 nm nanoparticles pattern (in red) and anatase 15 nm nanoparticles (in green).

As expected, the nanotubes are less crystalline than the 15 nm particles and more crystalline than the 6 nm nanoparticles. This can be observed as the intensity of the main anatase peak at 2θ = 25.2° is greater for the 15 nm particles and much broader

for the 6 nm nanoparticles when compared with the nanotubes. Furthermore, the triplet at 37, 37.8 and 38.5°, which is defined for the 15 nm nanoparticles, is still recognisable as a triplet for the nanotubes, but not well defined for the smaller nanoparticles. Evaluation of the particle size was performed using the Scherrer equation[18]. The estimated sizes are reported in table 6.1. The larger values suggest the presence of particles larger than claimed by the product.

Sample	**d_{hkl} (nm)**
Anatase nanoparticles (6 nm)	11
Anatase nanoparticles (15 nm)	24
Anatase nanoparticles (45 nm)	45
Anatase bulk (196 nm)	196

Table 6.1 Estimated particle size of the anatase samples obtained using the Scherrer equation.

The morphology of the samples was also investigated using TEM. In figures 6.13 and 6.14 the images for all of the relevant materials are shown. As can be seen there are large differences in particle size and they all display a spherical morphology. The particle size of the various specimens was also estimated and is found to be to be agreeable with the XRD particle size estimate.

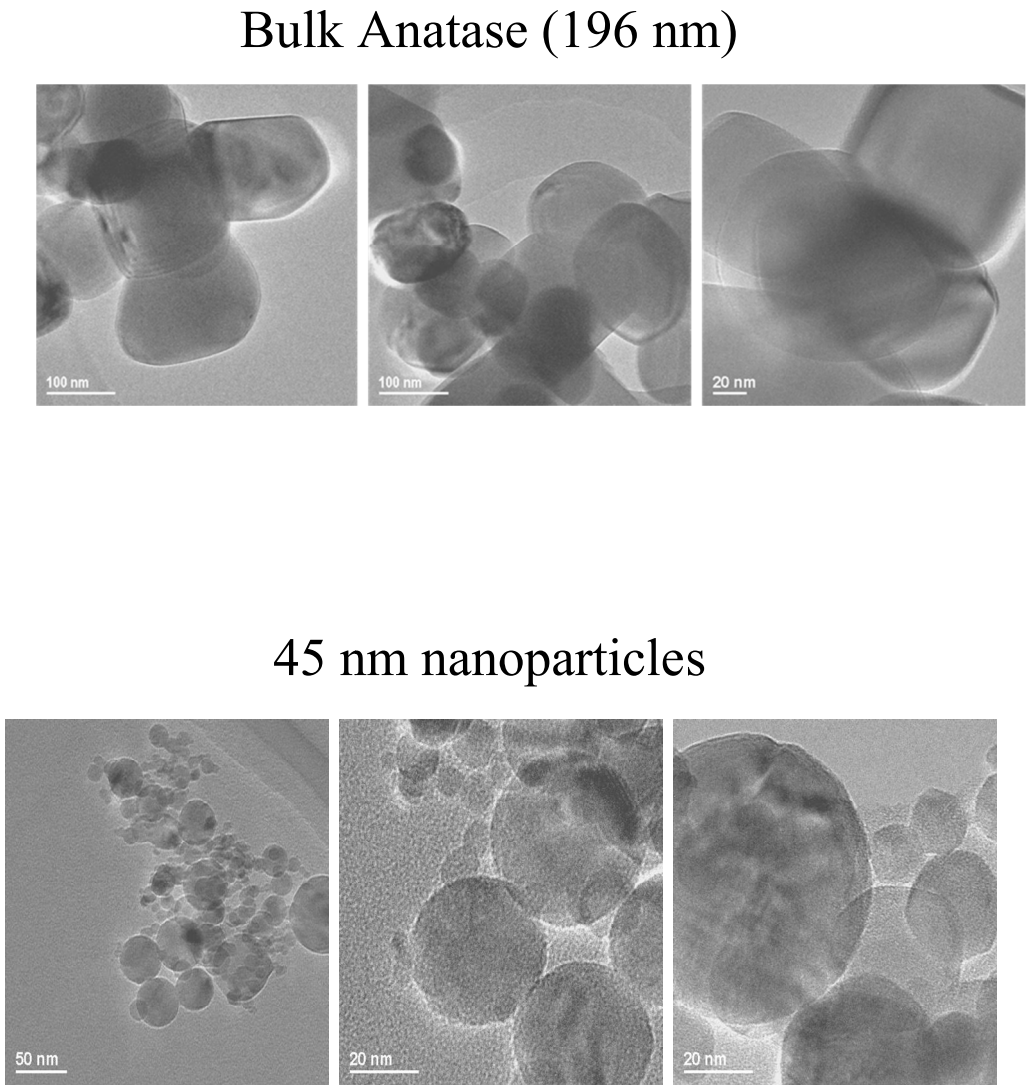

Figure 6.13 TEM images of bulk anatase (top) and 45 nm (bottom) anatase particles.

15 nm nanoparticles

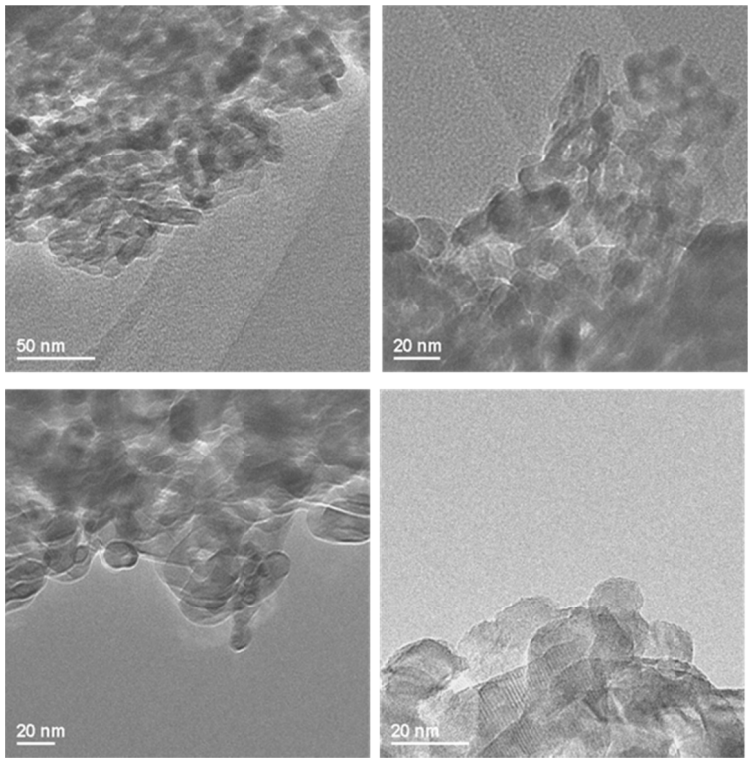

6 nm nanoparticles

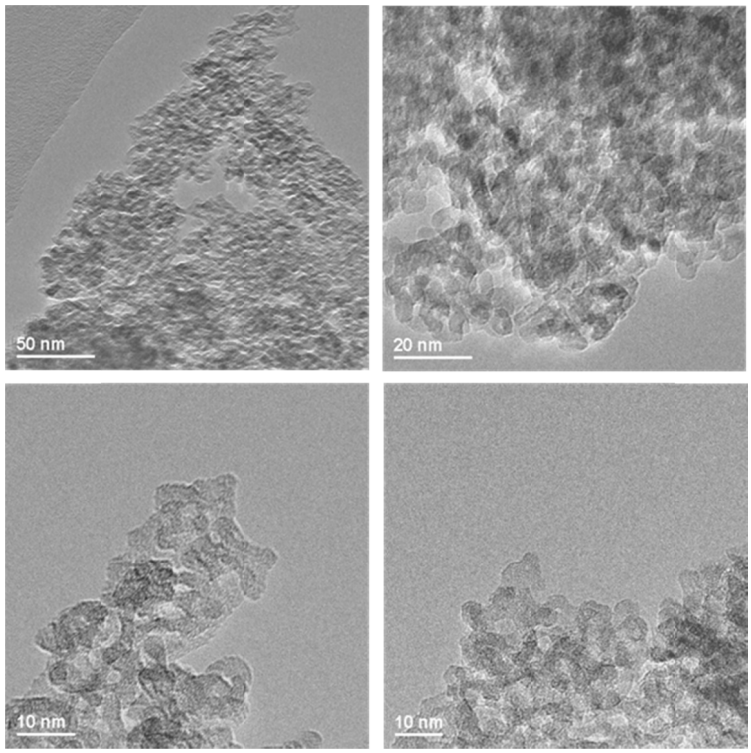

Figure 6.14 TEM images of 15 nm (top) and 6 nm (bottom) anatase nanoparticles.

6.6 Chapter conclusions

Anatase nanotubes were successfully synthesised following a modified procedure originally used for the production of TiO_2(B) nanotubes. Following investigations into the annealing procedure, an optimised set of calcination conditions were defined and resulted in a level of purity for the anatase nanotubes in the region of 80-85 %. This level of purity is consistent with the previously synthesised TiO_2(B) nanotubes, described in chapter 3.

This material has been fully characterised using several techniques including XRD, TEM, FESEM and BET surface area measurements.

Relevant commercially available materials with different morphologies and particle size were also characterised as they will be used as comparison materials for the anatase nanotubes, in order to establish the effect of particle size and morphology on the electrochemical properties, which is discussed in the next chapter.

References

1. Lu, M-D. and Yang, S-M. *Synth. Met*. (2005) **154** 73.

2. Varghese, O.K.; Gong, D.; Paulose, M.; Ong, K.G. and Grimes, C.A. *Sens. Actuators B* (2003) **93** 338-344.

3. Wang, M.; Guo, D-J.; Li, H-L.; *J. Solid State Chem.* (2005) **178** 1996.

4. Kasuga, T. *Thin Solid Films* (2006) **496** 141-145.

5. Mor, G.K.; Varghese, O.K.; Paulose, M.; Shankar, K. and Grimes, C.A. *Sol. Energy Mater. Sol. Cells* (2006) **90** 2011-2075.

6. Raja, K.S.; Misra, M.; Mahajan, V.K.; Gandhi, T.; Pillai, P. and Mohapatra, S.K. *J. Pow. Sources.* (2006) **161** 1450-1457.

7. Gao, Z.; Yang, S.; Sun, C. and Hong, J. *Sep. Purif. Technol.* (2007) **58** 24-31.

8. Yu, J.; Yu, H.; Chenga, B. and Trapalis, C. *J. Mol. Catal. A: Chem.* (2006) **249** 135.

9. Kavan, L.; Kalbac, M.; Zukalova, M.; Exnar, I.; Lorenzen, V.; Nesper, R. and Graetzel, M. *Chem. Mater.* (2004) **16** 477.

10. Eder, D.; Kinloch, I.A. and Windle, A.H. *Chem. Commun*. (2006) **13** 1448–1450.

11. Richter, C.; Wu, Z.; Panaitescu, E.; Willey, R.J. and Menon, L. *Adv. Mater.* (2007) **19** 946–948.

12. Kasuga, T.; Hiramatsu, M.; Hoson, A.; Sekino, T. and Niihara, K. *Adv. Mater* (1999) **11** 1307-1311.

13. Baiju, K.V.; Shuka, S.; Biju, S; Reddy, M.L.P. and Warrier, K.G.K. *Catal. Lett.* (2009) **131** 663-671.

14. Li, X.H.; Liu, W.M. and Li, H.L. *Appl. Phys. A* (2005) **80** 317–320.

15. Bavykin D.V., Friedrich J.M. and Walsh F.C., *Adv. Mater.* (2006) **18** 2807-2824.

16. Armstrong A.R., Armstrong G., Canales J. and Bruce P.G., *Angew. Chem.* (2004) **43**, 2286-2288.

17. Tsai C-C. and Teng H., *Chem. Mater.* (2006) **18** 367-373.

18. Langford, J.I.; Wilson, J.C. *J. Appl. Crystallogr.* (1978) **11** 102.

Chapter 7

Electrochemical performance of TiO_2 Anatase materials

7.1 Introduction

Titanium dioxide is capable of hosting a large amount of lithium ions at low voltage and hence is very attractive for use as an anode in rechargeable lithium-ion batteries. The synthesis of nanoparticulate forms of titanium dioxide has further increased interest in such applications, since dimensional confinement has been found to have a significant effect on the intercalation properties of TiO_2[1]. In this chapter the electrochemical performance of the anatase nanotubes successfully produced via hydrothermal synthesis, described in chapter 6, has been investigated. Furthermore, their performance is compared with other commercial anatase materials differing from the tubes in both morphology and size. The purpose is to investigate how the singular 1D nano-morphology affects the performance of anatase in lithium batteries compared with the spherical nanoparticles.

7.2 Electrochemical performance

7.2.1 Comparison of lithium uptake

Bulk anatase can host 0.5 equivalents of lithium in its structure[2], providing a maximum capacity of 168 mAh g^{-1}. This value corresponds to half of the capacity of the TiO_2(B) bulk, which can host 1 lithium atom per formula unit[3].

Nano-structuring can have a remarkable effect on the insertion properties of anatase, and can significantly increase the amount of lithium which can be accommodated in the structure[1].

In figure 7.1 the load curves of different sized anatase samples are shown. The measurements were recorded using galvanostatic conditions with a current rate of 10 mA g^{-1}.

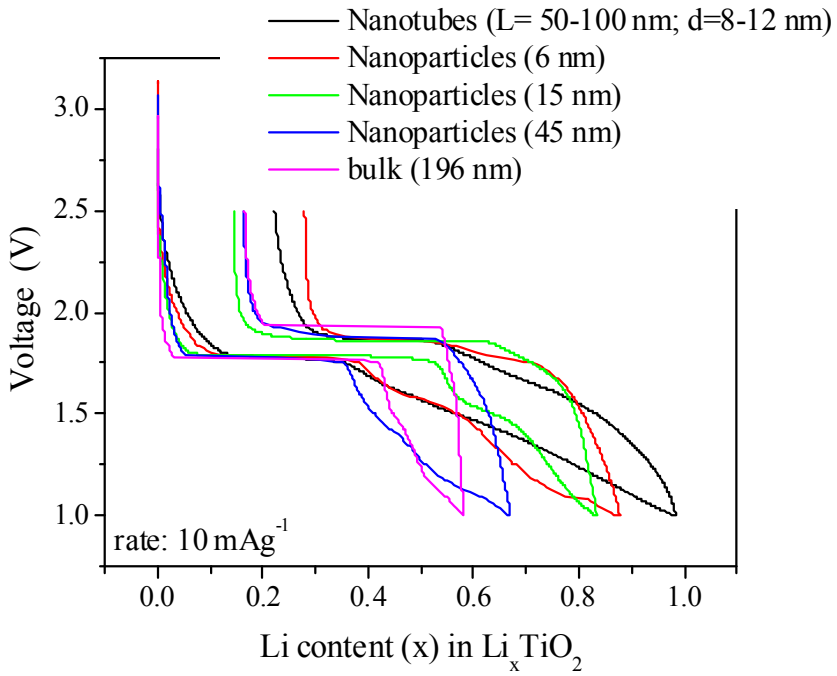

Figure 7.1 Load curves of different sized anatase samples recorded in galvanostatic conditions with a current rate of 10 mA g^{-1}.

As can be seen, only 0.6 equivalents were inserted in the material consisting of larger particles (196 nm), resulting in a specific capacity of 201 mAh g^{-1}. The reduction in the particle size results in a remarkable increase in lithium uptake. The 45 nm nanoparticles were able to accommodate almost 0.7 equivalents of lithium in the structure; the 15 nm nanoparticles inserted more than 0.8 and the 6 nm nanoparticles reached almost 0.9 equivalents of lithium. However, the maximum amount of lithium accommodated in the structure was observed in the anatase nanotubes load curve, where 0.98 equivalents of lithium were inserted into the structure.

This dramatic effect can be related to changes in the thermodynamics of the lithium insertion/removal process determined by the nano-sizing. This effect will be further discussed in paragraph 7.3.

7.2.2 Galvanostatic cycling of anatase materials

The performance of the anatase samples was tested using galvanostatic cycling. The experiments were performed at a charge/discharge rate of 100 mA g^{-1} (~0.11 mA cm^{-2}, C/3) and in a voltage range between 1-2.5 V.

In figure 7.2 the specific capacity over 100 cycles of all the materials investigated is shown. As expected, an enhancement of the capacity of intercalated and de-intercalated lithium was observed with a decrease in the particle size.

The bulkier materials display rapid capacity decay. This decay, however, may be related not only to the active material itself, but also to the manufacturing of the electrodes. The optimisation of the composition and the manufacturing of the electrode for the bulkier materials could overcome this issue, for example, by increasing the amount of electronic conductor (carbon) and decreasing the quantity

of the active material (TiO_2). This combination would enhance the performance in terms of capacity per mass of active material; however, it would also result in a loss in terms of capacity per mass of overall electrode.

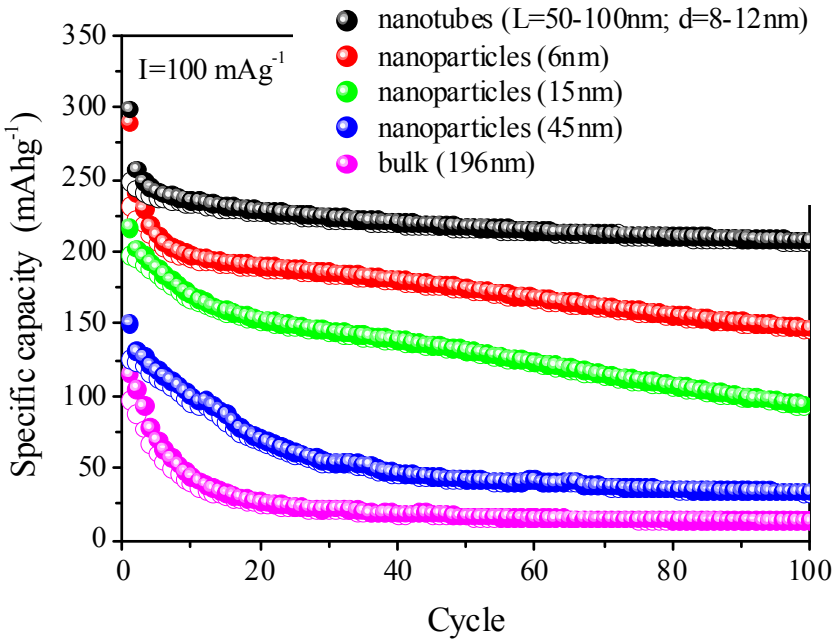

Figure 7.2 Specific capacities in charge (hollow) and discharge (filled) over 100 cycles for the different sized anatase samples.

The 6 nm nanoparticles and the nanotubes exhibit the greatest specific capacity, almost 50 mAh g^{-1} greater than the 15 nm nanoparticles.

A similar comparison to the one seen for the gravimetric experiments is made by reporting the volumetric performance which is presented in figure 7.3. In this case, the anatase nanotubes outperform all the other anatase morphologies under investigation. The nanotubes exhibit a capacity ~400 mAh cm^{-3} greater than the 6 nm nanoparticles. This is due to the higher density of the nanotube electrode.

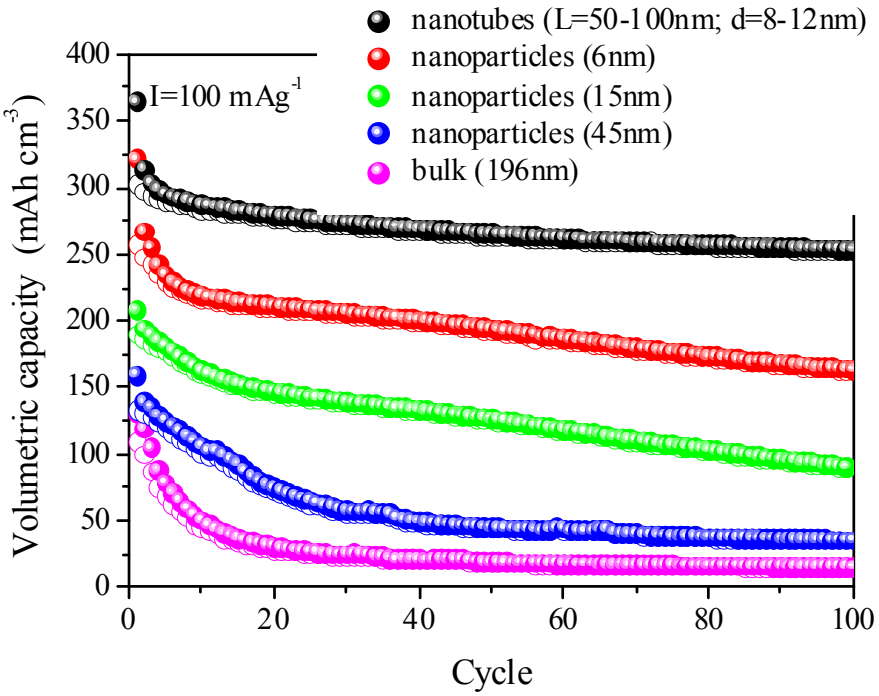

Figure 7.3 Volumetric capacities in charge (hollow) and discharge (filled) over 100 cycles for the different sized anatase samples.

Moreover, the anatase nanotubes exhibit superior capacity retention over cycling, exceeding 70 % at the 100th cycle in respect to the first discharge, compared with 51 % for the 6 nm nanoparticles. It is to be noted that *post mortem* TEM image investigation of the nanotube electrodes showed retention of the 1D morphology of the nanomaterial upon repeated lithium insertion/removal, as shown in figure 7.4.

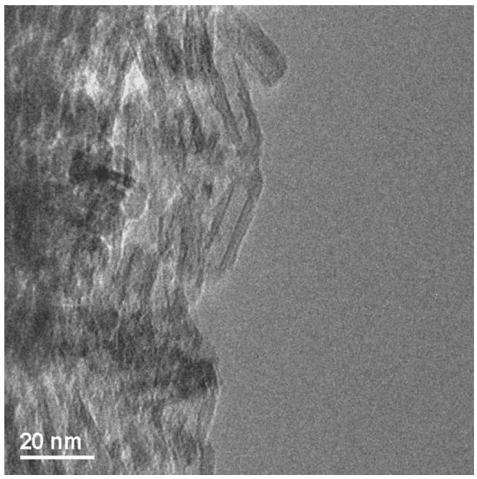

Figure 7.4 TEM image of composite electrode of anatase nanotubes cycled 100 times at 100 mA g^{-1}.

The performance at different charge/discharge rates of the anatase nanotubes was also investigated. Figure 7.5 reports the rate performance for one cell collected at various charge/discharge rates between 33 mA g^{-1} (C/10) and 1500 mA g^{-1} (5C) (corresponding to one lithium per formula unit inserted in 10 h and in 12 minutes, respectively; 1C is equivalent to 335 mA g^{-1})

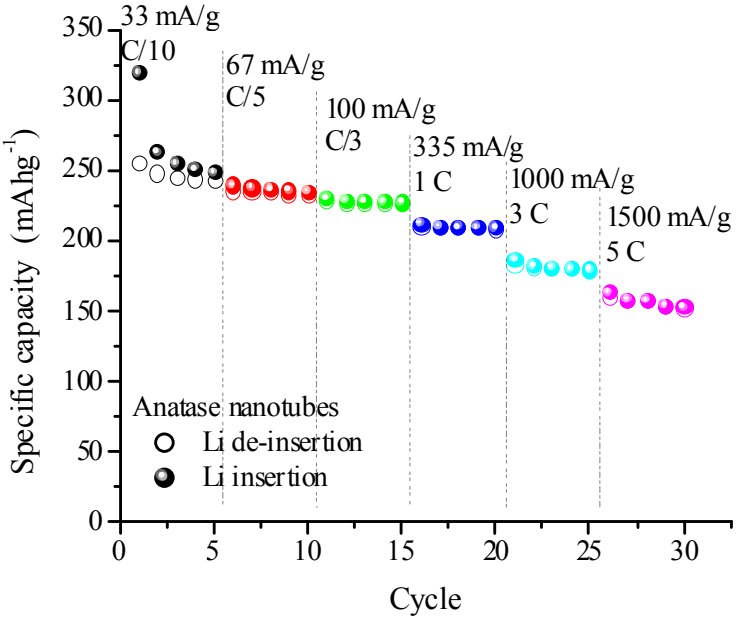

Figure 7.5 Performance of one cell cycled at various charge/discharge rates between C/10 and 5C.

A similar evaluation of the performance at higher rates is provided by reporting the capacity over a large number of cycles for different rates, as shown in figure 7.6, where the anatase nanotube performance was tested at various charge/discharge rates ranging between 333 mAh g^{-1} (3C) and 6000 mAh g^{-1} (20C).

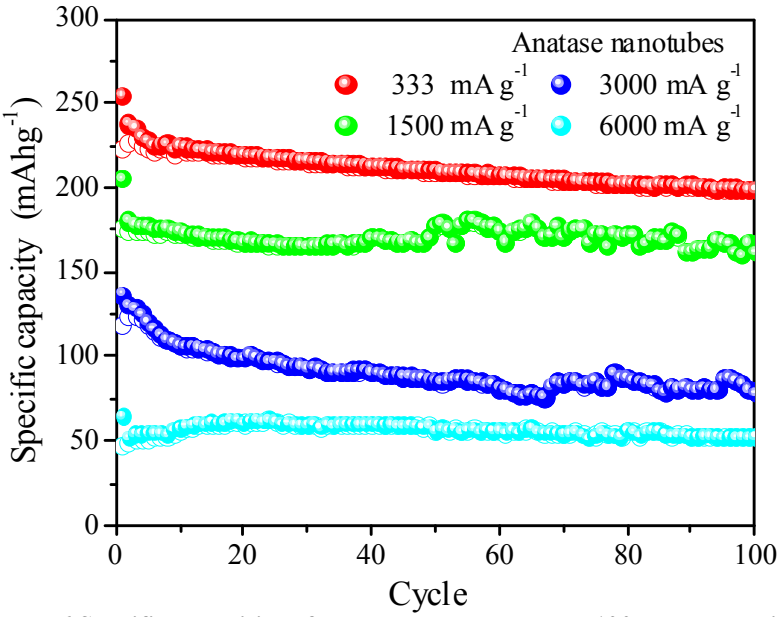

Figure 7.6 Specific capacities of anatase nanotubes over 100 cycles at differing charge/discharge rates.

As can be seen in figure 7.6, the anatase nanotubes exhibit good capacity even under fast charge/discharge conditions. All the experiments have been carried out on 2 electrode cells; however for high rates, such as 6000 mA/g, it would be advisable to use a three electrode set up using lithium as a reference.

7.2.3 Irreversible capacity and coulombic efficiency

As shown in figures 7.2 and 7.3, all anatase samples suffer from capacity loss between the first discharge and the first charge. In other words, a certain amount of the lithium inserted during the first discharge cannot be extracted during charging and is, therefore, irreversibly consumed. A measure of this phenomenon is given by

the coulombic efficiency after the first cycle, which is reported in table 7.1 for current rates of 10 and 100 mA g^{-1}. In table 7.1 the irreversible capacity observed for all of the samples at both current rates is also reported.

	Coulombic efficiency at 1st cycle		**Irreversible capacity (mAh g^{-1})**	
	I=100 mA g^{-1}	I=10 mA g^{-1}	I=100 mA g^{-1}	I=10 mA g^{-1}
Anatase nanotubes	83%	77%	50.4	74.5
Anatase nanoparticles (6 nm)	80%	68%	58.3	93.5
Anatase nanoparticles (15 nm)	91%	82%	19.1	48.5
Anatase nanoparticles (45 nm)	83%	75%	24.6	54.4
Anatase bulk (196 nm)	84%	71%	18.1	55.3

Table 7.1 Coulombic efficiency and irreversible capacity after the first cycle for the different sized anatase materials run at 10 and 100 mA g^{-1}.

There is no clear trend observed for the irreversible capacity with nominal particle size. Taking into account the surface area obtained by BET measurements for the materials under investigation (reported in table 7.2), the value of the irreversible capacity for the both current rates was plotted as a function of the surface area (fig.7.7). A general trend is observed as the irreversible capacity increases with samples displaying larger surface areas. The observed trend also suggests that there must be a critical value of surface area beyond which the irreversible capacity increases and this must be located between 10 and 6 nm particle size (100 and 200 m^2 g^{-1}).

Surface area BET (m^2 g^{-1})	
Anatase nanotubes	225.5
Anatase nanoparticles (6 nm)	285.8
Anatase nanoparticles (15 nm)	93.8
Anatase nanoparticles (45 nm)	48.7
Anatase bulk (196 nm)	8.5

Table 7.2 BET surface area values for the anatase nanotubes, different sized nanoparticles and bulk anatase.

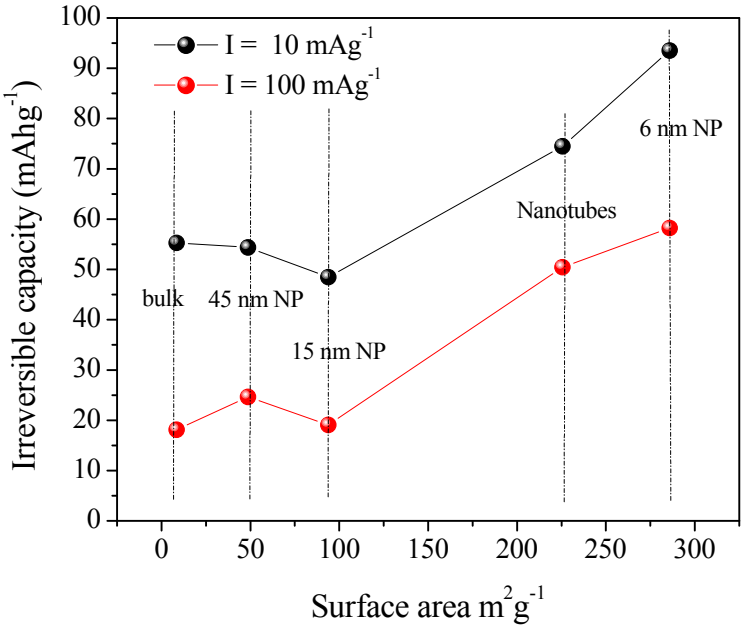

Table 7.7 Irreversible capacity *vs* surface area of different sized nanoparticles, recorded at 10 and 100 mA g^{-1}charge/discharge current rates.

This trend was further confirmed at various rates, ranging between 10 and 1500 mA g^{-1} for the three nano-structured samples investigated. As can be observed in figure 7.8, the 15 nm nanoparticles show the highest coulombic efficiency, followed by the nanotubes and then the 6 nm nanoparticles.

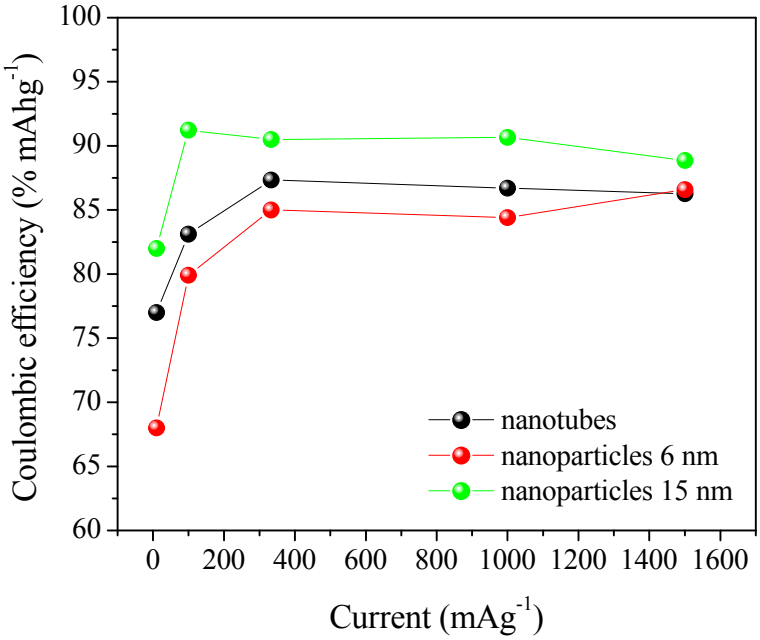

Figure 7.8 Coulombic efficiency observed after the first cycle of the anatase nanotubes, 6 nm nanoparticles and 15 nm nanoparticles at differing rates.

As a consequence, the irreversible capacity may be directly related to the increased surface area of the nano-particulates. On the other hand, the lithium uptake is not simply dependent on the surface area. The reason for the higher uptake of lithium in the nanotubes is expected to be found in their peculiar morphology.

7.2.4 Capacity retention

The performance at 100 mA g^{-1} in terms of specific capacity (fig.7.2) and volumetric capacity (fig.7.3) for the various anatase samples highlights improved capacity retention over a large number of cycles exhibited by the anatase nanotubes compared with both the 6 and 15 nm nanoparticles.

The investigation of the capacity retention for the three nano-sized materials at various rates is summarised and reported in figure 7.9, for the 2nd (a) and the 100th cycle (b) respectively.

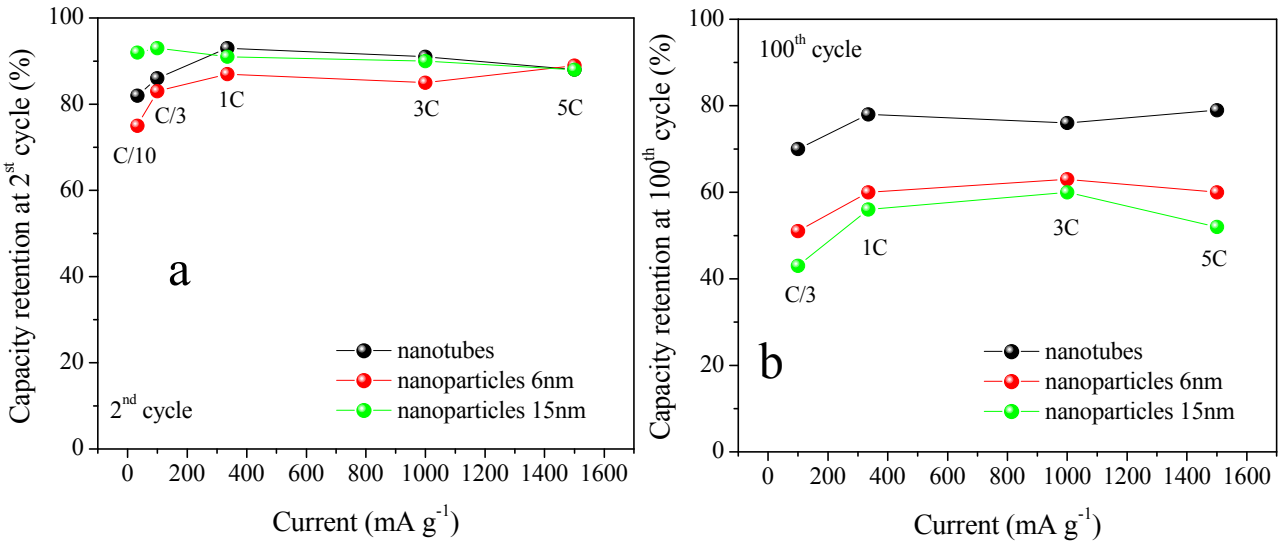

Figure 7.9 Capacity retention after the 2nd (a) and 100th (b) cycle for the nanotubes, 6 nm nanoparticles and 15 nm nanoparticles at differing rates.

The value of the capacity retention for the 2nd cycle is very close for all three samples, with the exception of the low rate cycling, where the nanotubes and the 6 nm nanoparticles show lower values than the 15 nm nanoparticles. On the other hand, at the 100th cycle, the anatase nanotubes outperform both the 6 and 15 nm nanoparticles.

In figure 7.10 the amount of lithium inserted at different stages of the galvanostatic cycling is shown, for the first, 10th, 50th and 100th cycle, and is reported as a function of the various current rates.

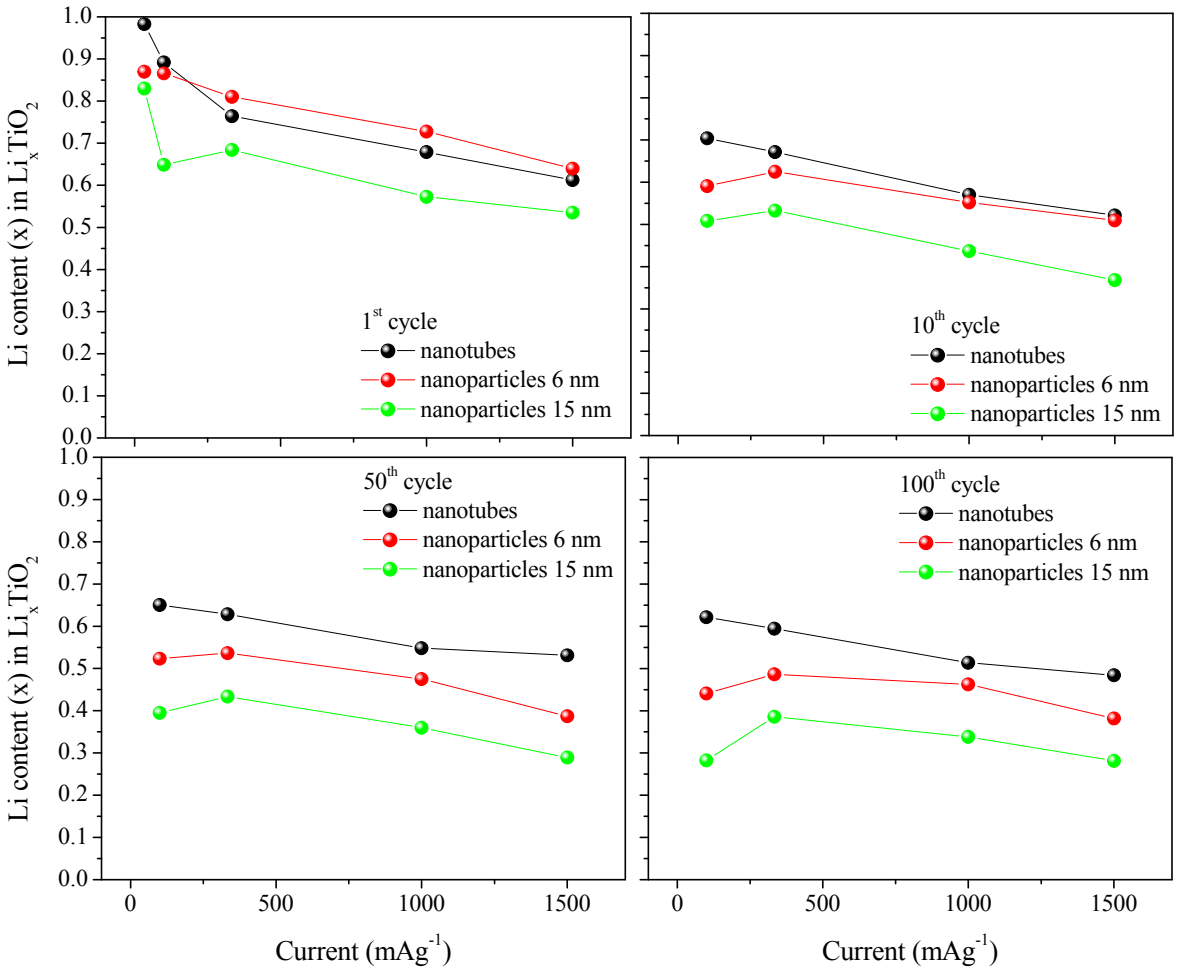

Figure 7.10 Equivalents of lithium inserted for the 1st; 10th; 50th and 100th cycle for anatase nanotubes, 6 nm nanoparticles and 15 nm nanoparticles at differing rates.

As can be seen, after the 50^{th} and 100^{th} cycles, a significant difference in the total amount of lithium inserted in the nanotubes is observed compared with all the nanoparticle samples.

As expected, the nano-structuring enhances the kinetics and the reversibility of the lithium insertion process. The reduced particle size shortens the diffusion paths for the lithium ions in the structure, making the lithium uptake and removal process fast and highly reversible.

The higher lithium uptake exhibited by the nanotubes, in comparison with the 6 nm nanoparticles, can be explained by taking into consideration the wall thickness, estimated to be between 2-3 nm by TEM image analysis (see chapter 6), compared with the effective radius of the 6 nm nanoparticles (6-11 nm, see chapter 6).

Moreover, due to their peculiar 1D nano-morphology, which is maintained upon cycling, and their long length, the nanotubes allow a closer packing within the electrode, and therefore a better contact with the other electrode components, i.e. the electronic conductor (carbon). The combination of the shortened diffusion path and the improved electronic conductivity within the electrode, together with the structural flexibility (reduced cracking during cycling) resulted in the greater capacity retention displayed by the anatase nanotubes.

The load curves for the galvanostatic cycling carried out at 100 mA g^{-1} on the nanotubes and the 6 nm nanoparticles at various cycles are reported in figures 7.11 and 7.12 respectively.

As can be seen, the curves are in good agreement with the load curves carried out with a current rate of 10 mA g^{-1}.

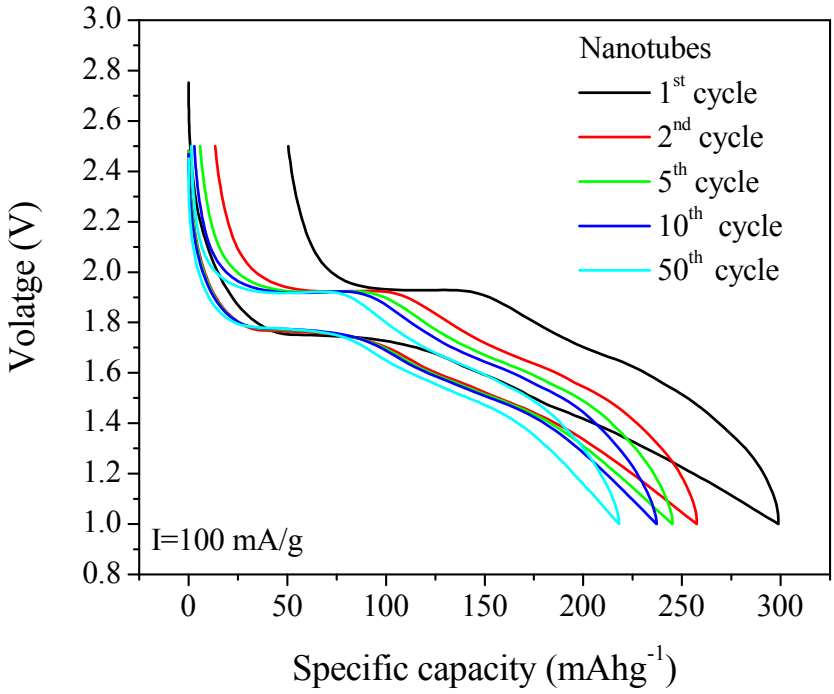

Figure 7.11 Load curves for the anatase nanotubes recorded at 1th, 2nd, 5th, 10th and 50th cycle during galvanostatic cycling with a current rate of 100 mA g^{-1}.

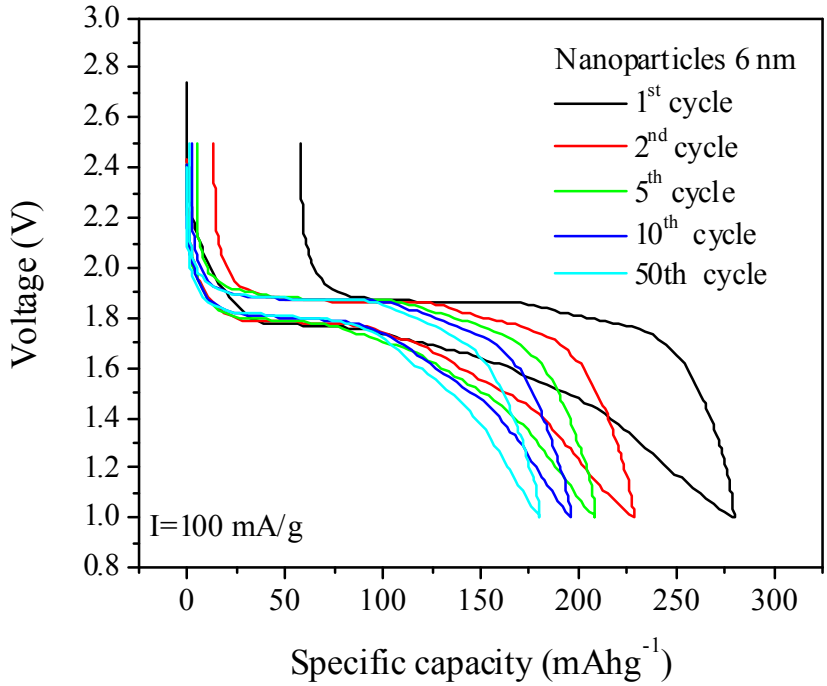

Figure 7.12 Load curves for the 6 nm anatase nanoparticles recorded at 1th, 2nd, 5th, 10th and 50th cycle during galvanostatic cycling with a current rate of 100 mA g^{-1}.

The load curves clearly consist of three different regions. The quantity of charge, Q, obtained during the discharge at each of the three different regions is reported in table 7.3.

	Nanotubes			**Nanoparticles (6 nm)**		
Discharge 100 mA g^{-1}	Q 1st Slope (mAh g^{-1})	Q Plateau (mAh g^{-1})	Q Tale (mAh g^{-1})	Q 1st Slope (mAhg^{-1})	Q Plateau (mAh g^{-1})	Q Tale (mAh g^{-1})
1st cycle	43.7	74.9	180.4	33.7	101.1	173.2
2nd cycle	29.5	68.7	158.8	23.3	81.5	122.7
5th cycle	30.4	67.8	144.8	23.3	72	127.8
10th cycle	30.47	66.2	139.8	23.3	72	99.7
50th cycle	29.0	54	135	23.3	69.7	86

Table 7.3 Quantity of charge, Q, obtained during the discharge at each of the three different regions of the load curves for the anatase nanotubes and the 6 nm nanoparticles.

As expected, the quantity of charge inserted at the first cycle is larger than for the following cycles. In both cases, after the first loss, the charge obtained at the initial slope remains constant during cycling. In the plateau region, the nanotubes show a slow decrease in the quantity of charge observed, whereas the nanoparticles seem to be less affected. The major difference between the two materials is observed in the final region. The nanotubes display a decrease during the first five cycles, however during subsequent cycles the quantity of charge stabilizes. On the other hand, a decrease in the quantity of charge inserted is still observable at the fiftieth cycle for the nanoparticles, suggesting that side-reactions are still occurring at the surface at low voltages. Therefore, due to the larger surface area, the nanoparticles are more affected by this phenomenon.

7.3 Lithium insertion mechanism

Anatase TiO_2 has a tetragonal structure with space group I41/*amd* [2]. Upon lithium insertion the tetragonal symmetry of anatase is reduced to orthorhombic, space group I*mma*, and the lithium content of this phase apexes at $Li_{0.5}TiO_2$[2]. When the particle size is reduced from microns to nanometres further insertion of lithium is possible, which is accompanied by the formation of a lithium rich phase, $LiTiO_2$. The latter phase is isostructural with anatase, having space group I41/*amd*[1, 4].

The evolution of the anatase structure upon lithium insertion was investigated for the anatase nanotubes using Raman *in situ* and neutron diffraction experiments.

7.3.1 *In situ* Raman experiment

The Raman spectra were recorded during discharge in galvanostatic conditions, with a current of 112 mA g^{-1}. The relative discharge curve is reported in figure 7.13 and figure 7.14 illustrates the Raman spectra collected at different stages of discharge during *in situ* experiment measurements.

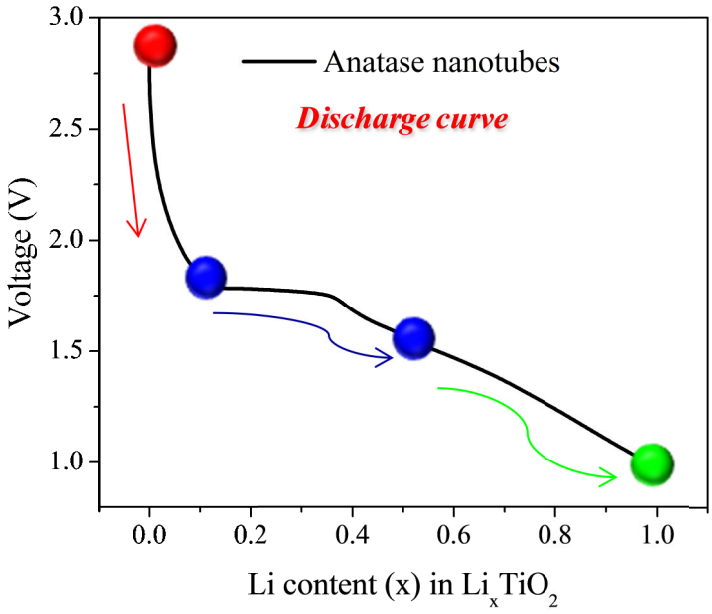

Figure 7.13 Anatase nanotubes discharge curve recorded in galvanostatic conditions at a current 112 mA g^{-1}.

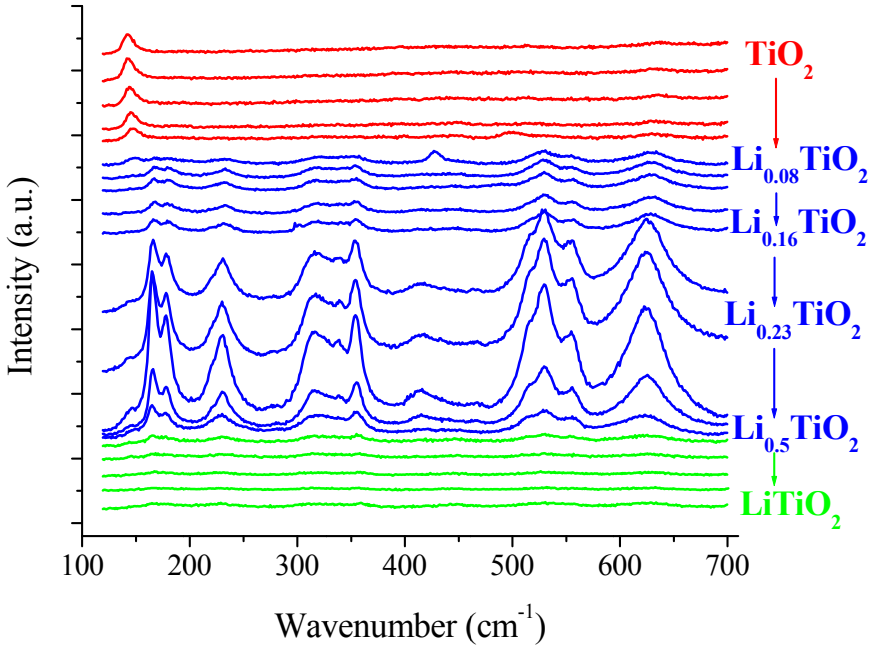

Figure 7.14 *In situ* Raman spectra of the anatase nanotubes collected at different stages of discharge during galvanostatic measurement.

In both the load curve and the Raman spectra, three distinct regions can be recognized. The first region (in red) is the homogenous insertion of lithium into the anatase tetragonal phase, up to a composition of $Li_{0.08}TiO_2$, and is reached at a potential of 1.75 V. In the Raman spectra, starting with the anatase spectrum, the appearance of new bands is observed at 1.75 V at the phase boundary of the solid solution domain. In the first domain, the band at 142 cm^{-1} is shifted to 147 cm^{-1} Following this, continuous lithium insertion leads to the second region (in blue), where the bi-phase plateau is reached, corresponding to the two-phase process between anatase (tetragonal) and orthorhombic phase, and continues until $Li_{0.5}TiO_2$ is reached, at a potential of 1.4 V. This phase transition is clearly observable in the Raman spectra where, simultaneously to the intensity decrease of the peak at 147 cm^{-1}, two bands appear at 165 and 177 cm^{-1}. Also new peaks are observed at 315, 339, 355, 528, 555 and 625 cm^{-1}. These peaks can be assigned as the Raman modes associated with the formation of the orthorhombic $Li_{0.5}TiO_2$ phase. Further lithium insertion leads to the third region (in green), the second two-phase process between the orthorhombic lithium-poor phase and a tetragonal lithium rich phase until a composition of $LiTiO_2$ is reached. The evolution of this phase in the Raman spectra is evident as a decrease of the band intensity leads to a featureless spectrum; which is in agreement with the fact that the lithium-rich phase is not active in Raman microscopy.

Our observations are in agreement with previous *in situ* Raman microscopy investigations reported by Hardwick *et al.*[6], whereby anatase nanoparticles undergo phase changes upon lithiation.

7.3.2 Neutron powder diffraction

The structural variations upon insertion of lithium into anatase TiO_2 nanotubes were investigated using powder neutron diffraction data collected on POLARIS.

During our experiment three different compositions of Li_xTiO_2 (x = 0, 0.5, 1) anatase nanotubes were investigated; the samples were prepared via chemical lithiation. The Rietveld refinements for the three anatase TiO_2 nanotube samples are reported in figures 7.15, 7.16 and 7.17. Convergence was achieved at R_{wp} values of: 2.2 % for the non-lithiated sample, 2.4 % for the 0.5 equivalents of lithium inserted sample and 1.6 % for the fully lithiated sample. The final parameters values are reported in tables 7.4, 7.5 and 7.6.

The first pattern shown in figure 7.15 is the anatase nanotubes followed by the 0.5 lithium and the fully lithiated samples respectively. The insertion of 0.5 equivalents of lithium in the anatase nanotubes led, as expected, to an orthorhombic deformation along the *b* axis. The Li titanate structure crystallises in space group I*mma*, where $a \neq b \neq c$. Two interchangeable sites for the insertion of lithium are available and are alternatively occupied. The total lithiation led to a tetragonal structure with a composition of $LiTiO_2$, which has the same space group as the pristine material (I41/*amd*), but with significantly different lattice parameters and one additional atomic site occupied by lithium. Following the first orthorhombic transformation ($Li_{0.5}TiO_2$), the additional insertion of lithium causes a further expansion along the *a* axis and contraction along the *c* axis, undergoing a second transformation into a tetragonal structure.

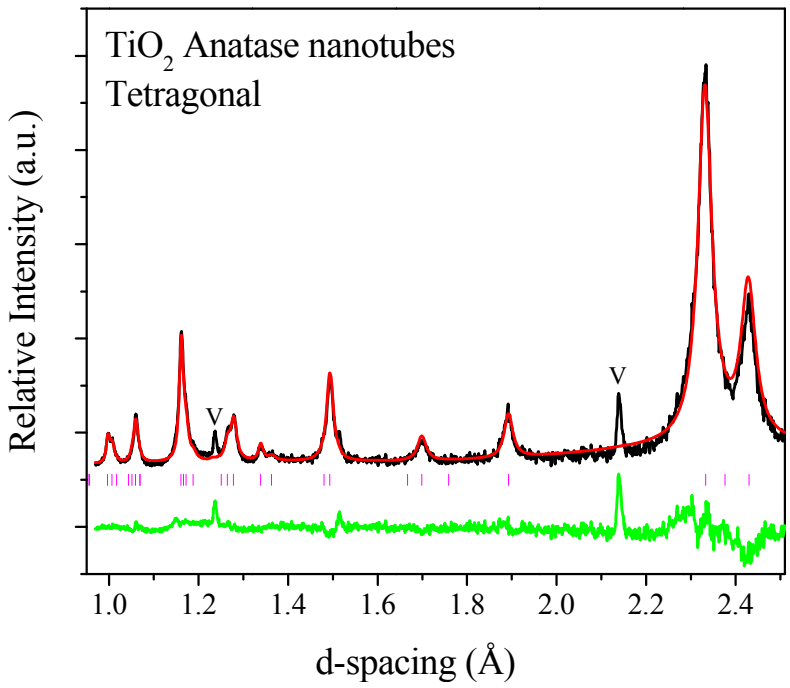

Figure 7.15 Refined powder neutron diffraction data for TiO_2 anatase nanotubes showing improved fit. Convergence achieved at R_{wp} value of 2.2 %, Rp of 2.7 % and χ^2 of 1.9.

Phase	Space Group	a (Å)	b (Å)	c (Å)	α , β, γ
TiO_2	I 41/amd	3.7859(1)	-	9.5058(10)	90°
Fractional coordinates					
	x	**y**	**z**	**$<u_{iso}>$ (Å^2)**	**Occupancy**
Ti	0.0	0.25	-0.125	0.22	1
O	0.0	0.25	0.083	1.22	1

Table 7.4 Final parameter values for anatase nanotubes refinement.

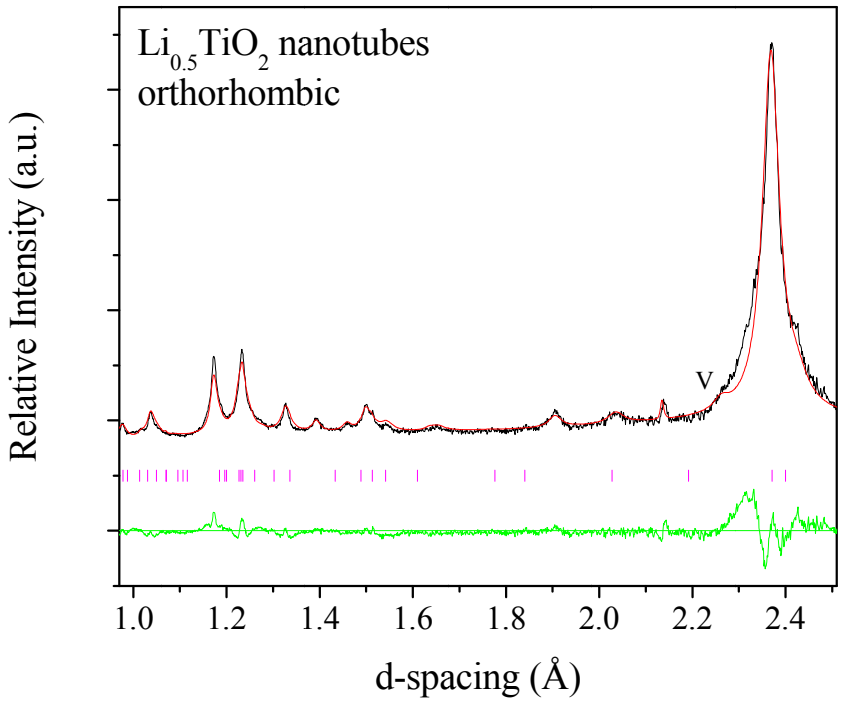

Figure 7.16 Refined powder neutron diffraction data for $Li_{0.5}TiO_2$ nanotubes showing improved fit. Convergence achieved at R_{wp} value of 2.4 %, Rp of 3 % and χ^2 of 7.

Phase	Space Group	a (Å)	b (Å)	c (Å)	α, β, γ
$Li_{0.5}TiO_2$	Imma	3.8146(6)	4.0769(8)	9.0617(24)	90°
Fractional coordinates					
	x	**y**	**z**	**$<u_{iso}>$ (Å^2)**	**Occupancy**
Ti	0.0	0.25	0.8879	3.4	1
O_1	0.0	0.25	0.1011	1.6	1
O_2	0.0	0.25	0.6523	4	1
Li_1	0.0	0.25	0.3651	0.0	0.32
Li_2	0.0	0.25	0.2881	0.0	0.19

Table 7.5 Final parameter values for $Li_{0.5}TiO_2$ nanotubes refinement.

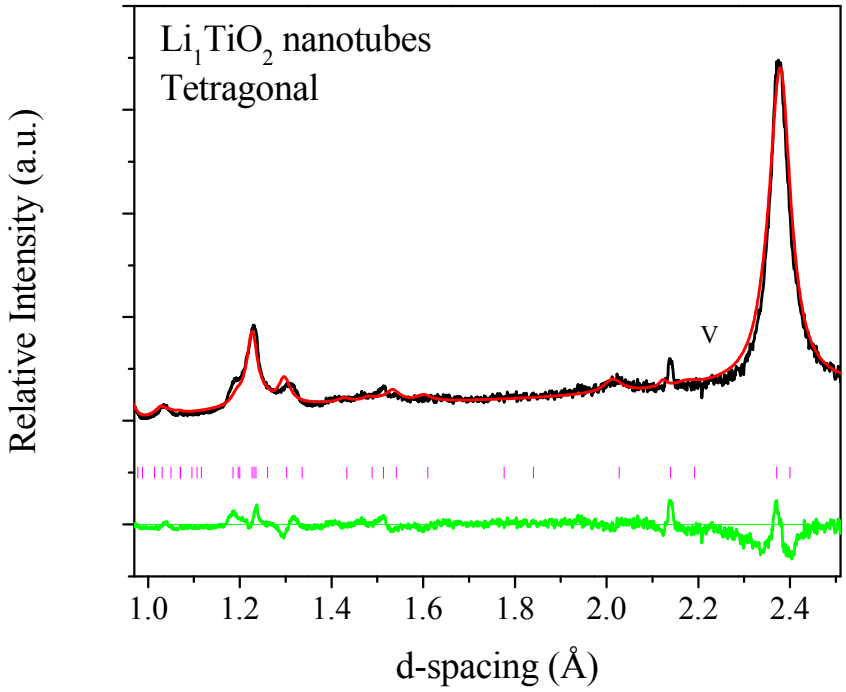

Figure 7.17 Refined powder neutron diffraction data for Li_1TiO_2 nanotubes showing improved fit. Convergence achieved at R_{wp} value of 1.6 %, Rp of 1.9 % and χ^2 of 5.4.

Phase	Space Group	a (Å)	b (Å)	c (Å)	α, β, γ
$LiTiO_2$	I41/amd	4.0555(6)	-	8.7675(31)	90°
Fractional coordinates					
	x	y	z	$<u_{iso}>$ (Å^2)	Occupancy
Ti	0.0	0.75	0.125	0.75	1
O	0.0	0.75	0.0353	1.07	1
Li	0.0	0.75	0.625	1.02	1

Table 7.6 Final parameter values for Li_1TiO_2 nanotubes refinement.

In summary the anatase nanotubes undergo two transformations upon lithiation. Firstly, from the tetragonal (I41*/amd*) to the orthorhombic structure until a maximum lithium content of 0.5 Li atoms per formula unit is reached; secondly, from the orthorhombic back to the tetrahedral reaching a lithium content of unity. Neutron data is in agreement with the Raman microscopy study.

7.3.3 Lithium insertion mechanism theories

In paragraph 7.2 the lithium insertion capacity of each of the anatase materials under investigation was discussed. Figure 7.1 showed how nano-sizing greatly improved the storage capacity.

One fact which explains the improvement in lithium insertion in nanomaterials is related to a phenomenon which occurs at the surface. This theory states that the smaller the particle size, the larger the area that is accessible for lithium insertion to take place. Due to the increased surface area in nano-sized materials, it is possible to accommodate lithium beyond the conventional bulk material. This is known as interfacial lithium storage.

The excess of lithium can be accommodated at the interfaces of the nano-sized particles in the composite electrode system, not only at solid-liquid but also at solid-solid interface between the Li host material, the electrolyte and conductive additives, resulting in an increase of total amount of stored lithium. One storage mechanism that can be used to explain lithium storage at interfaces is the so-called "job-sharing" mechanism proposed by Jamnik and Maier[6]. This states that using charge separation,

additional storage capacity for lithium can be created using a synergistic storage mode of a Li^+-accepting and an electron-accepting phase[7].

The values of the surface area for the samples under investigation have been previously reported in table 7.2 (paragraph 7.2.3). Clearly, there is a general trend that as particle size decreases surface area increases. However, it can also be seen that the nanotubes have a smaller surface area compared with the 6 nm nanoparticles. As the nanotubes have been shown to accommodate more lithium in the structure than the 6 nm nanoparticles, this theory is not sufficient to explain the exceptional performance of the nanotubes and therefore there must be another effect taking place. However, this theory provides a possible explanation for the irreversible capacity observed in the samples exhibiting large surface areas and to the phenomenon occurring on the surface during the first discharge.

Another possible explanation for the insertion of lithium in nano-materials has been put forward by Wagemaker *et al.*[1]. The authors have proposed a pseudo-phase diagram, which is reported in figure 7.18, of the lithium composition in anatase TiO_2 as a function of crystal particle size.

The authors observed that the reduction of particle size from several microns to 7 nm almost doubles the capability of the anatase powder to store lithium.

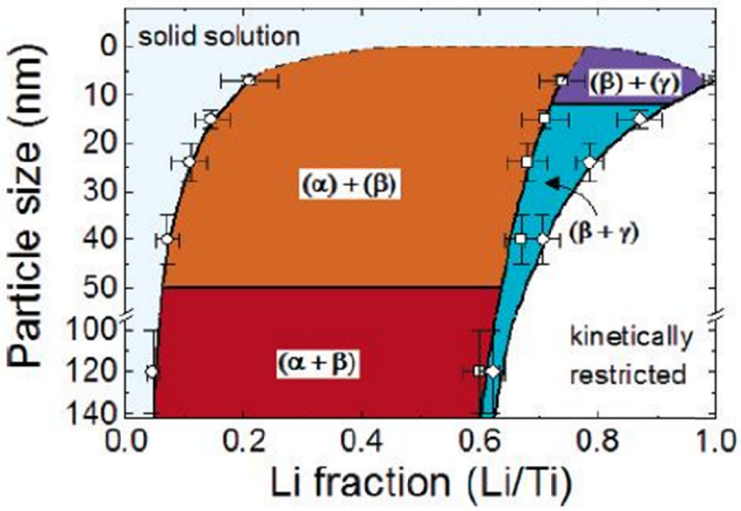

Figure 7.18 Phase diagram of the lithium composition in anatase TiO_2 as a function of crystal size. (Reprinted from reference 1, Copyright (2002), with permission from ACS journals)

In the proposed phase diagram α indicates the anatase phase (I41/*amd*), β the lithium titanate orthorhombic phase (I*mma*) and γ is the lithium rich tetragonal phase (I41/*amd*). According to the authors, the lithium rich phase is expected to be located at the surface with a shell of ca. 3-4 nm depths, and it acts as an impenetrable coating to further lithium insertion due to the small lithium diffusion coefficient.[5] The depth of this layer appears to be independent of total particle size; hence larger particles will have a smaller phase $LiTiO_2$ phase fraction and a lower overall Li composition, whereas in the case of nanoparticle sizes of 7 nm and less this leads to a complete conversion to the $LiTiO_2$ phase.

Taking into consideration the nanotubes wall thickness ranges between 2 and 3 nm, their size is sufficiently small to allow the complete phase transition into the lithium rich phase. Therefore, Wagemaker's theory would explain the enhanced lithium uptake capacity demonstrated by the nanotubes.

Both theories give good explanations for the enhancement of lithium insertion in nano-sized materials. Both rely on the thermodynamics of the lithium insertion process. It would be sensible to assume that it is a combination of both effects that can be used to explain the vast improvement in the lithium insertion in nano-materials. In the specific case of the nanotubes it would seem logical that the second explanation fits better than the first, as surface area measurement have shown. However, for a full comparison and possible explanation a comparison with even smaller particles with a diameter equivalent to the estimated wall thickness of the tubes (2-3 nm) would be required.

7.4 Chapter conclusions

In this chapter the electrochemical performance of the anatase nanotubes were compared with other anatase commercial materials differing from the tubes in both morphology and size.

It was observed that reduction in the particle size resulted in the capability of lithium uptake being increased remarkably, however, the maximum amount of lithium accommodated in the structure was observed in the anatase nanotubes load curve, where 0.98 equivalents of lithium were inserted in the structure. This dramatic effect is believed to be related to the diffusion of lithium in the structure and the thermodynamics of the lithium insertion/removal process.

The lithium insertion mechanism and the resulting phase variation in the anatase structure for the nanotubes sample was investigated via *in situ* Raman microscopy and powder neutron diffraction with the relative Rietveld refinements.

Two theories for the lithium insertion mechanism have been considered to explain our observations. The first is the interfacial lithium storage theory, which implies that the smaller the particle size, the larger the area that is accessible for lithium insertion to take place. Due to the increased surface area in the nano-sized materials, it is possible to accommodate lithium beyond the conventional bulk material. However, since the nanotube sample has a lower surface area compared with the 6 nm nanoparticles; this theory does not explain the higher lithium uptake exhibited by the nanotubes.

According to a second theory proposed by Wagemaker *et al.*[1], following bulk lithiation, the lithium rich phase formed on the surface of the nano-sized material consists of a shell of ca. 4 nm depths, which acts as an impenetrable coating to further lithium insertion. The depth of this layer appears to be independent of total particle size; hence larger particles will have a smaller phase $LiTiO_2$ phase fraction and a lower overall Li composition, whereas in the case of nanoparticle sizes of 7 nm and less this leads to a complete conversion to the $LiTiO_2$ phase. Therefore, the reduced size of the tube wall thickness would explain the complete lithiation observed for the anatase nanotubes.

In this chapter the performance of the anatase samples was also tested using galvanostatic cycling. It was noted that the nano-sized samples suffered from irreversible capacity between the first discharge and the first charge. In particular, particulates of smaller sizes were more affected by the phenomenon of irreversible capacity, which is believed to be due to their larger surface area.

The galvanostatic cycling also showed that the anatase nanotubes performed better than the other samples, in particular exhibiting excellent capacity retention, which was also confirmed at various current rates.

This is believed to be due to the nanotubes peculiar 1D morphology which is maintained upon cycling. In fact, not only do the nanotubes have very thin walls which shorten the diffusion path favouring the lithium insertion process, but their long length also ensures a closer packing within the electrode, and therefore a better contact with the other electrode components.

The combination of all these effects makes the anatase nanotubes very good candidates for future application as anodes in lithium batteries.

References

1. Wagemaker, M.; Borghols, W.J.H.; Mulder, F.M. *J. Amer. Chem. Soc.* **(**2007) **129** 4323.

2. Cava, R.J.; Murphy, D.W. and Zahurak, S. *J. Solid State Chem.*(1984) **53** 64-75.

3. Marchand, R.; Brohan, L. and Tournoux, M.; *Material Research Bulletin* (1980) **15** 1129.

4. Borghols, W.J.H.; Lutzenkirchen-Hecht, D.; Haake, U.; Van Eck E.R.H.; Mulder, F.M.; Wagemaker, M.J. *Phys. Chem. Chem. Phys.* (2009) **11** 5742-5748.

5. Hardwick, L.J.; Holzapfel, M.; Novak, P.; Dupont, L.; Baudrin, E. *Electrochimica Acta* (2007) **52** 5357–5367.

6. Jamnik, J.; Maier, J. *Phys. Chem. Chem. Phys.* (2003) **5** 5215.

7. Maier, J. *Faraday Discuss.* (2007) **134** 51.

Chapter 8

Vanadium doped TiO_2(B) nanotubes

8.1 Introduction

In this chapter a novel approach to enhance the electrochemical properties of titanium dioxide is discussed, and in particular to improve the electronic conductivity of the TiO_2 materials previously investigated. To this end, cation doping, and in particular vanadium doping of TiO_2(B) nanotubes, has been looked at.

Since Fujishima and Honda[1] discovered the photocatalytic properties of wide band gap semiconductor TiO_2, much scientific effort has been focussed on understanding the photocatalytic processes involved in order to increase its efficiency. In this sense, cation doping, such as vanadium, in the TiO_2 structure was only one of the strategies embarked upon to improve the photocatalytic properties of this material. In fact, not only can cation doping extend the absorption range of TiO_2, but it can also introduce localised trapping centres interspersed in the band gap with the resultant retardation of electron-hole recombination rates[2].

In this work, our intention was to make use of the knowledge gained within the photocatalytic field and relate it to lithium-ion technology.

8.2 Synthesis of vanadium doped TiO_2 nanotubes

Vanadium doped TiO_2(B) nanotubes were prepared via hydrothermal reaction in a similar manner to all other syntheses in this thesis. According to the desired level of doping, a certain amount of vanadium (V) oxide, V_2O_5, (Aldrich, 99.99 %) was dissolved in a 10 M sodium hydroxide aqueous solution and heated on a hotplate at 50-60 °C. Once completely dissolved bulk anatase (Aldrich, 99.8 %) was dispersed in the solution. After the mixture was stirred for 1 h, the resulting suspension was transferred to a Teflon-lined reaction vessel, sealed and then treated at 150 °C for 72 h. The product was then filtered, washed with distilled water until a neutral pH was obtained. This operation was performed in an ice bath in order to avoid dissolution of vanadium oxide in the alkaline solution. The product was subsequently dried at 80 °C overnight under vacuum. The V-doped TiO_2(B) nanotubes were obtained by annealing the acid-washed titanate at 400 °C for 2 h in air.

For this work, two levels of vanadium doped nanotubes (2 and 6 %), were successfully synthesised and fully characterised.

8.3 Characterisation of vanadium doped TiO_2 nanotubes

When studying doped nanomaterials it is extremely difficult to discriminate between real doping and nano-decoration. Therefore, it is very important to characterise the obtained product to investigate the presence of phase segregation, which would suggest a decoration rather than a real doping.

The XRD patterns of the synthesised materials are reported in figure 8.1 compared with pure TiO_2(B).

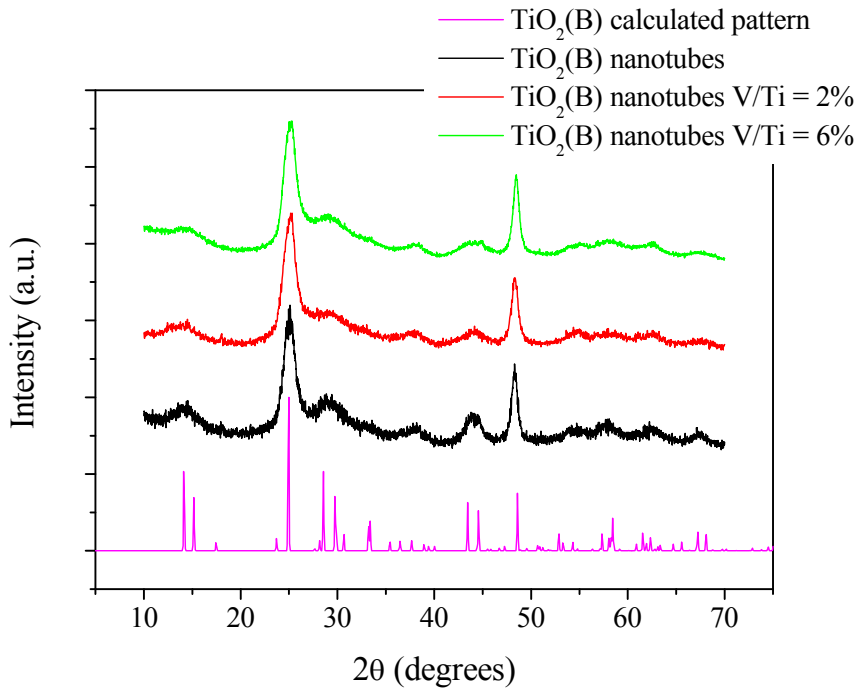

Figure 8.1 Experimental XRD pattern of pure TiO_2(B) nanotubes (in black); 2 % V-doped TiO_2(B) nanotubes (in red); 6 % V-doped TiO_2(B) nanotubes (in green) and TiO_2(B) calculated pattern (in magenta).

As can be seen, both V-doped samples exhibit the XRD pattern consistent with the TiO_2(B) nanotubes pattern and also with the TiO_2(B) calculated pattern and no additional peaks are observed. However, in order to confirm the absence of a phase segregation, the XRD patterns for the individual samples were compared with those of an equivalent sample obtained via a mechanical mixture of TiO_2(B) nanotubes and vanadium (v) oxide. The relative XRD comparison is reported in figure 8.2 for the 2 % V-doped sample, and figure 8.3 for the 6 % V-doped sample together with the V_2O_5 calculated pattern.

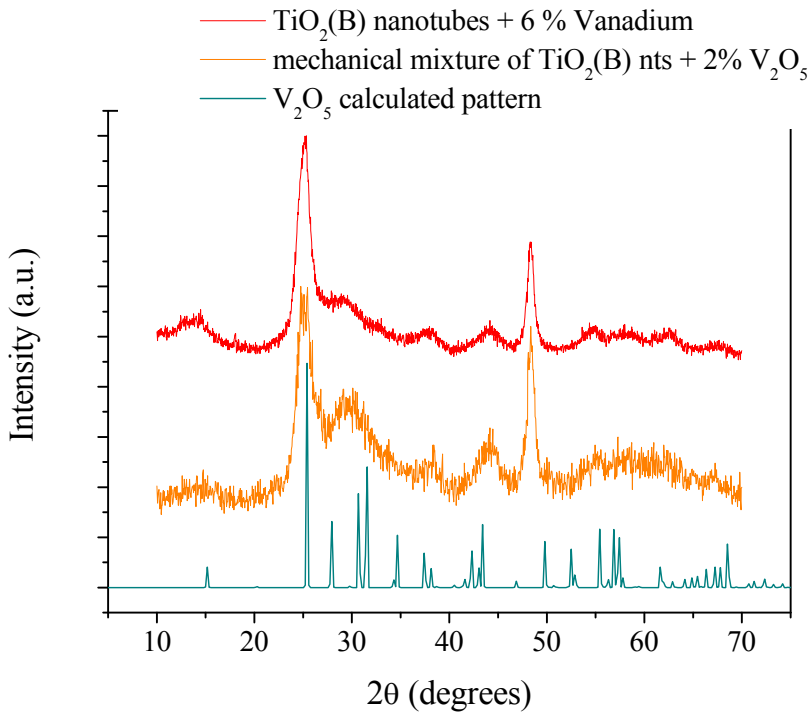

Figure 8.2 Experimental XRD pattern of 2 % V-doped TiO_2(B) nanotubes (in red); 2 % mechanical mixture of TiO_2(B) nanotubes and V_2O_5 (in orange) and V_2O_5 calculated pattern (in cyan).

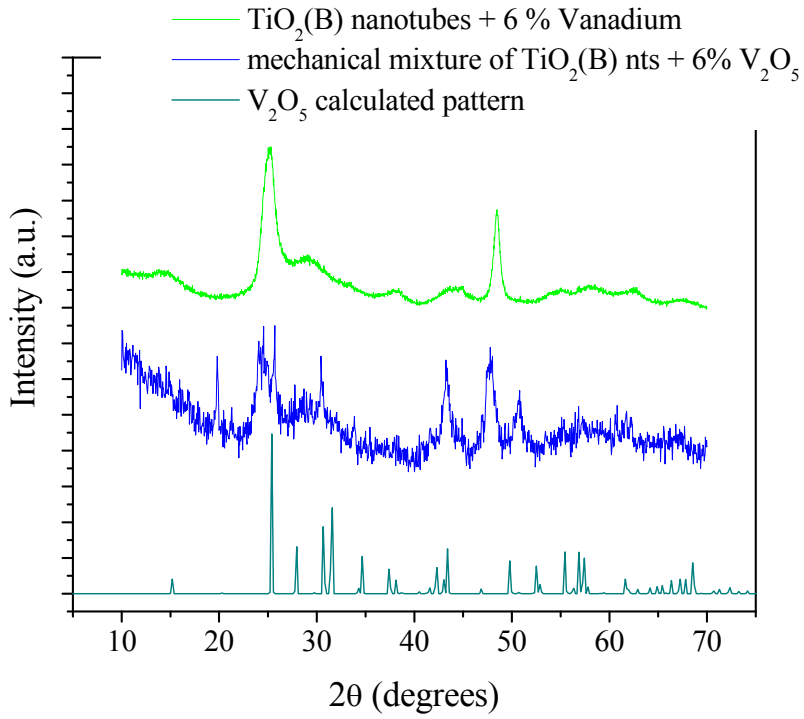

Figure 8.3 Experimental XRD pattern of 6 % V-doped TiO_2(B) nanotubes (in green); 6 % mechanical mixture of TiO_2(B) nanotubes and V_2O_5 (in blue) and V_2O_5 calculated pattern (in cyan).

Once again, no traces of the V_2O_5 phase are observable in both the V-doped sample patterns, whereas they are clearly recognisable in the mechanical mixtures, in particular in the 6 % mixture.

Further to this, the V-doped samples were also investigated using Raman spectroscopy. The Raman spectra are reported in figure 8.4 together with the pure TiO_2(B) nanotubes results.

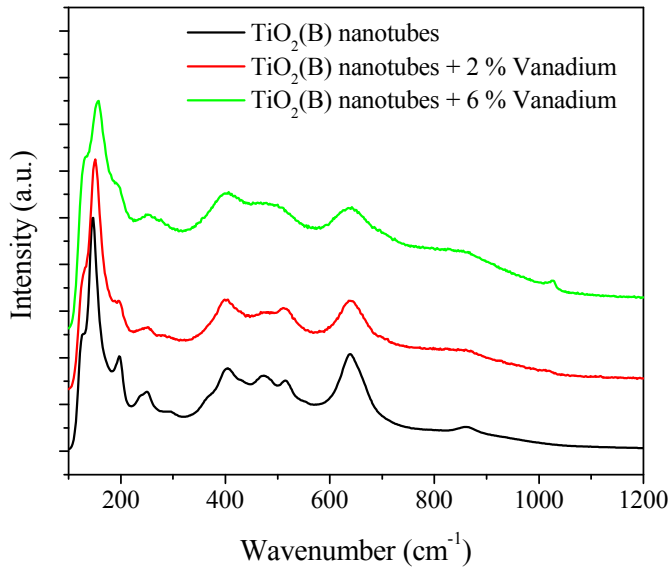

Figure 8.4 Raman spectrum of pure TiO_2(B) nanotubes (in black); 2 % V-doped TiO_2(B) nanotubes (in red) and 6 % V-doped TiO_2(B) nanotubes (in green).

Good agreement is observed between all spectra; however a few differences can be noted for the V-doped samples. On increasing the V-doping level, a shift towards higher wavenumbers is observed for the main TiO_2(B) peak at 146 cm^{-1}, which is found at 155 cm^{-1} for the 6 % doped sample. Moreover, a broadening of the multiplet between 400-560 cm^{-1} is noted together with the appearance of a new peak at 1025 cm^{-1}. The latter additional feature in the spectra is due to the presence of the isolated O-V-O bond stretching in the V-doped samples. The individual Raman spectra for the V-doped samples were also compared with the spectra of the relative mechanical mixture shown in figure 8.5 and 8.6 for the 2 % and 6 %, respectively.

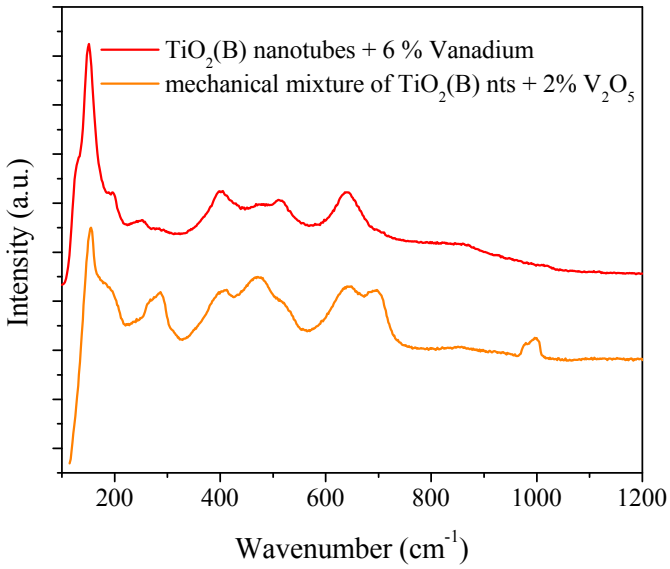

Figure 8.5 Raman spectra of 2 % V-doped TiO_2(B) nanotubes (in red) and 2 % mechanical mixture of TiO_2(B) nanotubes and V_2O_5 (in orange).

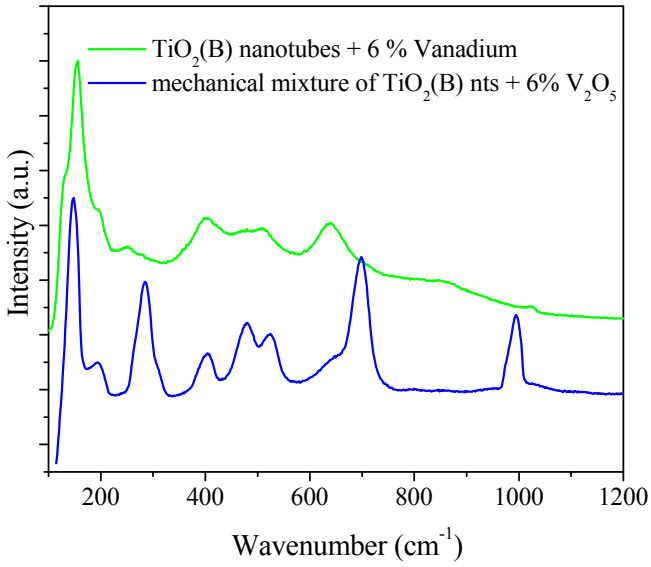

Figure 8.6 Raman spectra of 6 % V-doped TiO_2(B) nanotubes (in green) and 6 % mechanical mixture of TiO_2(B) nanotubes and V_2O_5 (in blue).

In both cases, the Raman spectra of the V-doped samples do not show the fingerprint of the V_2O_5 phase, which is clearly recognisable in the mechanical mixtures.

The analysis performed with two totally independent techniques, XRD and Raman spectroscopy, suggested the total absence of phase segregation if V_2O_5 was in the samples and that the successful doping of TiO_2(B) nanotubes with vanadium was achieved.

To further confirm the absence of any contamination, the morphology of the 6 % V-doped sample was also investigated using field emission scanning electron microscope (FESEM). The images are reported in figure 8.7.

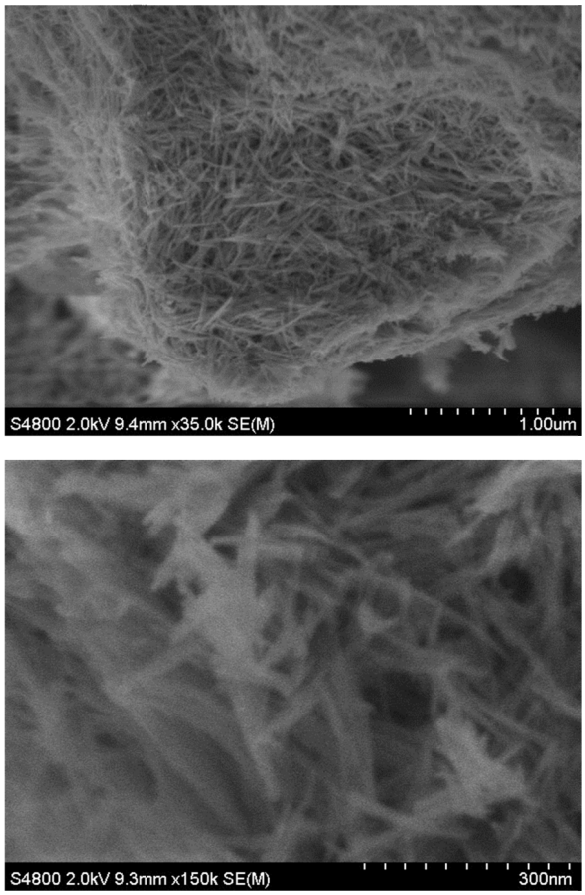

Figure 8.7 FESEM images of 6 % V-doped TiO_2(B) nanotubes at low (top) and high (bottom) resolution.

Images collected at FESEM confirmed the high morphological homogeneity of the sample, consisting mainly of tubular nano-particulates.

Following this, the sample was also studied in the transmission electron microscope (TEM). TEM images confirmed the sample constituted mainly of nanotubes and this can be seen in figure 8.8.

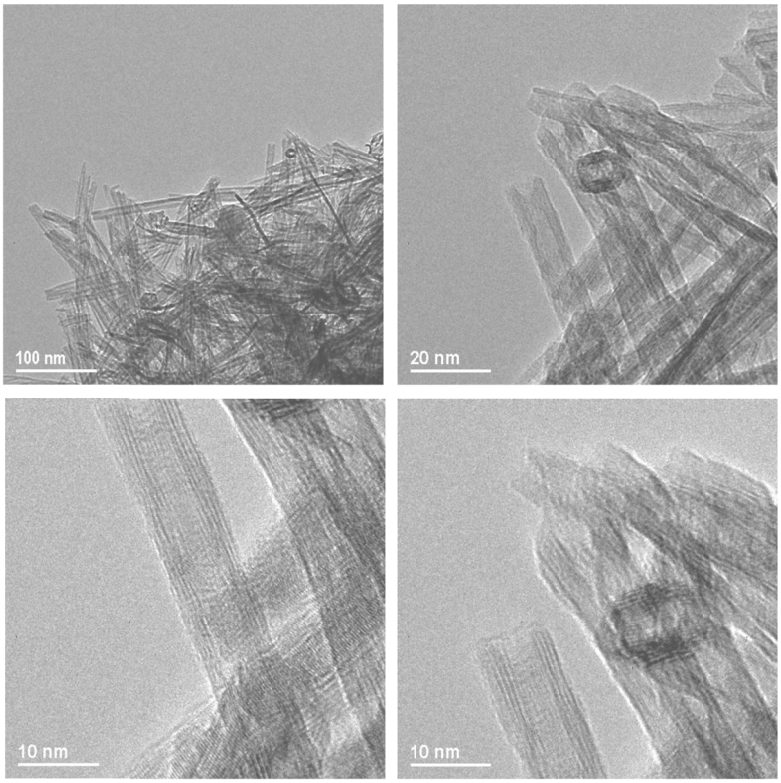

Figure 8. 8 TEM images of 6 % V-doped TiO_2(B) nanotubes.

Moreover, as can be seen in the high resolution images, the fringes of the tube walls are clearly visible and no decoration on the tubes surface is observable. This again confirms the successful vanadium doping of the nanotubes.

8.4 Band gap energy measurements

The band gap energies of the TiO_2(B) nanotubes both pristine and V-doped, was measured using the Kubelka-Munk treatment on the diffuse reflectance spectra (DRS) in UV-vis of powdered semiconductor structures[3, 4].

In the limiting case of an infinitely thick sample, thickness and sample holder have no influence on the value of reflectance (R). In this case, the Kubelka-Munk equation at any wavelength is:

$$\frac{K}{S} = \frac{(1 - R_\infty)^2}{2R_\infty} \equiv F(R_\infty) \qquad (1)$$

Where $R_\infty = R_{sample}/R_{standard}$ and $F(R_\infty)$ is the remission or Kubelka-Munk function[3].

In the parabolic band structure, the band gap, E_g, and the absorption coefficient, α, of a direct band gap semiconductor are related through the well-known equation[3]:

$$\alpha h\nu = C_1(h\nu - E_g)^{1/2} \qquad (2)$$

Where α is the linear absorption coefficient of the material, hν is the photon energy and C_1 is a proportional constant. When the material scatters in a perfectly diffuse manner the K-M absorption coefficient K becomes equal to 2α. In this case, considering the K-M scattering coefficient S as constant with respect to wavelength, and using the remission function in eq.(1), the following equation is obtained:

$$[F(R_\infty)h\nu]^2 = \left(C_2 h\nu - E_g\right) \qquad (3)$$

Therefore obtaining $F(R_\infty)h\nu$ from eq. (3), and plotting $[F(R_\infty)h\nu]^2$ against hν, the band gap of a powdered sample can be easily calculated.

The transmittance spectra (DRS) collected on the UV-vis (Perkin-Elmer) for the samples under investigation are reported in figure 8.9.

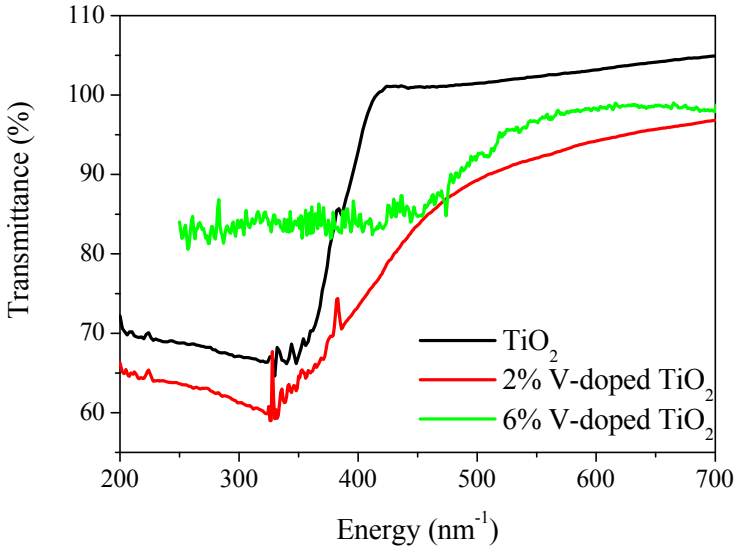

Figure 8.9 UV-vis spectra of pristine TiO2(B) nanotubes(in black); 2 % V-doped (in red) and 6 % V-doped TiO_2(B) nanotubes.

From the elaboration of data collected according to the Kubelka-Munch method it was possible to estimate the band gap energy values for the pristine, 2 % V-doped and 6 % V-doped sample, which are reported in table 8.1.

Band gap Energies (eV)	
TiO_2(B) nanotubes	3.28
2 % V-doped TiO_2(B) nanowires	3.15
6 % V-doped TiO_2(B) nanowires	2.53

Table 8.1 Band gap energy values for the material under investigation calculated using the Kubelka-Munk method.

As expected, the vanadium doping induced the decrease of the band gap energies therefore increasing the electronic conductivity in the sample. However, in order to confirm this result, it is necessary for future work to measure the electronic conductivity of the sample under investigation using the four-probe method.

8.5 Electrochemical performance of the V-doped TiO_2(B) nanotubes

8.5.1 Comparison Electrochemical performance of different V-doping degrees

Following the successful synthesis of V-doped TiO_2(B) nanotubes, the electrochemical performance was investigated and compared with the pure TiO_2(B) nanotubes.

The galvanostatic cycling of the materials under investigation is presented in figure. 8.10. The measurements were carried out at room temperature at a charge/discharge rate of 100 mA g^{-1}. All the electrodes were prepared by casting, with an electrode composition of 75 % active material, 15 % carbon and 10 % binder.

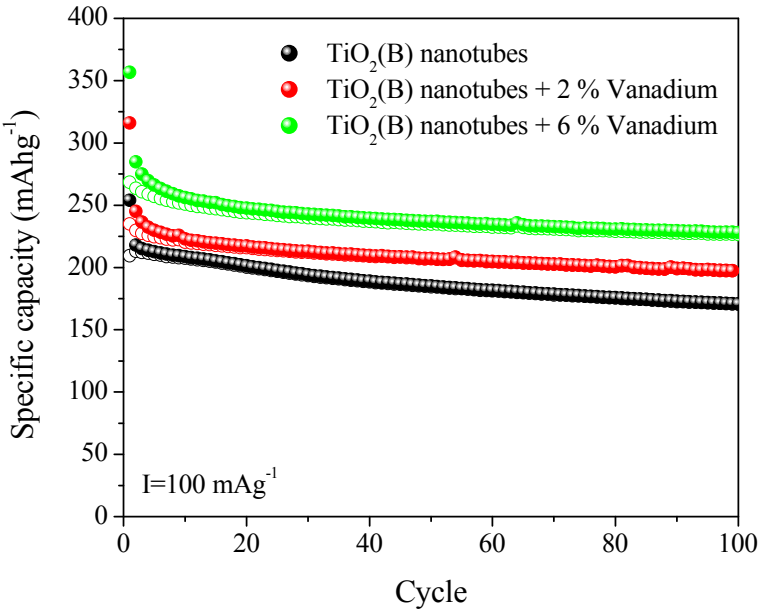

Figure 8.10 Specific capacities in charge (hollow) and discharge (filled) over 100 cycles of pure TiO_2(B) nanotubes (in black); 2 % V-doped TiO_2(B) nanotubes (in red) and 6 % V-doped TiO_2(B) nanotubes (in green).

As can be seen, the V-doping enhances the electrochemical performance of the TiO_2(B) nanotubes. In particular the 6 % V-doped sample outperforms the pure nanotubes with a capacity at the first cycle of 355 mAh g^{-1} compared with 253 mAh g^{-1} for the standard nanotubes. However, despite the remarkable increase in capacity exhibited by the V-doped materials, an increase in the irreversible capacity loss at the first cycle is also observed. The values of the coulombic efficiencies for the samples under investigation are reported in table 8.2.

Coulombic efficiency at 1st cycle	
TiO_2(B) nanotubes	82%
2 % V-doped TiO_2(B) nanotubes	74%
6 % V-doped TiO_2(B) nanotubes	75%

Table 8.2 Coulombic efficiency at the first cycle for the different TiO_2(B) nanotubes; the 2 % V-doped and the 6 % V-doped TiO_2(B) nanotubes at 100 mA g^{-1}.

8.5.2 Lithium insertion mechanism in 6 % V-doped TiO_2(B) nanotubes

In order to understand the remarkable enhancement in the capacity to insert lithium in the structure exhibited by the V-doped materials, the load curve at the low rate for the 6 % V-doped sample was compared with the load curve of the pure TiO_2(B) nanotube sample. The relative load curves, for the galvanostatic cycling at 5 mA g^{-1} are reported in figure 8.11.

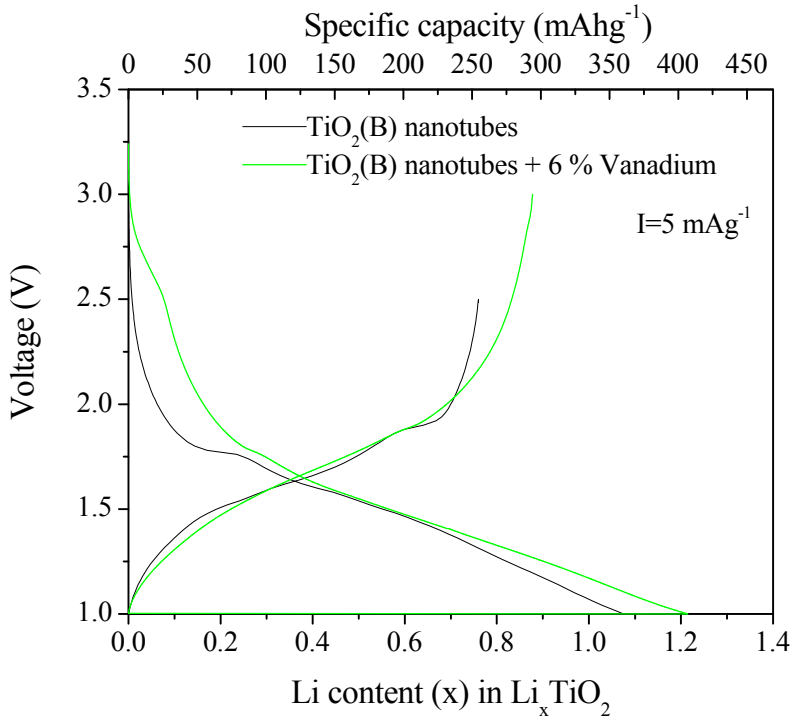

Figure 8.11 Load curves of pure TiO_2(B) nanotubes (in black) and 6 % V-doped TiO_2(B) nanotubes (in green).

As can be seen, even at low rates, the doped material inserted more lithium compared with the standard TiO_2(B) nanotubes. As expected, the open circuit voltage (OCV)

for the doped material is higher (3.25 V) than the non-doped material (2.7 V). Moreover, in the V-doped material load curve an additional plateau is observed between 3.25-2.2 V, suggesting that an additional redox process is occurring involving the vanadium.

This was also confirmed by the X-ray photoelectron spectroscopy (XPS) performed on 6 % V-doped sample. The analysis was carried out on both a pristine and lithiated 6 % V-doped sample and compared with the pristine and lithiated TiO_2(B) nanotubes. The lithiated samples were prepared via a chemical reaction with butyllithium.

The survey spectrum was collected for all samples, however only the regions of interest are reported. These are the Ti 2p and V 2p.

The results concerning each individual element will be discussed separately. Below, in figure 8.12, the V 2p regions are reported for both the non-lithiated and the lithiated V-doped samples.

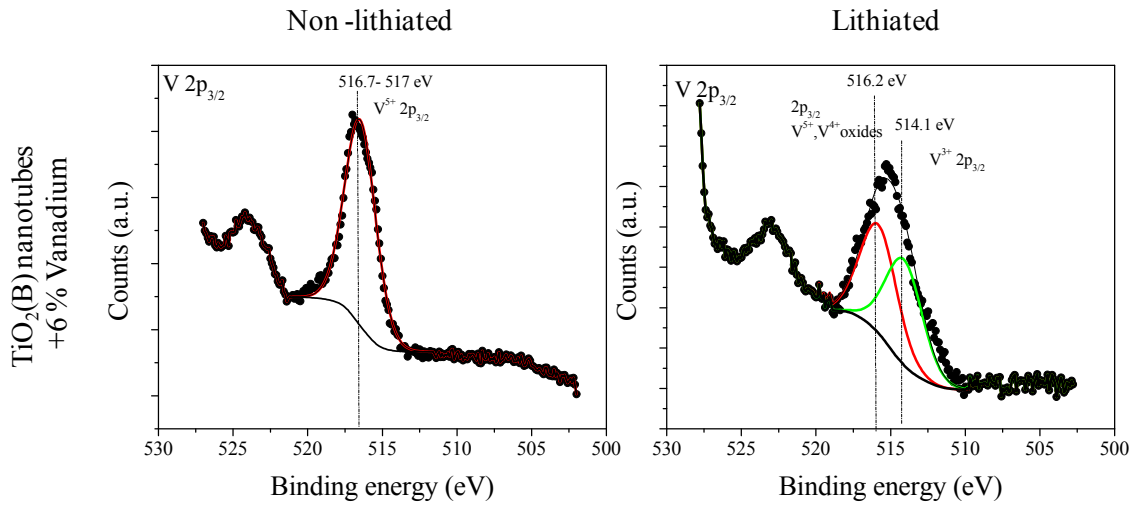

Figure 8.12 XPS spectra of V 2p region of the pristine (left) and chemically lithiated 6 % V-doped TiO_2(B) nanotubes.

For the pristine 6 % V-doped TiO_2(B) sample, in the V2p region, the $2p_{3/2}$ peak observed at 516.7 eV is associated with the V^{5+}, typical of the vanadium oxide, V_2O_5[5]. For the lithiated sample the data have been fitted with two peaks: the peak at 516.2 eV associated with the V^{5+} and V^{4+} species in the polycrystalline vanadium oxides[6] and a second peak at 514.1 eV associated with V^{3+} of the V_2O_3[7], confirming the presence of the additional redox process involving the vanadium.

In figure 8.13 the spectra of the Ti 2p regions for the investigated samples are reported.

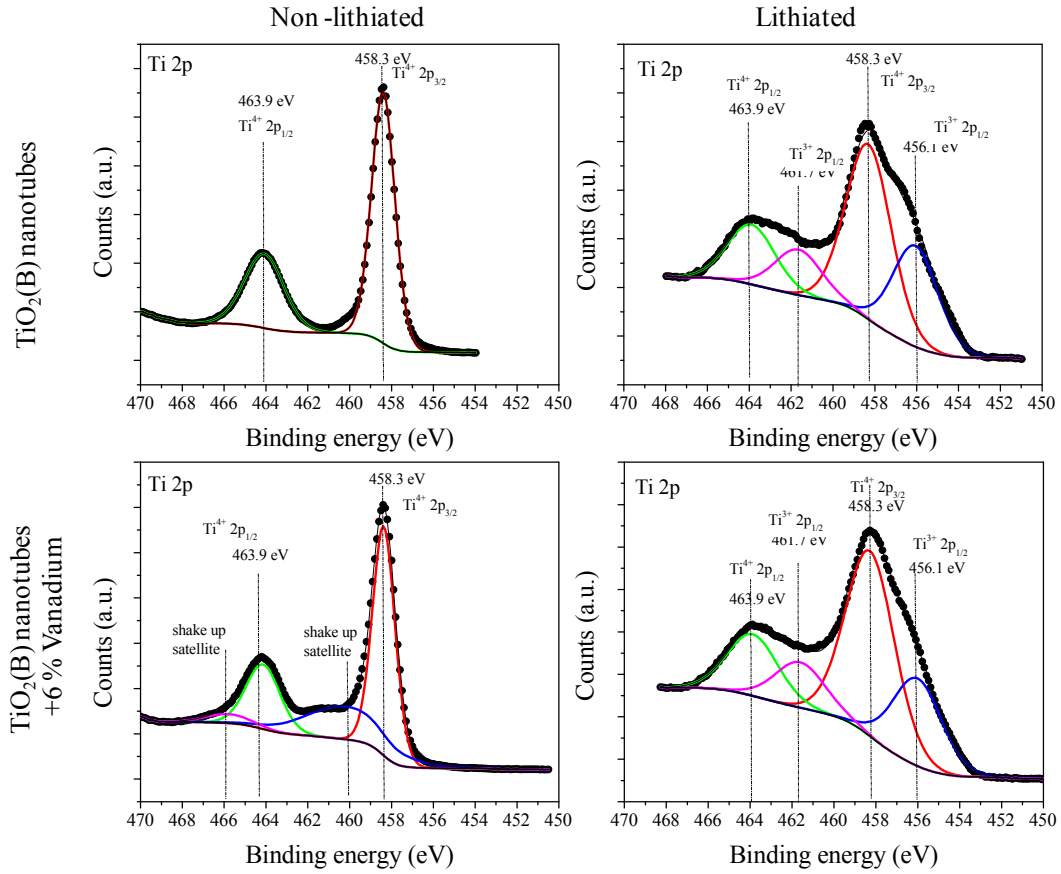

Figure 8.13 XPS spectra of Ti 2p region of the pristine (left) and chemically lithiated non-doped TiO_2(B) nanotubes (top); XPS spectra of Ti 2p region of the pristine (left) and chemically lithiated V-doped TiO_2(B) nanotubes (bottom).

The Ti 2p region of the pristine sample shows two peaks at 458.3 eV and 465 eV, which can be attributed to the Ti^{4+} $2p_{3/2}$ and $2p_{1/2}$ respectively[8]. In the chemically lithiated sample, the appearance of a second peak is observable at low binding energies, (456.1 eV), and can be attributed to the Ti^{3+} species which is formed from the reduction of the Ti^{4+} to Ti^{3+}, upon lithium insertion. The spectra in the Ti2p region obtained for the V-doped samples are very similar. No difference is observed in the behaviour between the doped and non-doped material regarding the titanium reactivity.

These results suggest that the V-doped sample offers an additional reactivity with lithium compared with the non-doped material.

8.5.3 Electrochemical performance at various rates of the 6 % V-doped TiO_2(B) nanotubes

The load curves of the 6 % V-doped materials at various rates are reported in figure 8.14. As can be observed, even at a current rate of 33 mA g^{-1}, around 1.2 equivalents of lithium are inserted, and 1.14 at a current rate of 100 mA g^{-1}.

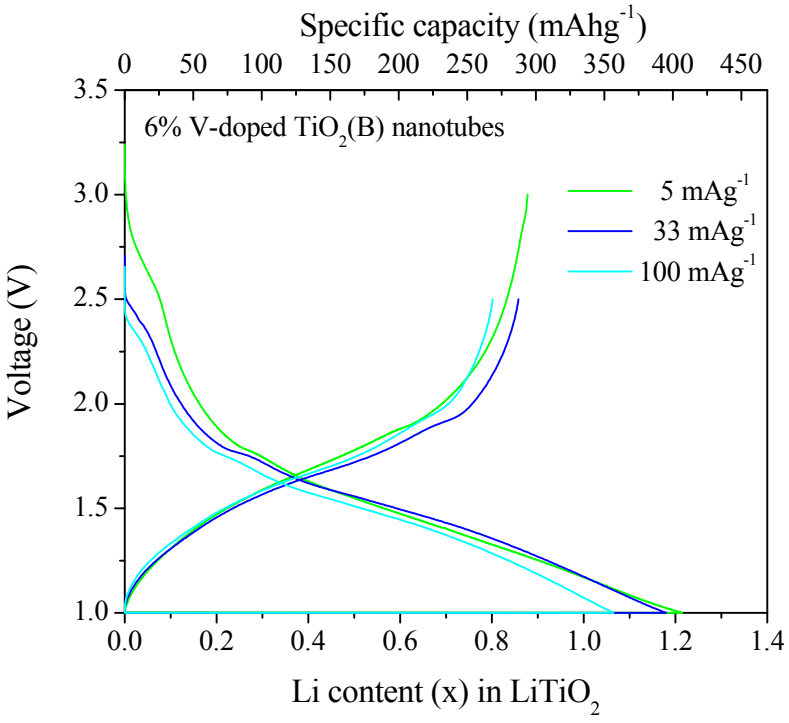

Figure 8.14 Load curves of 6 % V-doped TiO_2(B) nanotubes at various charge/discharge rates: 5 mA g^{-1} (in green); 33 mA g^{-1}(in blue) and 100 mA g^{-1} (in cyan).

The performance at different charge/discharge rates of the 6% V-doped nanotubes was also investigated. The rate performance for one cell collected at various charge/discharge rates between 33 mA g^{-1} (C/10) and 1000 mA g^{-1} (3C) (1C is equivalent to 335 mA g^{-1}), is reported in figure 8.15.

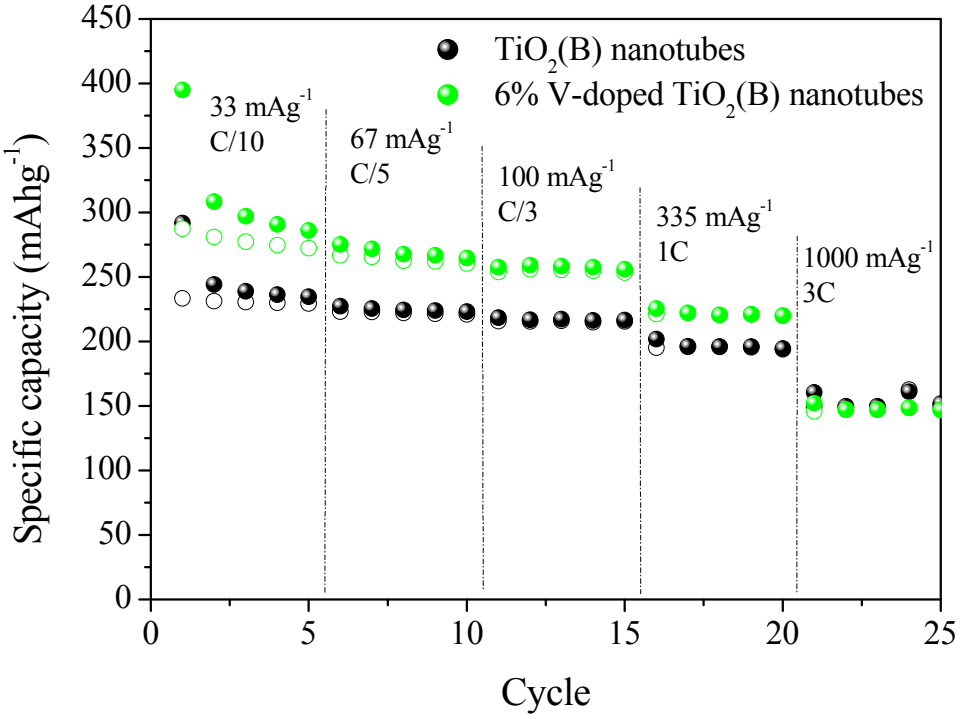

Figure 8.15 Performance of pure TiO_2(B) nanotubes (in black) and 6 % V-doped nanotubes (in green) cycled at various charge/discharge rates between C/10 and 3C.

As can be seen, the V-doped material exhibited higher capacity for current rates ranging between 33 -335 mA g^{-1}; however, at 1000 mA g^{-1} the performance is very close to the un-doped TiO_2(B) nanotubes.

8.6 Chapter conclusions

In this chapter a novel approach to enhance the TiO_2(B) performance has been attempted, in particular improving the electronic conductivity of the material.

The route chosen was the cation doping, i.e. vanadium, of the TiO_2(B) nanotubes. This was achieved by introducing vanadium (v) oxide to the classic nanotube hydrothermal synthesis procedure. Two different degrees (2 % and 6 %) of V-doped TiO_2(B) nanotubes were successfully synthesised and characterised using XRD, electron microscopy and Raman spectroscopy. The improvement in the electronic conductivity was measured using Ultraviolet-visible spectroscopy (UV-vis).

The electrochemical performance of the novel materials were tested in cell under galvanostatic cycling conditions. The V-doping was found to enhance the electrochemical performance of the TiO_2(B) nanotubes. In particular, the 6% V-doped sample outperformed the pure nanotubes with a capacity at the first cycle of 355 mAh g^{-1} compared with 253 mAh g^{-1} for the standard nanotubes, at charge/discharge rate of 100 mA g^{-1}.

From comparison of the load curves, at high voltages, the presence of an additional redox process involving the vanadium was evident. This was also confirmed by photoelectron spectroscopy (XPS) performed on the doped and the un-doped nanotubes in both lithiated and non-lithiated states.

Remarkably good performance was exhibited by the 6 % V-doped TiO_2(B) nanotubes at low current rates compared with the standard TiO_2(B) nanotubes.

References

1. Fujishima, A. and Honda, K. *Nature* (1972) **238** 37.

2. Luca, V.; Thomson, S. and Howe, R.F. *J. Cehm. Soc., Fraday Trans.* (1997) **93** 2195-2202.

3. Escobedo Morales, A.; Sanchez Mora, E. and Pal, U. *Revista Mexicana de Fisica S* (2007) **53** 18-22.

4. Kubelka, P. and Munk, F. *Z. Tech. Phys* (1931) **12** 593.

5. Mendialdua, J.; Casanova, R. and Barbaux. Y. *Journal of Electron Spectroscopy and Related Phenomena* (1995) **71** 249.

6. Colton, R.J.; Guzman, A.M.; Rabalais, J.W. *J. Appl. Phys.* (1978) **49** 409.

7. Werfel, F. and Brummer, O. *Phys. Scr.* (1983) ***28*** *92.*

8. Netterfield, R.P.; Martin, P.J.; Pacey, C.G.; Sainty, W.G.; McKenzie, D.R and Auchterlonie, G. *J. Appl. Phys.* (1989) **66** 1805.

Chapter 9

Summary and conclusions

The overall aim of this project was to investigate TiO_2 nanomaterials and their potential use in future Li-ion batteries. There are many conclusions that can be drawn from the research carried out during this project. The most important result obtained was the remarkable electrochemical performance exhibited by the nanotubular morphologies of TiO_2.

9.1 TiO_2(B) materials

Three morphologies of TiO_2(B) were successfully synthesised and subsequently studied: bulk, nanowires and nanotubes. The nano-morphologies were prepared using a previously established hydrothermal route. All three materials were fully characterised using a number of techniques including XRD, SEM, TEM and BET surface area analysis. The electrochemical performance of the TiO_2(B) bulk, nanowires and nanotubes were investigated and compared. All three materials exhibited a very similar voltage profile, suggesting that the same redox processes were occuring in each sample. An increase in the capability of inserting lithium was observed with reduction in the dimensions. In particular, the nanotubes exhibited a superior discharge capacity, exceeding one equivalent of lithium inserted in the structure. This improvement in capacity is believed to be due to the larger surface

area displayed by the nanotubes, (205 m^2 g^{-1}) compared with both the bulk (18 m^2 g^{-1}) and the nanowires (28 m^2 g^{-1}), suggesting that an additional charge storage mechanism is present on the electrode surface.

The lithium insertion mechanism in TiO_2(B) was investigated using powder neutron diffraction. This study was carried out on the bulk material and the nanowires. Both materials were found to have similar behaviour upon lithium insertion. At low lithium loadings, the lithium ion was found to be at one particular site and at higher lithium contents the initial site became unfavourable and the lithium was then found at two new distinct sites.

The performance of the three materials was also tested using galvanostatic cycling. The TiO_2(B) nanotubes outperformed the other samples, and also showed superior capacity retention over a number of cycles. However, the nanotube electrode also appeared to be the most affected by irreversible capacity at the first cycle. At this stage it was believed that the cause of the irreversible capacity was related to the greater area available for side reactions to occur in the nanotubular sample due to the larger surface area they exhibit.

Following this, the nature of the irreversible capacity observed in the TiO_2(B) nanotubes was investigated. Firstly, the effect of water contamination on the electrochemical performance was studied to establish if there was a relationship between the irreversible capacity and water contamination. However, FTIR analysis revealed the presence of residual OH groups on the surface of TiO_2, even for the samples treated and stored in a moisture free environment.

Secondly, in order to establish the voltage windows at which the irreversible processes occurred, the performance in terms of coulombic efficiency for the

TiO_2(B) nanotubes was tested at various voltage cut-offs during galvanostatic cycling. Two different voltage regions were found to highlight the poor performance of the TiO_2(B) nanotubes and were therefore studied thoroughly.

The performance at high voltage cut-off (V > 1.5 V) was proven to be due to reversible kinetic lithium trapping, which could be overcome by adding a potentiostatic step upon charge at 2.5 V to allow the complete removal of the lithium from the TiO_2 structure and therefore enhance the performance. The poor coulombic efficiency shown by the nanotubes at low voltages is believed to be due to side-reactions occurring on the electrode surfaces, which could possibly be due to the presence of residual OH groups on the surfaces of the electrode. The formation and evolution of the solid electrolyte interphase (SEI) layer was investigated using AC impedance spectroscopy. FTIR spectroscopy and X-ray photoelectron spectroscopy provided further information regarding the nature of the passivating film, which, was found to consist of both inorganic and organic carbonate species produced upon cycling and surface phosphates which are formed and decomposed upon cycling.

In order to minimise the irreversible capacity loss exhibited by the TiO_2(B) nanotubes, three different strategies were proposed and investigated to inhibit and/or compensate for the side reactions occurring at the electrode/electrolyte interface.

The three procedures trialled were as follows:

- The addition of nano-lithium to the composite electrode;
- Pre-treatment of the TiO_2(B) nanotubes with n-butyllithium (10 mol% versus titanium);
- Pre-treatment of the TiO_2(B) nanotubes with lithium ethoxide (100 mol% versus titanium).

Investigations made using all three strategies resulted in the irreversible capacity loss being dramatically reduced, and all samples exhibited a coulombic efficiency of over 90 %.

9.2 Anatase nanotubes

The exceptional electrochemical performance shown by the TiO_2(B) nanotubes provoked interest in trying to produce nanotubes of a different titanium dioxide polymorph. Anatase nanotubes were successfully synthesised following a modified procedure originally used for the production of TiO_2(B) nanotubes. Investigations into the annealing procedure, resulted in the production of an optimised set of preparation and calcination conditions which led to a purity level comparable with that of TiO_2(B) nanotubes (80-85 %).

Relevant commercially available materials with different morphologies and particle sizes were used as comparison materials for the anatase nanotubes to establish the significance of both particle size and morphology on electrochemical properties.

As was observed with the TiO_2(B) nanotubes, a reduction in particle size resulted in an increased capacity for lithium insertion. However, despite having a larger particle size, the anatase nanotubes displayed the highest lithium capacity (0.98 equivalents of lithium were inserted in the structure). This significant effect is believed to be related to the diffusion of lithium in the structure and the thermodynamics of the lithium insertion/removal process in 1D nanotubular morphology.

The lithium insertion mechanism and the resulting phase variation in the anatase nanotubes' structure was investigated via *in situ* Raman microscopy and powder neutron diffraction and the subsequent Rietveld refinements.

Further investigations on the anatase nano-morphologies were carried out using galvanostatic cycling, which showed that the anatase nanotubes are less affected by the irreversible capacity, compared with the smaller nanoparticles. Again this was believed to be due to the nanoparticles displaying a larger surface area compared with the nanotubes. The galvanostatic cycling also showed that the anatase nanotubes performed better than the other samples, in particular exhibiting excellent capacity retention, which was also confirmed at different current rates.

The reason for the excellent performance of the anatase nanotubes compared with the other nano-morphologies is believed to be due to the 1D morphology which is maintained upon cycling. Not only do the nanotubes have very thin walls which shorten the diffusion path favouring the lithium insertion process, but their long length also ensures a closer packing within the electrode, and therefore a better contact with the other electrode components.

The good specific capacity and exceptional capacity retention upon cycling resulting from the 1D nanotubular morphology makes the anatase nanotubes very good candidates for future application as anodes within lithium batteries.

9.3 Vanadium-doped TiO_2(B) nanotubes

A novel approach to improve the electronic conductivity of the material of TiO_2(B) performances was adopted. Vanadium doping of the TiO_2(B) nanotubes was achieved by introducing vanadium (v) oxide into the classic nanotube hydrothermal synthesis procedure. Two different degrees (2 % and 6 %) of V-doped TiO_2(B) nanotubes were both successfully synthesised and characterised. The improvement in

the electronic conductivity was measured using ultraviolet-visible spectroscopy (UV-vis).

The electrochemical performance of the innovative materials was tested in cells under galvanostatic cycling conditions. The electrochemical performance of the TiO_2(B) nanotubes with V-doping was found to be enhanced, particularly the 6 % V-doped sample which outperformed the pure nanotubes. Comparison of the load curves revealed the presence of an additional redox process occurring at high voltages involving the vanadium and this was confirmed by photoelectron spectroscopy (XPS). Remarkably good performances were exhibited by the 6 % V-doped TiO_2(B) nanotubes at low current rates compared with the standard TiO_2(B) nanotubes. This initial work has shown the potential for the doping of different cations within the TiO_2 structures and also the possible application of such materials in future lithium batteries as they have displayed such exceptional electrochemical performance.

9.4 Future work

The work carried out during this doctoral project has demonstrated the great potential of titanium dioxide nanomaterials, and in particular TiO_2 nanotubes, have as anodes for rechargeable lithium-ion batteries.

To further develop this new class of negative electrodes for future commercial use in rechargeable lithium-ion battery systems in which these materials are coupled with high-potential cathodes, such as lithium nickel manganese spinel (LNMO), should be studied in order to investigate the performance in a complete lithium-ion battery. Following the exceptional performance obtained by doping the nanotubes with vanadium (V), another area of future research would be exploring the effect of the introduction of cations with different oxidation states within the titanium dioxide structure.

List of Publications

Lithium Coordination Sites in Li_xTiO_2(B): A structural and Computational Study

A. Robert Armstrong, Corinne Arrouvel, **Valentina Gentili**, Stephen C. Parker, M. Saiful Islam and Peter G. Bruce, *Chem. Mater*. (2010) **22** 6426-6432.

TiO_2-(B) nanotubes as anodes for lithium batteries: origin and mitigation of irreversible capacity

Sergio Brutti, **Valentina Gentili**, Herve Menard, Bruno Scrosati and Peter G. Bruce, *manuscript submitted*.

Mitigation of the Irreversible Capacity and Electrolyte Decomposition in a $LiNi_{0.5}Mn_{1.5}O_4$/nano-TiO_2 Li-ion Battery

Sergio Brutti, **Valentina Gentili**, Priscilla Reale, Lorenzo Carbone, Stefania Panero, Peter G. Bruce and Bruno Scrosati, *manuscript in preparation*.

Anatase as Nano-negative Electrodes in Li-ion Batteries

Valentina Gentili, Sergio Brutti, A. Robert Armstrong, Brutti Scrosati and Peter G. Bruce, *manuscript in preparation.*